Aalborg Universitet

AALBORG UNIVERSITY
DENMARK

Modeling of Solar Cells and Environmental Conditions for Space Microgrids

Raya-Armenta, José Maurilio

MODELING OF SOLAR CELLS AND ENVIRONMENTAL CONDITIONS FOR SPACE MICROGRIDS

BY
JOSÉ MAURILIO RAYA ARMENTA

DISSERTATION SUBMITTED 2021

AALBORG UNIVERSITY
DENMARK

Modeling of Solar Cells and Environmental Conditions for Space Microgrids

Ph.D. Dissertation
José Maurilio Raya Armenta

A Dissertation Submitted to the Faculty of Engineering and Science at
Aalborg University in Partial Fulfilment of the Degree of Doctor of
Philosophy in Electrical Engineering
Dissertation submitted December, 2021

Abstract

A significant increase of interest in space exploration has emerged during the last years by different sectors of society, such as the scientific and industrial communities. The current efforts for a new generation of space trips point towards Mars and the Moon, which is usually considered a strategic place to settle a transit base between the Earth and the red planet. However, the creation of lunar bases demands the use of cutting-edge technologies. Therefore, several research centers are committed to develop and improve the required space technology. For the case of photovoltaic (PV) cells, which is regularly considered the best energy generation solution to space trips relatively close to the Sun, the biggest issue lies in the extreme environment of outer space, which can heavily degrade them in a short period. Particularly, the radiation-induced degradation of PV cells due to nuclei particles is a very important challenge to be overcome. Besides, given the very high cost of launching experiments to the Space, highly accurate and fast models, with results having physical meaning, to represent not only the behavior of the PV cells but also the actual space environments have to be created to perform suitable ground-based tests. In this regard, several models have been proposed to understand the dependency of the PV cell performance on different variables and the nature of its degradation due to the impact of nuclei particles under different conditions. Furthermore, improvements to the cells by thermal annealing, illumination exposure, a forward bias for recovering, while coatings, nanostructures, Bragg reflectors, for hardening, *etc.* , have been proposed. Besides, software packages like SRIM and SPENVIS are widely used to observe theoretically the distribution of defects across the PV cells created by the particle radiation. However, the state-of-the-art of PV cells modeling is mostly limited by mathematical approximations without physical meaning or numerical approaches with long processing times. On the other hand, the mathematical modeling of the radiation effects on the PV cells is mostly semi-empirical or even fully empirical with curve-fitting techniques. In this respect, this thesis presents a comprehensive review of different PV-models and studies dedicated to the radiation-induced degradation and shielding of the PV cells intending

to pave the way for improved physical models in future studies. Besides, experimental results regarding the characterization of 39 triple junction (TJ) III-V based PV cells are introduced and analyzed. Moreover, a new physical model with high accuracy in a wide range of temperatures and solar irradiances, resembling outer space conditions, is proposed. Finally, a novel technique for identifying the illumination condition at the South Pole of the Moon is proposed taking advantage of the topographic data provided by the lunar orbiter laser altimeter (LOLA) experiment of the National Aeronautics and Space Administration (NASA). Finally, by integrating all proposed models, a conceptual framework for modeling the PV cells behavior in outer space environment is planned for future works. The review process identified important challenges that need to be addressed to allow an extended PV cells lifetime under space conditions. The proposed PV cell model showed a higher accuracy in a much wider range of light intensities and temperatures in comparison to the state-of-the-art approximations while being based on physical laws. Besides, a higher accuracy was observed not only in the maximum power point (MPP) but also in the whole range of voltages. Finally, the computation of the illumination profiles over the South Pole of the Moon allowed finding the most optimal arrangement of sites for a PV-based multi-microgrid system while allowing to test improved PV models for real conditions.

Resumé

I løbet af de senere år er der opstået en betydelig stigning i interessen for rumforskning i forskellige dele af samfundet, bl.a. indenfor videnskabs- og industriområdet. Den nuværende indsats for en ny generation af rumrejser peger mod Mars og Månen, som normalt betragtes som et strategisk sted at etablere en transitbase mellem Jorden og den røde planet. Men oprettelsen af månebaser kræver brug af banebrydende teknologier. Derfor er flere forskningscentre engagerede i at udvikle og forbedre den nødvendige rumteknologi. I tilfældet med PV-celler, som jævnligt anses for at være den bedste energigenereringsløsning til rumrejser relativt tæt på Solen, ligger det største problem i det ekstreme miljø i det ydre rum, som kan nedbryde dem på kort tid. Især den strålingsinducerede nedbrydning af PV-celler på grund af kernepartikler er en meget vigtig udfordring, der skal løses. I betragtning af de meget høje omkostninger ved at opsende eksperimenter til rummet, skal der skabes meget nøjagtige og hurtige modeller med resultater, der har fysisk betydning. Disse skal repræsentere ikke kun PV-cellernes opførsel, men også de faktiske rummiljøer for at kunne udføre passende tests på jorden. I denne henseende er flere modeller blevet foreslået for at forstå PV-cellens ydeevnes afhængighed af forskellige variabler og arten af dens nedbrydning på grund af påvirkningen af kernepartikler under forskellige forhold. Ydermere er der foreslået forbedringer af cellerne ved termisk udglødning, belysningseksponering, en fremadrettet bias til genvinding, belægninger, nanostrukturer, Bragg-reflektorer, til hærdning osv. Desuden bruges softwarepakker som SRIM og SPENVIS i vid udstrækning til teoretisk at observere fordelingen af defekter på tværs af PV-cellerne skabt af partikelstrålingen. Imidlertid er state-of-the-art inden for PV-celle modellering for det meste begrænset af matematiske tilnærmelser uden fysisk betydning eller numeriske tilgange med lange behandlingstider. På den anden side er den matematiske modellering af strålings effekterne på PV-cellerne for det meste semi-empirisk eller endda fuldt empirisk med kurvetilpasningsteknikker. I denne henseende præsenterer denne afhandling en omfattende gennemgang af forskellige PV-modeller og undersøgelser dedikeret til den strålingsinducerede nedbrydning og afskærmning af

PV-cellerne med det formål at bane vejen for forbedrede fysiske modeller i fremtidige studier. Desuden introduceres og analyseres eksperimentelle resultater vedrørende karakterisering af 39 TJ III-V baserede PV-celler. Desuden foreslås en ny fysisk model med høj nøjagtighed i en bred vifte af temperaturer og solindstråling, der ligner forholdene i det ydre rum. Endelig foreslås en ny teknik til at identificere belysnings tilstanden ved Månens Sydpol ved at udnytte de topografiske data fra NASA's LOLA-eksperiment. Endelig, ved at integrere alle foreslåede modeller, planlægges en konceptuel ramme for modellering af PV-cellernes adfærd i det ydre rummiljø for fremtidige værker. Gennemgangs processen identificerede vigtige udfordringer, der skal løses for at PV-cellens levetid under rumforhold kan forlænges. Den foreslåede PV-cellemodel, som er baseret på fysiske love, viste en højere nøjagtighed i et meget bredere område af lysintensiteter og temperaturer sammenlignet med state-of-the-art approksimationerne. Desuden blev der observeret en højere nøjagtighed ikke kun i MPP, men også i hele spændingsområdet. Endelig gjorde beregningen af belysningsprofilerne over Månens Sydpol det muligt at finde det mest optimale arrangement af steder for et PV-baseret multi-mikrogrid system, samtidig med at det var muligt at teste forbedrede PV-modeller for virkelige forhold.

Contents

Contents

Contents

Preface

The exploration of the universe is something inherent to humankind given that instinctively we are looking always for new ways to survive. That is why since ancestral times the human being has explored the outer space with increasingly more sophisticated devices. Today, in the new era of the space exploration, different sectors of the society are looking forward to start colonizing other celestial bodies and the Moon and Mars are right in front of the queue. However, the contemporary space technology has to be improved in order to guarantee a very high level of safety not only for the technological devices, but also specially for the crew members. In this regard, the idea of studying and contributing in the area of the photovoltaic technology for space applications was the origin of this thesis, which is also part of the requirements to get the degree of Doctor of Philosophy in Electrical Engineering at the Aalborg University.

This thesis work is a summary of different publications made by the author in collaboration with other co-authors during the PhD studies. Most of the thesis is based on these publications, which are introduced in the second part of the thesis.

The last but not the least, I want to extend my special gratitude to my supervisors, who were always supporting and helping me throughout my PhD studies.

José Maurilio Raya Armenta
Center for Research on Microgrids (CROM), Aalborg University
December 30, 2021

Preface

Dedication

To my dad *Francisco Raya rodríguez*, who was my hero since I was a child
and my role model when I grew up.

To my children *Axel and Luka Raya Rodríguez*, who are the engine of my
heart to continue working and never give up, even during the worst times.

To my wife *SanJuana Yanely Rodríguez Rodríguez*, who is the love of my life
and my inspiration.

To my mom *Carolina Armenta Jiménez*, because all the good things that exist
on me, is thanks to her.

Dedication

Report

Chapter 1

Introduction

This thesis presents the scientific research status on III-V/Si PV technology degradation and shielding in outer space conditions as well as the modeling of PV cells and the lunar space environment. Besides, the application of this technology to space microgrids (SMGs) on the Moon is discussed. This chapter starts providing the background and motivation of this research project, followed by the objectives and limitations of the approximations proposed and experiments carried out. Then, the outline of the thesis is presented and finally a graphical description of the publications is provided.

1.1 Project Background

1.1.1 Space Exploration and the Moon

During the last few years, the space exploration interest has emerged once again aiming at different celestial bodies with commercial, security, or purely scientific purposes by different organizations and governments. For instance, the Starlink fleet by SpaceX, which aims to put in orbit thousands of satellites to provide remote internet access for remote areas on Earth, is undergoing [1]. Also, the space tourism is getting importance. The Russian Space Agency, ROSCOSMOS, plans to send again civilians to the International Space Station (ISS) [2], and private stakeholders with missions like *Inspiration 4* to send tourists to the Earth orbits [3] and the mission *DearMoon* that plans to orbit the Moon for the year 2023 with no astronauts on board of a SpaceX's Starship [4]. Furthermore, the European Space Agency (ESA) has a Planetary Defence Office committed to look for risky asteroids for Earth, and planning mitigation strategies in case a potential impact is predicted [5]. Moreover, missions with purely scientific purposes are going on, like the *Psyche* mission planned for 2022 and lead by the Jet Propulsion Laboratory (JPL), which will

orbit the Psyche asteroid made of solid metal and considered a window to understand the formation of planets [6]. The *OSIRIS-REx* spacecraft from NASA, which inspects on place the asteroid Bennu and is producing high resolution imagery, in a similar way to the LOLA experiment does around the Moon, is also going on [7]. Besides, the NASA mission *DragonFly* is planned to be launched by the year 2027, which aims to look for signs of life in the Saturn's Moon Titan and will be the first time that a multi-rotor machine is landed by humankind in another world [8]. Also, the ESA will launch the *JUICE explorer* in a mission to study Jupiter and three of its largest moons by the year 2022 [9]. For the same year, ESA plans to complete the *ExoMars programme* by launching a rover on martian floor to answer the question of whether life ever existed on the red planet [10]. Mars is being widely explored also by the *Mars Exploration Program* of NASA [11] while the *MMX mission* of Japan Aerospace Exploration Agency (JAXA) to explore two Martian Moons will be launched by 2024 [12].

Apart from all these missions, the exploration of the Moon is probably reaching its greatest extend in the coming future due to the importance of its resources and strategic location for deep-space exploration. NASA currently is continuously mapping the surface of the Moon by the LOLA experiment on board of the Lunar Reconnaissance Orbiter (LRO) [13]. Besides, the *Chang'e 4 Mission* of the China National Space Administration (CNSA) is exploring the far side of the Moon with Yutu 2 rover [14]. Moreover, NASA and international partners are working on the *Gateway Mission* to be launched in 2024, which will be an advanced lunar orbiter for vital support of planned long stays on the Moon and a key piece for future deep-space explorations beyond the Moon [15]. Even though all these missions are of extreme importance for future space explorations, manned missions are even more critical, and currently plans are undergoing by several space agencies and private companies. NASA is on its way to the *Artemis I Mission* planned for the year 2024, which will be the first long-stay base on the Moon aiming to learn how to live in other planets and prepare for future manned Martian missions [16], like the SpaceX's program *Mars & Beyond*, which plans to land on Mars in the year 2026 [17]. Finally, ROSCOSMOS and CNSA have invited international partners to join the development of an *International Lunar Research Station*, which is planned to start the construction by 2026 [18]. Fig. 1.1 shows some important undergoing and planned space missions.

1.1.2 The PV Technology for Space Applications

The success of all these future crewed missions will require the use of cutting-edge technologies, which can guarantee a safe stay on the specific celestial body. This especially applies to missions to the Moon since there is practically neither atmosphere nor magnetic shielding over there, which
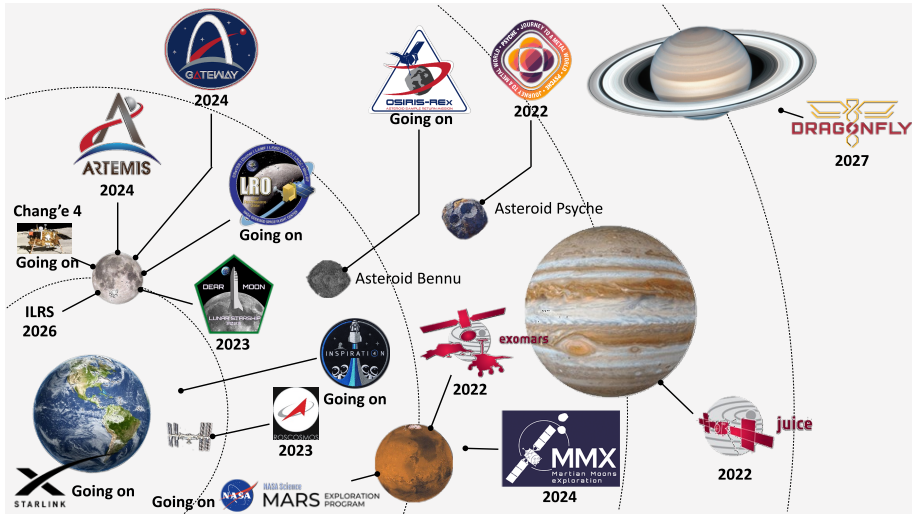
Fig. 1.1: Some current and coming space missions by different organizations. The figure is not drawn at scale.

otherwise would conserve a much better temperature regulation and prevent the entrance of high energetic ions, respectively. Regarding the production of energy, the use of fission-based generators is widely proposed, however in spite of the benefits of this technology, there is the need of special shielding and disposal of wastes, among others. Besides, the potential danger to the crew and environment must be considered. Therefore, techniques like harvesting of energy from the regolith's electrostatic charge has emerged. Nevertheless, it is still at laboratory tests and improvements should be made [19]. On the other hand, the PV is a well-tested technology in space missions, which has a lot of potential for harvesting the solar energy in locations relatively close to the Sun[1], like the Moon.

However, the hostile environment of space, which features intense particle radiation, ultra-violet photons, deep temperature cycles and vacuum, electrostatic fields, micro-meteorites, space debris for the terrestrial orbits, *etc.*, can heavily degrade the PV modules while reducing quickly their lifetime [20, 21]. The degradation due to particle radiation of PV cells is of especial interest for scientists and manufacturers given the deep damage and reduction of the cells' lifetime. In this regard, the effects of the degradation due to particle radiation of the PV cells and techniques to reduce such effects have been widely discussed in several articles, especially

---

[1]PV-based missions are considered more feasible than other technologies up to the Jupiter orbit at most (even at such a distance the nuclear-based generators are usually utilized), since the illumination intensity is inversely proportional to the square of the distance [20].

for III-V/Si materials, which are the most widely used technology for space applications. Some characteristic effects of radiated cells are the increase of reverse saturation current [22–24], anomalous degradation of the short-circuit current and open-circuit voltage in PV cells based on Si [25, 26], increment in the surface recombination velocity (SRV) [27–29], minority-carrier lifetime reduction [30], *etc.* On the other hand, some of the techniques used to reduce the effects of particle radiation over the PV cells are the base-carrier concentration optimization [31, 32], use of the hardest material against radiation as the current-limiting layer [33, 34], coverglass thickness optimization [35, 36], increase of In and P in the composition of layers [37, 38], *etc.* However, there are still challenges that III-V PV cells have to overcome for a reliable and robust long-stay deployment in outer space conditions [39].

1.1.3   Physical Modeling and Space Environment

The understanding of not only the degradation process of PV cells, but also their energy and power production dependency on extreme conditions of temperature and light intensity is of paramount importance for long-stay space missions. In this sense, experiments under actual conditions are essential, but still it is too expensive to launch payloads into space, even with the substantial reduction of cost recently provided by Falcon 9 + Dragon of SpaceX in a factor of four to the ISS [40]. Thus, the development of accurate models with a physical meaning are essential not only for the PV cells, but also the extreme environment that such cells would face in outer space. Thereby, this will allow to setup ground-based tests bench suitably to ensure a high level of similarity with the space conditions.

Nowadays, the single-diode (SD) and double-diode (DD) approximations are the main models used to represent the PV cell's behavior at standard test conditions (STCs)[2] and other temperatures and irradiance levels (light intensities) [41–45]. Models based on analytical methods [42,43], curve-fitting approximations [46, 47], solution of physical and empirical equations with values taken from the datasheet [48–50], heuristic algorithms [51–53], and artificial neural networks (ANNs) [41,54,55] have been presented. However, the underlying assumptions either decrease the accuracy of the model or the results lack of physical meaning. One possible reason behind some of the assumptions is to reduce the computational burden of the models. However, not only models with a fast processing time are required, but also with high accuracy and primarily results with physical interpretation.

The modeling of the degradation due to particle radiation of PV cells has been widely supported by numerical solvers like SRIM [36, 56–59] and

---

[2]Irradiation 1000 [W/m^2], solar spectrum AM1.5 G, and temperature 25 [°C].

SPENVIS/MULASSIS [22, 35, 60]. While these software have shown a good accuracy to represent the damage profiles of particle-radiated PV cells, they are usually too slow given that the trajectory is computed particle by particle. In this regard, several models based on physical/empirical expressions have been reported. However, to the best of our knowledge, there is not yet a well-defined model with physical explanation of such a degradation process [39]. That might be one of the possible reasons because the empirical method of the JPL and semi-empirical method of the Naval Research Laboratory (NRL) are still mainly used in the industry.

On the other hand, the outer space conditions are more extreme than on Earth and their correct modeling is of vital importance to ensure a precise estimation of the energy and power production, as well as the remaining lifetime of the PV cells. Regarding the lunar environmental conditions, the knowledge of the topography and Sun elevation for the illumination estimation, temperature levels and cycles, dust and regolith constituents and physical-chemical properties, micro-meteorites characteristics, vacuum levels, highly energetic photons, plasma, and radiation are of great importance apart from the availability of water and other volatile resources [20, 61, 62]. The Moon's topography is of special interest for illumination estimation at the polar regions since the Sun elevation is always near to the horizon and relative small terrain elevations can create shadows of kilometers long [61]. In fact, according to [63], an statistical analysis of the Moon's topography allows to say that the assessment of the relief elevations around a point of interest (POI) should be done within a radius of 210 km. In this regard, several studies have reported the computation of the lunar poles topography aiming to estimate the solar illumination availability [64–68]. Besides, due to intermittent periods between darkness and light over a POI, the need of energy storage system (ESS) is essential, but can represent a big challenge in terms of weight, volume, and fast life degradation. In this sense, fast recharge ESSs would allow the use of smaller storage devices, and the use of very tall towers, in the range of kilometers, might prevent the need of any ESS [65]. Therefore, harvesting the solar energy upon the Moon would bring many challenges, especially regarding the ESS, thus looking for new strategies to reduce or even prevent the use of the ESS is of great importance.

Apart from the illumination availability, the temperature is another important feature to be considered since some potential POIs for harvesting solar energy on the Moon's polar regions have temperatures ranging from $-220°C$ to $22°C$ [61]. For instance, maximum temperatures in the "*Shackleton crater*" are reported to be around -193.15 to -163.15 $°C$ [69]. An issue regarding large temperature cycles is the mechanical elastic stress and accordingly a faster degradation of different components [20]. Furthermore, the efficiency of solar cells might reduce due to non-linear dependencies of

their series and shunt resistances on temperature [70]. Therefore, the proper estimation of temperatures on the Moon not only to forecast the PV cells performance, but also for the whole electrical system, which the survival of the crew would depend on, is vital. In this regard, several models have been reported to compute the temperature at different points of the Moon [71–73]. In [71], an analytical model was presented by considering two functions. One for the day-side and another for the night-side of the Moon with a match at the terminators. The day-side is represented by a cosine function in terms of the Sun zenith angle while the night-side with a polynomial function with six terms. According to the results, 74% of the points analyzed are within ± 10 *K* with respect to the collected data by the *Diviner Lunar Radiometer Experiment* on board of the LRO. However, the points near to the terminator are the least accurate points given that such an analytical function does not consider the topographic effects. Therefore, the authors proposed to use a Gaussian distribution of longitude offsets to produce a small randomness while resembling the effect of topography. The estimation near the poles was also not accurate. One important issue with this study was the assumption of being symmetric with respect to the equator while the effect of selenographic position was ignored.

Other studies have computed the Moon's surface temperature by solving a physical-based one-dimensional partial differential equation, with initial boundary conditions, while taking into account topographic and Albedo effects. Besides, the internal heat source of the Moon was assumed negligible in comparison to the heat provided by the sunlight. The topographic effect was included with digital elevation models (DEMs) dataset from LOLA and *Chang'E-1 orbiter*. The method uses another model [73] to estimate the illumination based on distances between the celestial bodies relative to 1 astronomical unit (AU)[3] and geodetic latitude, but without considering neither the terrain slopes nor elevations. Then, such a model was improved by adding two conditions to determine whether the target place is illuminated or in shadows while considering the terrain slope. However, these conditions do not take into consideration the spherical shape of the Moon. The improved model was tested for latitudes lower than 60° in both hemispheres while showing a good resembling with actual data provided by the *Diviner experiment* at noon time. According to their results, 82.3% of the points are within ± 10 *K*. This model was compared with the "soft" analytical model of [71], showing better results for low latitudes [72]. The improved model also was applied to compute the temperature profile of the *"Hercules crater"* [73].

---

[3]The average distance between the Earth and the Sun. 1 AU $\approx$ 149597870.7 [*km*].

1.2 Motivation

The future of humankind will belong to more than one single planet due to our natural instinct of exploration. And in our path towards that future, nowadays several sectors of the society are investing time and money to develop new technologies based on the cutting-edge scientific research. Especially the study of electrical systems for space applications is of huge interest these days since it is a vital element for the survival of human beings in the extreme hazardous outer space environment. In this regard, the new concept of SMGs has been proposed recently, which are based on the widely-studied islanded terrestrial microgrids (MGs), but with a much higher level of reliability, resiliency, robustness, optimization, and stability (RRROS) not only for the whole system, but also for each individual element [74–77]. In case of the energy production, atomic fission-based generation has been proposed given its benefits in terms of mass, volume, being independent of location, modularity, *etc.* However, issues like radiation, special shielding requirements, proper disposal of radioactive wastes, *etc.* , have made the researchers to look for other alternatives. One promising technology for energy harvesting on the Moon is the PV technology given that it can be installed near the human base with no special requirements of shielding, it is modular, no ambient issues are presented, it is a mature technology, and it has a high level of RRROS. Besides, the PV technology has been considered the most applicable technology for energy harvesting not only in the orbit of the Moon, but also on its surface. Nevertheless, the power generation hugely depends on the sunlight availability and temperature. Besides, the lunar dust can cover the panels and reduce the efficiency, and effects of radiation of ions and highly energetic photons represents a way to degrade quickly the PV cells [20,76]. Therefore, more investigation on this technology is required.

In this sense, to contribute in this area of research, the following research questions were formulated and answered during the development of this thesis.

- What are the most challenging aspects of the PV cell technology for space applications?

- How can the solid state physics be applied to develop a reliable physical model of PV cells/modules to ensure a high accuracy not only at the MPP in STCs, but also in the whole range of voltages, as well as a wider range of illumination intensities and temperatures?

- How can the illumination condition be estimated at any point of the Moon to compute the PV energy production while reducing or eliminating the need of ESSs? and how this illumination can be used to compute the temperature?

9

- What are the requirements that PV cells should meet to be applied in a space environment and the merits and demerits of this technology in comparison with other options?

1.3 Objectives and Limitations

The main objective of this thesis is to contribute in the comprehension of the physics behind the performance of the III-V/Si PV cells in space environments with large variations of temperature and light intensity, as well as highly energetic nuclei particles, which will accelerate the degradation process. This will contribute in the development of improved physical models to represent the PV cells and their shielding, as well as updating the degradation status of PV cells due to particle radiation while identifying unmet challenges, which the future PV technology should meet to be applied efficiently on SMGs. Thereby, the development of suitable experimental ground-based setups and real-time modeling will be improved. Besides, an updated status of the challenges that still the PV cells for space applications should overcome is quite valuable to pool the efforts of the scientific research in a right direction while improving the current technology and paving the way for future space crewed missions.

The specific objectives are listed in the following.

1. Identification of challenges that the III-V/Si-based PV cells have to overcome to be applied effectively in environments featuring high radiation of nuclei particles.

2. To develop an improved physical-based model of a PV-module with a high accuracy in the whole range of voltages from zero to the open circuit voltage and in a wide range of light intensities and temperatures.

3. Perform the characterization of degraded PV cells by the radiation of energetic protons at standard conditions and outer space conditions of high vacuum and deep temperatures.

4. Computation of the time-series illumination profiles of any POI upon the Lunar south pole to optimally estimate the allocation of a PV-based multi-SMG upon the Moon's south pole while preventing the use of ESS.

5. Identification of merits and demerits of the PV and other technologies for energy generation in space environments, as well as the main differences between the ground-based and space-based PV-technology.

The models presented in this thesis are based on several assumptions for simplifications of the treatment of the physics and/or to delimit the

applicability of the study. These assumptions are limitations that should be overcome to increase the accuracy of the models and expand the study frontiers. These limitations can be listed as follows.

1. The identification of the challenges that PV cell technology should overcome to be effectively applied in space environments is limited to III-V/Si PV cells since this is currently the most used technology for space applications. However, technologies like the *Perovskite PV cells* have shown to be a promising solution for future space applications. Besides, the unmet challenges are limited to degradation due to particle radiation and other features like temperature cycles, ultraviolet (UV)-radiation, galactic cosmic rays (GCRs), electrostatic fields, micro-meteorites impacts, *etc.* , are not thoroughly discussed.

2. The PV-module model is based on physical equations. However, the model still contains a few parameters that are found by curve fitting by using additional IV-curves obtained either from the datasheet or experimental measurements.

3. Even though the optimal allocation of a multi-SMG can prevent the use of any ESS, the distance between the sites is still in the range of kilometers, which represents nowadays the use of wires to transport the energy. This is because the study is limited to twenty sites, which in turn limits the options of the optimization algorithm.

Regarding the development of experiments, the limitations can be listed as follows.

1. The PV cells utilized for the experiments are only of one type. Namely TJ and made of $Ga_{0.5}In_{0.5}P/Ga_{0.99}In_{0.01}As/Ge$.

2. The experiments are limited to only radiation of protons. However, the protons are usually the more damaging particle.

3. The study is limited to two levels of proton's energy: 1 and 2 $[MeV]$.

4. The spectrum AM0 reproduced by the solar simulator (SOSIM) still presents differences with respect to the actual AM0 spectrum.

5. The deep temperature measurements were performed only to 24 PV cells due to schedules of the host company.

The discussion of the limitations is expanded in the following chapters.

1.4 Thesis Outline

This Chapter provided briefly the background of this thesis project, where several present and future space missions were described while a special attention for the lunar exploration can be observed. Besides, the potential of PV technology for space applications was briefly described along with issues regarding the extreme environmental conditions in outer space. In this sense, some of the effects that characterize a degraded PV cell by particle radiation and some techniques to reduce such effects were introduced. Then, the importance of modeling the space environment was described and finally the motivation, objectives, and limitations of the project were discussed.

Chapter 2 introduces the PV-technology for space applications, describes the implications for working on space, and makes a comparison between other technologies and the same PV-technology but for terrestrial applications. Chapter 3 describes different techniques for PV modeling, with advantages and disadvantages of each technique. Besides, it introduces a new proposal for modeling PV-modules with a high accuracy in the whole range of voltages (from zero to open-circuit voltage) and for a wider range of light intensities and temperatures in comparison with other techniques. Chapter 4 provides a chronological review of the different studies carried out on PV cells degradation due to highly energetic particle radiation. Besides, it presents the challenges that PV-technology should overcome to be applied effectively in outer space conditions featuring particle radiation. Then, the experiments performed and the setups utilized are introduced in Chapter 5. The collected data is analyzed and some unexpected results are identified to be further investigated. Afterwards, Chapter 6 describes the importance of modeling the outer space conditions and provides a novel technique to compute the illumination conditions on the Lunar poles. Moreover, the Chapter describes how this technique can be used to allocate optimally a multi-SMG upon the Moon's poles. Finally, the conclusions and future work are provided in Chapter 7. A scheme describing the content of the present thesis work is shown in Fig. 1.2.

1.5 Distribution of Publications

The present thesis work is based on four papers developed during the PhD studies as a first author or co-author. These papers are listed in the following and the correspondence between each publication and chapter of this work is presented in Fig. 1.3. Additionally, the experimental results, which have not been published yet, are also presented and briefly discussed in the Chapter 5.

Journal Papers:

1.5. Distribution of Publications
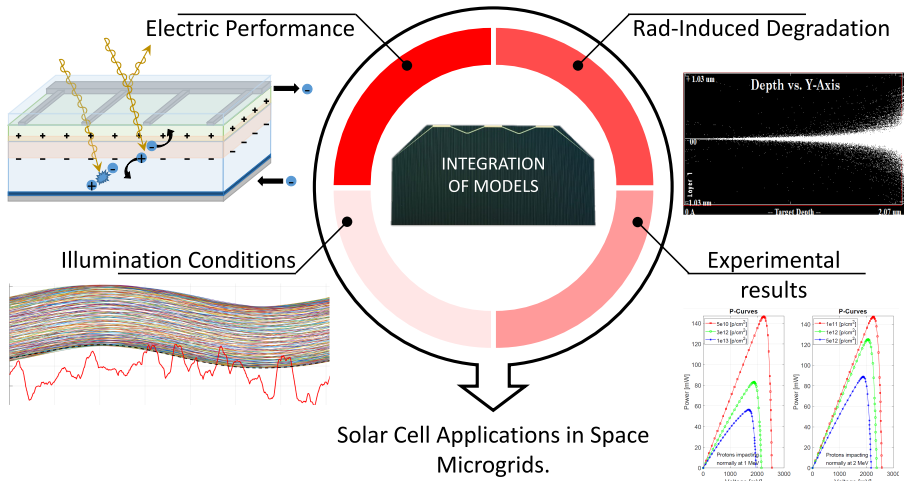
Fig. 1.2: Graphical outline of the thesis.

J1 Saha, D., Bazmohammadi, N., **Raya-Armenta, J.M.**, Bintoudi, A., Lashab, A., Vasquez, J.C., Guerrero, J.M., "Space Microgrids for Future Manned Lunar Bases: A Review", *IEEE Open Access Journal of Power and Energy*, 2021, doi: `https://doi.org/10.1109/OAJPE.2021.3116674`.

J2 **Raya-Armenta, J.M.**, Ortega, P.R., Bazmohammadi, N., Spataru, S.V., Vasquez, J.C., Guerrero, J.M., "An Accurate Physical Model for PV Modules With Improved Approximations of Series-Shunt Resistances", *IEEE Journal of Photovoltaics*, vol. 11, no. 3, pp. 699-707, May 2021, doi: `https://doi.org/10.1109/JPHOTOV.2021.3056668`.

J3 **Raya-Armenta, J.M.**, Bazmohammadi, N., Vasquez, J.C., Guerrero, J.M., "A short review of radiation-induced degradation of III–V photovoltaic cells for space applications", *Solar Energy Materials and Solar Cells*, vol. 233, 2021, doi: `https://doi.org/10.1016/j.solmat.2021.111379`.

J4 **Raya-Armenta, J.M.**, Bazmohammadi, N., Vasquez, J.C., Guerrero, J.M., "Optimal Allocation of a Photovoltaic-Based Space Multi-Microgrid over the Lunar South Pole Based on Illumination Time-Series Profiles", *Submitted to IEEE Transactions on Smart Grid*.

The next journal paper was also developed during the PhD studies, but excluded from this thesis.

J5 **Raya-Armenta, J.M.**, Bazmohammadi, N., Avina, J.G., Sáez, D., Vasquez, J.C., Guerrero, J.M., "Energy management system optimization in islanded microgrids: An overview and future trends", *Renewable and Sustainable Energy Reviews*, vol. 149, 2021, doi: `https://doi.org/10.1016/j.rser.2021.111327`.

Modeling of Solar Cells and Environmental Conditions for Space Microgrids

Report

Journal Papers

Ch. 1: Introduction

Ch. 2: Solar cells for applications in space microgrids.

J1

Ch. 3: Modeling of PV-cells and a proposal for an improved physical model.

J2

Ch. 4: Radiation-induced degradation mechanisms of III-V PV-cells for space applications.

J3

Ch. 6: Illumination conditions of the Lunar south pole and an optimal allocation to harvest solar energy.

J4

Fig. 1.3: Correspondence of the papers developed during the PhD studies with each chapter of this thesis.

Chapter 2

Solar Cells for Applications in Space Microgrids

2.1 Introduction

The concept of SMGs has been recently proposed by different authors [74–77]. The idea is inspired by the similarity between the terrestrial islanded MGs and planned space bases. However, the SMG will demand a much higher level of RRROS than the terrestrial counterpart since the crew life will depend on it. In this regard, the efforts to improve the technology, control scheme, energy management system (EMS), and so on, have been intensified to ensure reliable operations of the future space bases. Besides, special interest has been deposited in the closest celestial body, *the Moon*. The reason behind that is likely because its proximity, strategical position for future deep space missions to Mars and beyond, and the availability of resources, like water and other volatile substances [15,62].

Just like on Earth, the selection of a position upon the Moon for establishing an SMG will change the energy needs of the costumers, in this case the space base. The position will be selected taking into account the lunar terrain topography and accessibility to the POI, temperature range, availability of energy, ease of a good communication link between the Earth and Moon, as well as water and other frozen volatiles, among others [62,76]. Then, regarding the selected position(s), the power and energy demanded by different loads on the space settlement must be managed as optimally as possible while having a high level of RRROS, not only of the whole system, but each individual element of the SMG. Fig. 2.1 shows a graphical representation of an SMG where the factors affecting the base selection are indicated, as well as the main parts of an SMG.
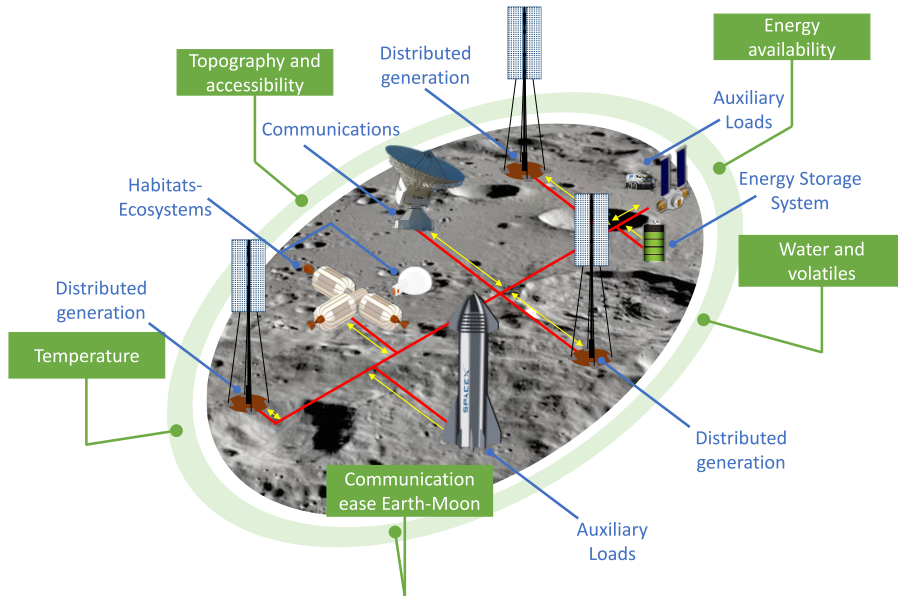
Fig. 2.1: Graphical representation of a PV-based SMG. Green labels: some factors to consider for the site selection. Blue labels: main parts of the SMG. Red lines: Power lines. Yellow lines: Communication lines (if any). The loads are mostly comprised by life support systems (habitats, ecosystems, *etc.*), communication systems, scientific facilities, exploration vehicles, rovers, charging systems, in-situ resources utilization facilities, tools, other supported equipment [76,77].

For the energy generation, fission-based reactors have been widely proposed [16,78,79]. Besides, regarding Lunar bases, the harvesting of energy from electrostatic fields generated on the surface has been suggested [19]. However, the large availability of sunlight in the orbit and over the surface of the Moon makes the PV-technology a very promising candidate to produce the energy required by future Lunar missions [20].

2.2 Site selection for a PV-based SMG

As indicated previously, the site selection to settle an SMG depends on several factors, see Fig. 2.1. However, the relevance of each factor will differ from each kind of energy source utilized. For instance, while for a fission-based reactor the illumination availability is not an issue, for the PV-technology it is vital. Then, regarding a PV-based SMG, the site selection depends heavily on the energy production and degradation of the PV-modules. Specifically for Lunar conditions, the solar irradiance (illumination), frequency and duration of darkness periods (night and

Fig. 2.2: Location of highly illuminated POIs on the Lunar poles. (A) South Pole. (B) North Pole. See Table 2.1. The latitudes range from $\mp 87.5°$ to $\mp 90°$ [76].

eclipses), site topography (especially for polar locations), temperature profiles, radiation of nuclei particles, and meteorite flux [76] are among the main factors to consider.

The light intensity over the surface of the Moon is usually assumed to be around 1367 $[W/m^2]$, corresponding to the spectrum air mass zero (AM0), since the distance from the Sun to Moon is practically the same than from the Sun to Earth [80, 81]. Besides, the illumination availability over the surface of the Moon, depends hugely on the position of the POI and the topography around there. While positions around the Moon's equator have periods of $\approx$ 15 days of light and $\approx$ 15 days of darkness, near the Lunar poles, the Sun is always around the horizon. Thereby, there are places with almost continuous darkness and others with almost continuous illumination. For instance, some places located around the *Shackleton crater* rim have been identified to have around six months of constant illumination while the other six months of intermittent day-night periods [76, 82]. The reason lies on the fact that the Lunar topography is highly irregular and small elevations of the terrain near the poles might cast shadows of kilometers long, because of the low Solar elevation angle. In this regard, several studies have been dedicated to compute the topography of the Lunar poles by using the LOLA databases [83, 84].

Therefore, regarding the Moon, locations on the poles with high illumination availability are the most desirable for PV-based SMGs. Moreover, it has been stated that places featuring frequent changes between illumination and darkness are preferable as long as fast charging ESSs are used, given that this can reduce the ESS size [65, 76]. Table 2.1 shows 26 sites with high average illumination levels on the polar regions previously identified [68, 76]. Besides, Fig. 2.2 shows the location of these sites on a stereographic projection of the poles using the databases provided by the LOLA experiment mounted on the LRO of NASA [85].

Some studies have proposed to add tall towers generally on the rim of craters on the Lunar poles to reduce or even eliminate the need of ESS [65,66],

Table 2.1: Sites with high average illumination on the Lunar Poles at surface level [68,76].

North Pole			South Pole		
Longitude	Latitude	Average illum. (%)	Longitude	Latitude	Average illum. (%)
326.44	89.65	72.60	222.84	-89.45	76.00
110.38	89.85	78.10	203.97	-89.78	81.00
126.80	89.37	84.60	245.94	-89.31	75.60
130.56	89.35	84.01	204.27	-89.78	86.71
127.94	89.36	83.87	123.64	-88.81	85.50
128.94	89.36	82.02	197.05	-89.69	85.24
242.24	88.06	86.08	198.43	-89.69	84.44
232.04	87.31	81.55	205.14	-89.79	82.37
7.22	87.20	82.16	123.95	-88.80	82.37
8.11	87.00	79.53	37.07	-85.30	85.95
7.78	87.05	77.87	37.57	-85.55	82.34
8.07	86.99	76.51	243.22	-85.73	79.54
7.02	87.12	76.94	356.80	-85.96	80.61

see Fig. 2.3. For instance, it has been stated that a tower of either 1.5 [km] at a location on the north pole or > 3 [km] at a location on the south pole can prevent the use of any ESS [65]. Moreover, recently a study is proposing to harvest the energy from different sites simultaneously in any of the Lunar poles to reduce significantly the towers' height while preventing the use of ESS [86].

On the other hand, it is desirable to place the PV-based SMG in a location with the lowest meteorite flux. In this sense, it has been estimated that polar regions have 10% lower probability of meteorites impact than equatorial zones [87]. Therefore, apart from a high level of illumination, polar regions are also more attractive for preventing a high meteorite flux [76].
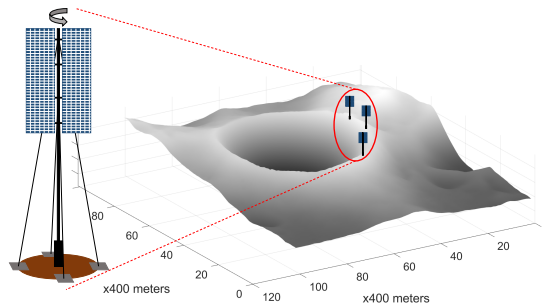
Fig. 2.3: Graphical representation of tall towers on the Shackleton crater rim with PV-modules [76].

Another important factor affecting the power production and accordingly the site selection is the temperature of the PV cells since it has been demonstrated that the series and shunt resistances of the PV-modules depend non-linearly on the temperature [70, 88, 89]. The PV cells efficiency is lower for high temperatures than for lower temperatures and it can reduce again at very low temperatures.

Finally, the degradation of PV cells on the Moon corresponds primarily to nuclei particles radiation, *e.g.* electrons and protons, which can be assumed to be distributed in omnidirectional spectrum [39].

2.3 The PV Technology for Space Applications

Nowadays, the space applications rely heavily on the use of multi-junction (MJ) PV cells due to their high efficiency, reasonable cost, mature manufacturing processes, and high resistance to radiative environments. For instance, the TJ-lattice matched (LM) GaInP/GaAs/Ge has shown efficiencies of around 30%. However, the mismatch between the lattice constants of the three layers makes the currents of layers to be different, preventing further improvement of the efficiency. In this regard, several attempts to overcome this issue have been focused mainly in the proposal of upright metamorphic (UMM) and inverted metamorphic (IMM) PV cells, which allow to optimize the currents between the subcells. These PV cells use buffer layers to progressively release the strain between the materials of different lattice constants [22, 76, 90].

A great advantage of using PV-modules for energy generation on the Moon is the lack of environmental issues regarding cloud coverage for instance. However, due to the absence of an atmosphere and magnetosphere, other kind of drawbacks come into play. Namely, impacts of micro-meteorites, highly energetic photons, and energetic nuclei particles, deep temperature cycles and vacuum, and electrostatic fields, to name a few [21, 76]. Even though all these issues degrade the PV cells, a special interest has been observed for the radiation-induced degradation due to the heavy damage induced to the solar cells, which depends on the type of particle, energy, flux, fluence, material of the cell, temperature, light intensity, *etc.* [39]. Some of the main advantages and disadvantages of the PV-technology for Lunar applications are provided in Table 2.2.

Therefore, the PV-modules for space applications must meet more strict requirements than for terrestrial applications. A comparison between the PV-technology for terrestrial and space applications is provided in Table 2.3.

Table 2.2: Advantages and disadvantages of the PV-technology for Lunar applications [76].

Tech.	Advantage	Disadvantage
PV	• Installation free of additional or heavy infrastructure and logistics. • Harmless for living beings and environment. • Modular. • Mature technology for space applications. • High level of RRROS.	• Power generation depends on several environmental factors. • Requirement of frequent cleaning due to Lunar dust addition on the PV-module surface. • Degradation due to highly energetic photons, nuclei particles, GCRs, micro-meteorites, deep vacuum, extreme temperatures cycles, electrostatic fields, *etc.*

Table 2.3: A comparison between the PV-technology for space and terrestrial applications [76].

Earth-based PV-technology	Space-based PV-technology
• Simpler architecture and normally cheaper. • Research focused on increasing efficiency while reducing manufacturing costs. • The main technology is based on Silicon. The highest laboratory-based efficiencies are about 26.7% for mono-crystalline and 24.4% for poly-crystalline structures [91, 92].	• More complex architectures to ensure a high efficiency and hardness to radiation. • Research focused not only on increasing efficiency and cost reduction, but more importantly the reduction of weight and increase of radiation shielding level, mechanical strength, tolerance to extreme temperature cycles, intense UV radiation, and vacuum. Besides, reduction of sensibility of efficiency to temperature fluctuations. • The main technology is based on MJ architectures with an efficiency of around 35% [93] or higher than 40% when light concentrators are utilized* [94].

* [95] recommends a concentration limit between 10 and 50 suns since the increment of complexity in the thermal dissipation system design.

2.4 Conclusion

The new concept of SMG is showing a high potential to be applied into the future space bases for ensuring a high level of RRROS. However, the

contemporary technology has to be improved in many aspects. Besides, challenges regarding the space environment should be faced. Talking specifically about the Moon, a complete knowledge of the terrain topography and accessibility to the POI, temperature ranges, ease of communication between different bases and/or orbiters and the Earth, availability of different type of natural resources and energy, radiation, among many other characteristics, is vital for the success of future long-term Lunar missions. Addressing the challenge of supplying uninterrupted energy to a future Lunar base, the allocation of PV-systems on the Lunar poles is demonstrating to be a promising solution. However, some of the proposals can be still considered unfeasible, such as the allocation of very tall towers, in the range of kilometers. Moreover, the Lunar environment is extremely harmful for the PV cells due to the presence of micro-meteorites, highly energetic photons and nuclei/ion particles, very deep temperature and vacuum levels, electrostatic fields, dust, *etc.* That is why the PV technology has to meet many more requirements than its terrestrial counterpart. A couple of tables at the end of this section provide the advantages and disadvantages of the PV technology for Lunar applications, as well as a comparison between its terrestrial and space applications.

Chapter 3

Modeling of PV-cells and a Proposal for an Improved Physical Model

3.1 Introduction

PV cell models with a physical meaning can be used straightforwardly to improve the designs of PV cells, which is a great asset for space applications. Besides, as previously emphasized, accurate models will assist the suitable development of ground-based test-benches. Moreover, apart from a point of view of design, accurate models with a short processing time might be ideal for online applications, such as monitoring, control, and real-time energy management [70].

So far, most of the models are based on the SD and DD approximations [41–45]. Diverse strategies based on analytical methods [42, 43], curve-fitting methods [46, 47] and improvements [96], system of non-linear equations [48–50], adaptive algorithms [97], heuristic algorithms [51–53], ANN [41,54,55], *etc.* have been proposed to model the PV cells/modules. However, most of these models lack a physical meaning that narrows down their application under different conditions of temperature and irradiance for instance. Table 3.1 shows a summary of different strategies proposed to model the PVs along with their advantages and drawbacks.

In this sense, some attempts to develop physical-based PV cell models have been reported. Physical expressions for the SD and DD models have been presented in [100] and [101], respectively, with a good accuracy in the whole range of voltage and several light intensities. However, the models have been tested only for temperatures above the RT and the expressions

Table 3.1: Different strategies based on the SD and DD approximations to model PV cells/modules [70].

Strategy	Advantage	Drawback
Analytical	Simple expressions.	Accuracy decreased due to assumptions done.
Curve-fitting	Highly accurate at the MPP.	Inaccuracies in regions away from the MPP.
Improved curve-fitting	High accuracy in whole voltage range for temperatures above room temperature (RT).	Assumption of constant shunt resistance*.
System of non-linear equations	High accuracy on the MPP while using the datasheet parameters.	Solution highly depends on the initial guesses.
Adaptive algorithm	Accuracy above the RT while ensuring convergence to a solution.	Empirical expression for the shunt-resistance while series-resistance is assumed constant*.
Heuristic algorithms	Highly accurate in the whole voltage range and for a wide range of light intensities and temperature.	Slow and requires many experimental curves.
ANNs	High accuracy while no need of mathematical expressions.	It is particular for a module and requires a lot of experimental data.

* Other studies suggest a dependency of the shunt and series resistances on the light intensity and temperature [88,89,98,99].

for the series and shunt resistances are semi-empirical, thereby jeopardizing the physical representation of the PV cell/module. Another attempt has proposed to use a triple diode model with dark IV-curves, which shows a good accuracy with the experimental profiles [102]. Nonetheless, the study is limited to just one temperature. Therefore, yet more sophisticated models are required, which should be:

1. Highly accurate in the whole range of voltage from zero up to the open-circuit condition, and in a wide range of temperatures and light intensities.

2. Fast enough for real-time applications.

3. Independent of experimental data as much as possible.

4. Based on the physics of the PV cell.

3.2 Single and Double Diode Approximations for PV Modeling

The physical model of a PV cell has been carried out mostly by using four well established configurations based on electrical equivalent circuits. The simplest approximation refers to the ideal model where no losses are considered [42,43], see Fig. 3.1(a). The next configuration is the SD equivalent circuit where the losses are taken into consideration by means of series and shunt resistances [44, 52], see Fig. 3.1(b). However, usually the shunt resistance is neglected. In the third approximation, a second diode parallel to the first diode is included to represent the recombination current in the depletion region [47, 50, 103], see Fig. 3.1(c). And finally, multi-diode approximations have been also reported in the literature [104], see Fig. 3.1(d). The SD and DD equivalent circuits are discussed in the following. Besides, some strategies to compute the parameters of the circuits are introduced.

3.2.1 Single Diode Model

The SD model features a current source called I_{ph}, which represents the photo-generated current, and a diode in shunt to model the currents of diffusion and recombination. Besides, the losses due to the load current is directly represented by a concentrated equivalent series resistance, R_s, while the losses due to leakage currents by a shunt resistance called
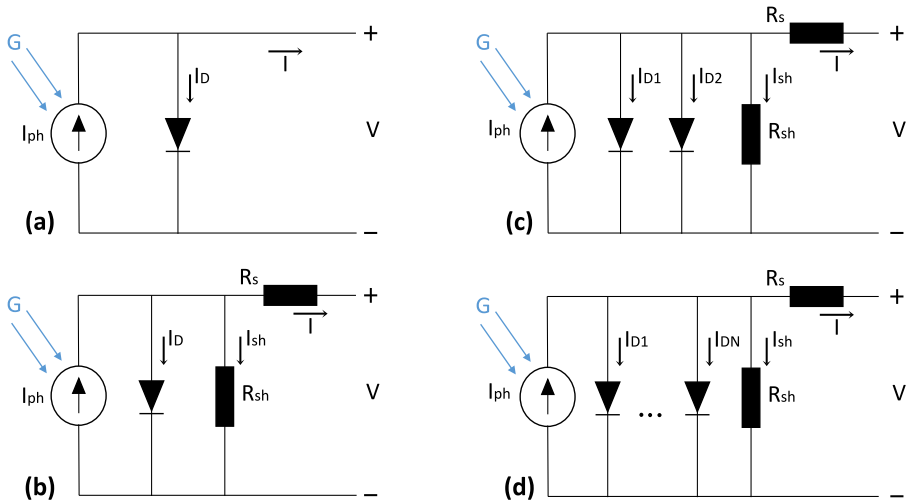
Fig. 3.1: Electrical equivalent circuits for the PV cells. (a) Ideal equivalent circuit. (b) SD model. (c) DD model. (d) Multi-diode model.

R_{sh} [44, 47, 52, 104], see Fig. 3.1(b). The general equation for a single cell is expressed by

$$I_c = I_{ph,c} - I_{0,c} \left[\exp \left(\frac{V_c + I_c R_{s,c}}{a_c} \right) - 1 \right] - \frac{V_c + I_c R_{s,c}}{R_{sh,c}}, \qquad (3.1)$$

where $a_c = mV_T$. In (3.1), m is the ideality factor while $V_T = kT/q$ represents the thermal voltage, which is comprised of the Boltzmann constant $k \approx 8.62 \times 10^{-5}$ $[eV/K]$, temperature of the cell T $[K]$, and the elementary charge $q \approx 1.6021 \times 10^{-19}$ $[C]$. I_c, $I_{ph,c}$, and $I_{0,c}$ represent the load current, photo-generated current, and reverse saturation current of a single cell, respectively. Besides, $R_{s,c}$ and $R_{sh,c}$ represent the series and shunt resistances and V_c the output voltage of a single cell.

On the other hand, the expression for a PV-module comprised of n_p parallel strings of n_s PV cells in series is expressed as [43, 46, 48, 105]

$$I = I_{ph} - I_0 \left[\exp \left(\frac{V + I R_s}{a} \right) - 1 \right] - \frac{V + I R_s}{R_{sh}}, \qquad (3.2)$$

where the equivalent parameters are

$$I = n_p I_{ph,c} \quad R_s = \left(\frac{n_s}{n_p} \right) R_{s,c} \quad a = n_s a_c$$
$$I_0 = n_p I_{0,c} \quad R_{sh} = n_s R_{sh,c}.$$

Actually, this model is usually called five-parameters model due to the five unknown values to be computed (I, I_0, R_s, R_{sh}, a). In this regard, several attempts to estimate such parameters have been introduced in the literature. Some important approximations are listed in this thesis as *W. D. Soto Solution* [48], *M. G. Villalva Solution* [46], and *D. Sera Solution* [49].

W. D. Soto Solution

In this approximation, the five parameters of the SD equivalent circuit have been computed with the following translating equations [48].

$$I_0 = I_0^{stc} \left(\frac{T}{T_{stc}} \right)^3 \exp \left[\frac{1}{k} \left(\left. \frac{E_g}{T} \right|_{stc} - \frac{E_g}{T} \right) \right], \qquad (3.3)$$

$$I_{ph} = \frac{G}{G_{stc}} \frac{M}{M_{stc}} \left(I_{ph}^{stc} + \alpha_{isc} \Delta T \right), \qquad (3.4)$$

$$a = a_{stc} \frac{T}{T_{stc}}, \qquad (3.5)$$

$$R_s = R_s^{stc}, \qquad (3.6)$$

$$R_{sh} = R_{sh}^{stc} \frac{G_{stc}}{G}, \qquad (3.7)$$

where the bandgap energy dependency on the temperature is computed by a linear approximation $E_g = E_g^{stc}(1 - 0.0002677\Delta T)$ and $\Delta T = T - T_{stc}$. The bandgap energy of Silicon at STCs is approximately 1.12 $[eV]$. Besides, G represents the solar light intensity in $[W/m^2]$, M is the air mass modifier, and α_{isc} shows the temperature coefficient for the short-circuit current. Moreover, the series resistance, R_s, is assumed to be constant independent of the temperature and light intensity while the shunt resistance, R_{sh}, is approximated by an empirical equation depending on the inverse of the light intensity. Finally, the parameters having the subscript "stc" refer to the corresponding variables at STCs, which are proposed to be the solution of a system of non-linear equations.

M. G. Villalva Solution

In this approximation, the five parameters of the SD model are computed by the following translating equations [46].

$$I_{ph} = \left(I_{ph}^{stc} + \alpha_{isc}\Delta T\right)\frac{G}{G_{stc}}, \tag{3.8}$$

$$I_0 = \frac{I_{sc}^{stc} + \alpha_{isc}\Delta T}{\exp\left[(V_{oc}^{stc} + \beta_{voc}\Delta T)/a\right] - 1}, \tag{3.9}$$

$$R_{sh} = \frac{V_{mp}^{stc} + I_{mp}^{stc}R_s}{I_{ph}^{stc} - I_0^{stc}\exp\left[(V_{mp}^{stc} + I_{mp}^{stc}R_s)/a^{stc}\right] + I_0^{stc} - I_{mp}^{stc}}, \tag{3.10}$$

$$R_s \rightarrow \text{Increased progressively}, \tag{3.11}$$

$$1.0 \leq m \leq 1.5, \rightarrow \text{Chosen arbitrarily}, \tag{3.12}$$

where $I_{ph}^{stc} = \frac{R_{sh}+R_s}{R_{sh}}I_{sc}^{stc}$. Besides, I_{sc} represents the short-circuit current while V_{oc} is the open-circuit voltage and β_{voc} is its thermal coefficient. The subscript "mp" indicates that the corresponding parameter is at the MPP. In this technique, the value of R_s is increased progressively while the shunt resistance in (3.10) is updated. The iterative method finishes when the error between the maximum power estimated and the datasheet value are lower than a predefined value δ.

D. Sera Solution

The authors of [49] propose to use the superposition principle to take into account the influence of temperature and light intensity on two parameters of I_0 and I_{ph}. The other three parameters (R_s, R_{sh}, and m) are computed by solving numerically a system of non-linear equations. Then, they are assumed constant regardless of the temperature and light

intensity. The translating equations for the reverse saturation current and the photo-generated current are proposed as follows.

$$I_0(T) = \left[I_{sc}(T) - \frac{V_{oc}(T) - I_{sc}(T)R_s}{R_{sh}} \right] \exp\left[-\frac{V_{oc}(T)}{a^{stc}} \right], \qquad (3.13)$$

$$I_{ph}(T) = I_0(T) \exp\left[\frac{V_{oc}(T)}{a^{stc}} \right] + \frac{V_{oc}(T)}{R_{sh}}, \qquad (3.14)$$

$$I_{ph}(G) = I_{ph}^{stc} \left(G/G_{stc} \right). \qquad (3.15)$$

where the dependency of the open-circuit voltage and short-circuit current on the temperature are expressed as,

$$V_{oc}(T) = V_{oc}^{stc} + \beta_{voc}\Delta T, \qquad (3.16)$$

$$I_{sc}(T) = I_{sc}^{stc} + \alpha_{isc}\Delta T, \qquad (3.17)$$

3.2.2 Double Diode Model

The DD model is usually proposed to improve the accuracy of the physical approximation to the PV cell but having a longer processing time [52]. The second diode is placed in parallel to the first diode, see Fig. 3.1(c), and aims to represent the recombination current that takes place in the depletion zone [103, 106]. The general expression is quite similar to (3.2) while having a second exponential term corresponding to the second diode as follows

$$I = I_{ph} - I_{01} \left[\exp\left(\frac{V + IR_s}{a_1} \right) - 1 \right] - I_{02} \left[\exp\left(\frac{V + IR_s}{a_2} \right) - 1 \right] - \frac{V + IR_s}{R_{sh}}, \qquad (3.18)$$

where the subscripts "1" and "2" correspond to diode 1 and 2, respectively. This model contains seven parameters to be estimated. In this sense, a popular approximation introduced by [103] to compute these parameters is discussed in the following.

Z. Salam Solution

In this iterative approximation proposed by [103], the series resistance, R_s, is increased progressively and the shunt resistance, R_{sh}, is updated in a similar way to (3.10), but using (3.18) instead of (3.2). The algorithm ends when the error between the estimated and the values provided by the datasheet at MPPs is lower than a predefined value δ. The translating equations are

expressed as follows.

$$I_{ph} = \frac{G}{G_{stc}} \left(I_{ph}^{stc} + \alpha_{isc}\Delta T \right),$$ (3.19)

$$I_{01} = I_{02} = \frac{I_{sc}^{stc} + \alpha_{isc}\Delta T}{\exp\left[(V_{oc}^{stc} + \beta_{voc}\Delta T)/V_T\right] - 1}.$$ (3.20)

$$R_s \rightarrow \text{Increased progressively,}$$ (3.21)

$$m_1 = 1.0,$$ (3.22)

$$m_2 \geq 1.2.$$ (3.23)

3.3 An Improved Physical Model for PV Modules

New expressions for the translating equations of the series and shunt resistances of a SD equivalent model have been proposed, which are based on the equation for resistivity of extrinsic semiconductors. Besides, a physics-based expression for the bandgap energy has been updated based on reports of narrowing effects under different situations. Fig. 3.2 provides a graphical view of the SD model elements modified to find the proposed translating equations.

The translating equations for three elements of the SD equivalent model have been either proposed or updated in this thesis. The aim was to increase the accuracy of the approximation for the whole voltage range and a wider range of temperatures and light intensities. The expression for the bandgap energy is updated by adding a narrowing effect due to the doping concentration. On the other hand, the proposed translating equation for
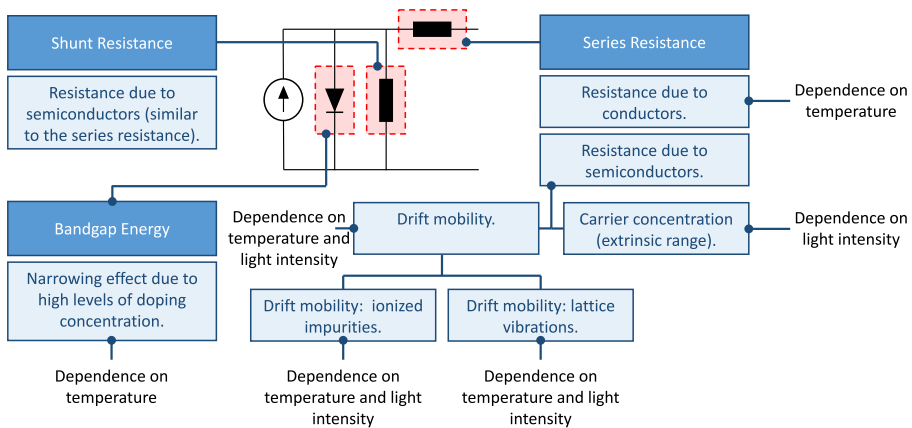
Fig. 3.2: Elements of the SD model improved by the new physical approximation.

the series resistance considers the conductive and semi-conductive parts, which is assumed to be always in the extrinsic stage. Finally, the translating equation for the shunt resistance is the same as the expression for the series resistance without the conductive part, see Fig. 3.2. A graphical representation of a generic single junction (SJ) PV cell with the concentrated elements of the SD equivalent model is shown in Fig. 3.3. The shunt resistance is allocated in the frontiers of the crystal whereas the series resistance corresponds to the flow of the photo-generated current through the semiconductor and metallic connectors to the load.

3.3.1 Bandgap Energy Expression

It is shown that the bandgap energy is narrowed down when [107–110]

1. the temperature increases,

2. the doping concentration increases.

In this sense, a new constant term, δE_g, has been added to the traditional thermal dependent expression for the bandgap energy as follows [70].

$$E_g = E_{g,0} - \frac{\alpha T^2}{T + \beta} - \delta E_g,$$ (3.24)

where δE_g represents the narrowing effect in the bandgap of the intrinsic semiconductor material due to the doping while it is assumed to be a tuning parameter of the model, which should be in the range of $[meV]$. Besides, the projected bandgap at $0\ [K]$ is represented by $E_{g,0}$. For the case of Silicon, $E_{g,0} \approx 1.169\ [eV]$, $\alpha \approx 4.9 \times 10^{-4}\ [eV/K]$, and $\beta \approx 655\ [K]$ [107].
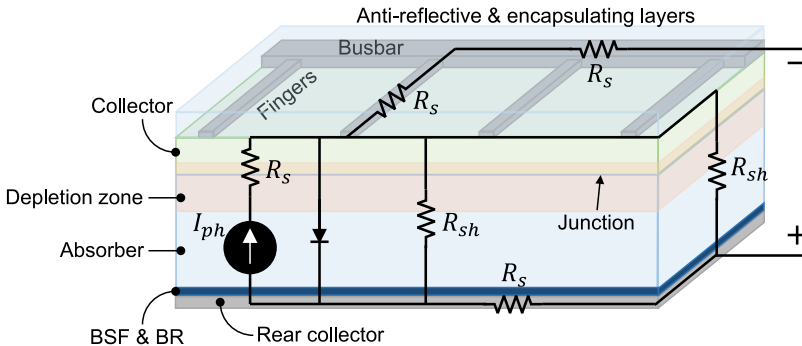
Fig. 3.3: Graphical representation of the equivalent SD model. Adapted from [70].

3.3.2 Series Resistance Expression

As shown in Fig. 3.2, the series resistance has been proposed to be comprised of a conductive and semi-conductive part [70].

Resistance Due to Conductors

Based on the theory discussed in [111], the resistance in the PV cell that belongs to the conductors like the fingers and busbar, can be expressed as [70]

$$R_{s1} \approx R_s^{stc} \left(1 + \alpha_0 \Delta T\right), \tag{3.25}$$

where α_0 is the temperature coefficient of the conductors at STCs. Besides, the translating equation is in terms of the parameter at STCs, R_s^{stc}.

Resistance Due to Semiconductors

The semi-conductive part of the series resistance is proposed to be expressed based on the conductivity of semiconductors. The general expression is [112]

$$\sigma = qn\mu_n + qp\mu_p, \tag{3.26}$$

where n and p represent the electrons and holes concentrations (carrier concentrations), respectively. Besides, μ_n and μ_p are the drift mobilities of electrons and holes, respectively. As can be seen in Fig. 3.2 and (3.26), the resistance due to semi-conductors should be in terms of the carrier concentrations and mobilities, which have been updated in the following way.

Carrier Concentration (Extrinsic Range): For the development of the carrier concentration expression, the semiconductors of the PV cell are assumed to have enough thermal energy to be on the extrinsic region. Besides, it is assumed that the extrinsic semiconductors have been doped enough to neglect the intrinsic carriers due to a high concentration of donors (in case of a *n-type* semiconductor). Thereby, the carriers concentration in presence of light can be expressed as follows [70, 112].

$$n \approx N_d + \delta n, \tag{3.27}$$
$$p \approx \delta p, \tag{3.28}$$

where $\delta n = \delta p$. Besides, N_d is the donors concentration (for the case of an *n-type* semiconductor) and $\delta p = \delta n$ is the average excess of carrier concentration created by the photo-generation. Therefore, regarding (3.27) and (3.28) (and similar for a *p-type* semiconductor), the conductivity

expressed in (3.26) can be arranged for both kinds of semiconductors (*n-type* and *p-type*) as follows [70].

$$\sigma_n = q\mu_n N_d \left[1 + \frac{\delta n}{N_d}\left(1 + F_\mu\right)\right], \tag{3.29}$$

$$\sigma_p = q\mu_p N_a \left[1 + \frac{\delta n}{N_a}\left(1 + F_\mu^{-1}\right)\right], \tag{3.30}$$

where $F_\mu = \mu_p/\mu_n$. Besides, the subscripts d and a represent "donors" (electrons) and "acceptors" (holes). The amount of extra carriers due to the photo-generation is expressed as [70]

$$\delta n = \left(\frac{G}{G_{stc}}\right)\frac{\tau_r}{hcW}\int_{AM1.5G}\eta_\lambda F_\lambda \lambda d\lambda, \tag{3.31}$$

$$\eta_\lambda = \frac{hc}{q\lambda}SR(\lambda), \tag{3.32}$$

where τ_r [s] represents an average value between the bulk and surface recombination times, $h \approx 6.626 \times 10^{-34}$ [Js] is the Planck's constant, $c \approx 3 \times 10^8$ [m/s] is the speed of light, W [m] is the semiconductor wafer thickness, η_λ is the external quantum efficiency (EQE), F_λ [$W/m^2 - nm$] is the spectral irradiance, λ [nm] is the photon wavelength, and SR [A/W] is the spectral response of the semiconductor [112–114].

Drift Mobility: The carriers mobility is expressed by the Matthiessen's rule as

$$\frac{1}{\mu_n} = \frac{1}{\mu_I} + \frac{1}{\mu_L}, \tag{3.33}$$

And,

$$\mu \propto \tau = \frac{1}{SvN_s}, \tag{3.34}$$

where τ is defined as the average time between two consecutive scattering events, S is the average scattering cross-section, v is the mean velocity of the carriers also known as thermal velocity, and N_s is the concentration of scatterers [112]. Besides, the subscript "n" refers to an *n-type* semiconductor, which should be changed to "p" for *p-type*. Moreover, the total mobility of the electrons in the conductive band (CB) and holes in the valence band (VB) is affected largely by the lattice vibrations and ionized impurities. Thus, μ_L and μ_I are known as the mobility due to lattice vibrations and ionized impurities, respectively. Such mobilities are addressed in more detail in the following.

Drift Mobility - Lattice Vibrations: The expression for μ_L is formulated by considering the following,

1. The average cross-section area of the scatterers, S, is affected by the temperature as $S \propto (3/2)kT$ [112].

2. The concentration of scatterers, N_s, is assumed uniform and constant through the semiconductor.

3. The mean kinetic energy (KE) of the carriers, $(3/2)kT$, is assumed to be increased temporarily by the action of the photon absorption in a magnitude δE. Therefore, regarding that $T = (1/2)mv^2$, then $v \propto \left(\frac{3}{2}kT + \alpha_{ph}\frac{G}{N}\right)^{1/2}$. N [$\#photons/s - m^2$] represents the global photon flux and α_{ph} the average ratio of the energy gained by the electron from the photon to the total energy contained in the impacting photon [70, 112].

Thereby, the part of the total carrier drift mobility taking into account the lattice vibrations is formulated as [70],

$$\frac{1}{\mu_L} \propto T g_\alpha^{1/2}, \tag{3.35}$$

$$g_\alpha = \frac{3}{2}kT + \alpha_{ph}\frac{G}{N}. \tag{3.36}$$

Drift Mobility - Ionized Impurities: The expression for the drift mobility of the carriers regarding the action of the ionized impurities in the material (Coulombic attractions) is formulated by [70] considering the following,

1. Given that the scatterer cross section area, S, is the circular area with a radius of length where the KE and potential energy (PE) are numerically the same, then $S \propto \mathrm{KE}^{-2}$. And assuming again that carriers will increase their KE by the action of photons, then $S \propto g_\alpha^{-2}$.

2. The concentration of scatterers, N_s, is assumed uniform and constant across the semiconductor.

3. The thermal velocity is again considered as $v \propto g_\alpha^{1/2}$.

Therefore, the drift mobility regarding the action of ionized impurities is expressed as [70],

$$\frac{1}{\mu_I} \propto g_\alpha^{-3/2}. \tag{3.37}$$

Table 3.2: Main features assumed for the proposed translating equations [70]

Parameter	Assumption
Operation	Semiconductors: Extrinsic region.
Doping concentration	$N_a = N_d$, $n \ll N_c$, $p \ll N_v$ (Non-degenerative).
Doping profile	Uniform across the PV cell.
SRV	Non passivated cells.
τ_r	Constant.
W	Constant $\forall$ layers, $W \gg$ Absorption Depth.
Injection level	Low.
Mobility ratio	$F_\mu = \mu_p / \mu_n = 1$.

Then, the total drift mobility expressed by the Matthiessen's rule in (3.33) is finally formulated as follows [70],

$$\frac{1}{\mu_n} = \gamma_{n1} g_\alpha^{-3/2} + \gamma_{n2} T g_\alpha^{1/2}, \tag{3.38}$$

where γ_{n1} and γ_{n2} are proportional constants. Besides, "n" is particular for the *n-type* semiconductor and should be changed to "p" when *p-type* is considered.

The main features assumed for this model are presented on Table 3.2. Then, as $R \propto 1/\sigma$ and considering the expression for the conductivity in (3.29) or (3.30) and the expression for the total drift mobility in (3.38), the series resistance due to the semiconductor can finally be written as,

$$\frac{R_{s2}}{R_s^{stc}} = \left(\frac{\Omega_{stc}}{\Omega} \right) \left[A\phi^{-3/2} + (1 - A) \left(\frac{T}{T^{stc}} \right) \phi^{1/2} \right], \tag{3.39}$$

$$\Omega = 1 + 2\frac{\delta n}{N_d}, \tag{3.40}$$

$$\phi = g_\alpha / g_{\alpha,stc},$$

where A is a constant coming from the algebraic process and it is considered as a tuning parameter.

Series Resistance

The total series resistance is then comprised of a conductive, (3.25), and a semi-conductive, (3.39), resistances connected in series. Therefore, the expression for the total resistance in series is given as follows,

$$R_s = \Gamma_R R_{s1} + (1 - \Gamma_R) R_{s2}, \tag{3.41}$$

where the fraction of the conductive to the total resistance in series is represented by the tuning parameter Γ_R.

3.3.3 Shunt Resistance Expression

Even though the resistance in parallel is usually assumed to be a leakage current that flows through the surface of the semiconductor crystal or the grain boundaries in case of a poly-crystalline [112], for this model, it was assumed that resistance has a semi-conductive behavior. In other words, the shunt resistance is modeled by the expression given in (3.39) but written as follows [70],

$$\frac{R_{sh}}{R_{sh}^{stc}} = \left(\frac{\Omega_{stc}}{\Omega}\right) \left[B\phi^{-3/2} + (1-B)\left(\frac{T}{T^{stc}}\right)\phi^{1/2}\right], \tag{3.42}$$

where B is the corresponding tuning parameter.

3.3.4 Equations for the Physical Model Proposed

The last subsections have described the translating equations of the series (3.41) and shunt (3.42) resistances, which are in terms of temperature and light intensity. Besides, an updated version of the bandgap energy expression (3.24) was proposed. The translating equations corresponding to the reverse saturation current, I_0, photo-generated current, I_{ph}, and ideality factor, a, are expressed by (3.3), (3.4), and (3.5), respectively. Apart from that, the actual temperature of the cell should be computed. In this sense, it has been stated that the real temperature of a PV cell will differ from the temperature measured at the rear side of the cell [115, 116]. In fact, a linear expression for the actual temperature in terms of the light intensity has been proposed for PV-modules as [70, 117],

$$T = T_m + \frac{G}{G_{stc}}\Delta T, \tag{3.43}$$

where ΔT has been proposed to be around $2 \sim 4\ [°C]$ for flat plate modules. Moreover, it should be noticed that all the translating equations for the proposed model are in terms of the corresponding variables but in STCs. Additionally, five tuning parameters are observed for this model.

Regarding the parameters in STCs, a heuristic algorithm can be applied to the current-voltage (IV)-characteristics, usually provided on the datasheet, to compute the five parameters at STCs as long as the solution is constrained by realistic values. Indeed, the teaching-learning based optimization (TLBO) has been used in this thesis for this task [51, 70]. Table 3.3 provides the tuning parameters and the ranges in which normally their values are bounded. The ranges for A, B, and δE_g were defined by experience during the modeling process. It is worth mentioning that some iterative techniques might be used in order to optimize the tuning parameters. However, the reduction in the number of tuning parameters is much better and it should be done by doing more mathematical analyses using physical laws.

Table 3.3: Tuning parameter ranges for the improved physical model proposed [70]

Parameter	Description	Range
A	Proportional constant, R_s	[0,1.5]
B	Proportional constant, R_{sh}	[0,1.5]
Γ_R	Portion of conductive R_s	[0,1.0]
ΔE_g	Narrowing effect, E_g	$\leq 90\ [meV]$ *
		$\geq 90\ [meV]$ **
α_{ph}	Carrier-KE / photon-energy	(0,1.0)

* Poly-crystalline. ** Mono-crystalline.

3.4 Results and Discussion

The overall process for the simulations is presented in the flowchart diagram of Fig. 3.4. For this study, six different PV-modules were simulated. One corresponds to a physical module located on the roof of the PV-lab at Aalborg University. A second module was simulated by means of the software package *PC1D*. The last three modules were modelled by extracting the datasheet information, two poly-crystalline (PC) and one mono-crystalline (MC) technologies. The basic information of each module is presented in Table 3.4.

Then, the TLBO algorithm was utilized to process the measured data and get the five parameters R_s, R_{sh}, I_0, I_{ph}, and a under STCs. Afterwards,

Table 3.4: Basic information of the PV-modules used for the simulations [70]

	KK280P	JAP60S01	REC245PE	PC1D	M-60
	Datasheet parameters				
I_{sc}^{stc}	9.53	9.18	8.80	7.9755	9.08
V_{oc}^{stc}	38.9	38.17	37.10	39.324	37.90
n_s	60	60	60	60	60
V_{mp}^{stc}	31.50	31.13	30.10	34.4085	30.80
I_{mp}^{stc}	8.89	8.67	8.23	7.6232	8.60
α_{isc}	0.00559	0.00532	0.002112	0.000251	0.003632
β_{voc}	-0.138	-0.12596	-0.10017	-0.12416	-0.12128
	PV parameters under STCs (computed by the TLBO algorithm)				
I_{ph}^{stc}	9.52731	9.18789	8.69404	7.97837	9.07735
I_0^{stc}	1.45198	0.17515	61.7734	0.06194	19.32055
R_s^{stc}	0.27686	0.21724	0.26557	0.01382	0.15082
R_{sh}^{stc}	190.645	501.121	2094.48	5000	594.029
a^{stc}	1.72293	1.54662	1.91299	1.53731	1.89903

Note: α_{isc} is in $[A/^oC]$, β_{voc} in $[V/^oC]$, and I_0^{stc} in $[nA]$.

the translating equations of the respective model are processed and the IV response is obtained for a specific temperature and light intensity. The simulation was carried out in two ways. Firstly, the extra carriers due to the photo-generation, δn was not taken into consideration. This model was called *Model 1*. The second model, also called *Model 2*, takes into consideration the extra carriers generated by the photo-generation, see (3.31). However, the implementation of *Model 2* requires additional information provided in [70]. The tuning parameters for each model are shown in Table 3.5.

The accuracy of each model was carried out by means of the mean absolute error in power (MAEP) introduced by [96, 100] and defined as
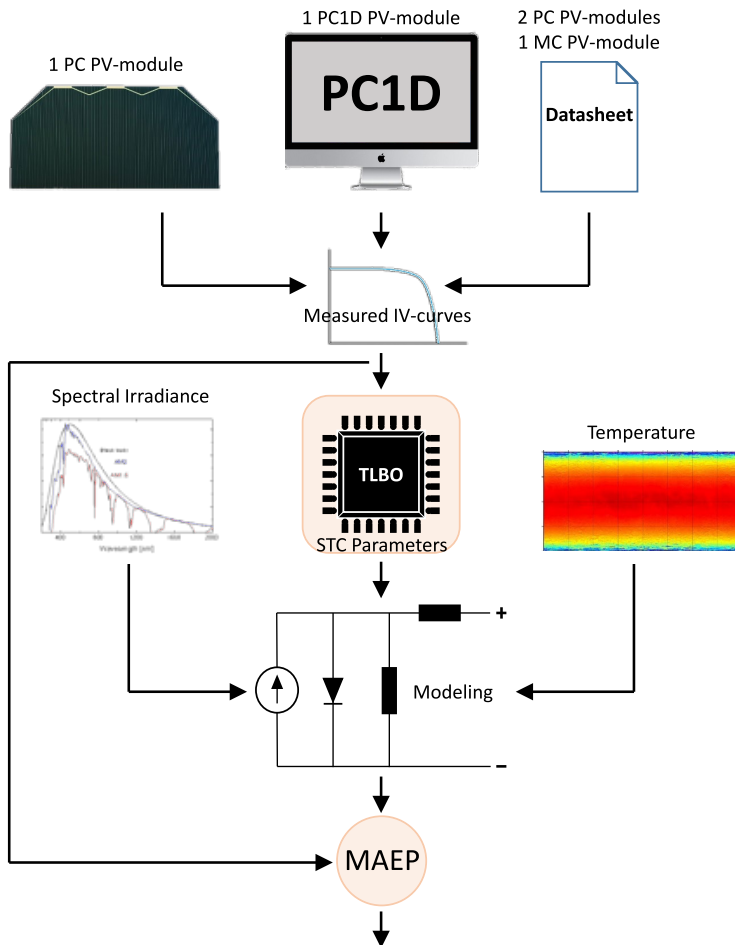

Fig. 3.4: The simulation process.

Table 3.5: Tuning parameters for the six models implemented and each PV-module [70]

Param.	KK280P	JAP60S01	REC245PE	PC1D	M-60
			PV-Module		
			Model 1 and *Model 2* (SD) [70]		
A	1.004240	0.18	0.0064	-	-
B	0.516975	0.55	0.32	1.50	0.121
Γ_R	0.954569	0.15	0.30	1.0	1.0
ΔE_g	80.645	32.25	70	6.5	223.75
α_{ph}	0.25	0.099	0.1485	0.03542	0.3264
			Salam approximation (DD) [103]		
m_2	1.53	1.20	1.20	1.20	1.60
			Villalva approximation (SD) [46]		
m	1.10	1.0	1.35	1.025	1.25

Note: the ideality factor for diode 2 is m_2. ΔE_g is in $[meV]$.

follows for the *i-th* IV-characteristics,

$$MAEP_i = \frac{\sum |P_{mes,k} - P_{mod,k}|}{N_p}, \quad k = 1, \ldots, N_p, \quad (3.44)$$

where P_{mes} and P_{mod} refer to the measured and modelled power profiles while N_p is the number of sampling points in each curve. The MAEP is assessed in the whole voltage range and around the MPP. Furthermore, as an attempt to evaluate the model in all the possible conditions of temperatures and light intensities, the MAEP curves are averaged as follows,

$$MAEP_{av} = \frac{\sum MAEP_i}{N_{curves}}, \quad i = 1, \ldots, N_{curves}, \quad (3.45)$$

where N_{curves} is the number of curves. Finally, the root mean square error (RMSE) is also assessed for the same ranges.

The MAEP for each model, module, irradiance, and temperature is graphically deployed on Fig. 3.5 [70]. It should be noticed that curves on row 4 from top to bottom correspond to experimental curves of the PV-module REC245PE. Neither the temperature in the first two columns from left to right, nor the light intensity in the last two columns are indicated since these values were different from each other. The rear surface temperatures in the points of Fig. 3.5(13)-(14) from left to right are $25.9, 25.3, 24.1, 25.1, 25.3$ $[°C]$. The light intensity in the points of Fig. 3.5(15)-(16) from left to right are $205, 255, 842, 219, 1007$ $[W/m^2]$. From these plots, it is easy to see how the proposed *Model 1* and *Model 2* are more accurate in the majority of conditions not only around the MPP, but also in the whole voltage range. *Model 2* is a little more accurate than *Model 1* when the light intensity changes, such as observed on the first two columns from left to right, Fig. 3.5.
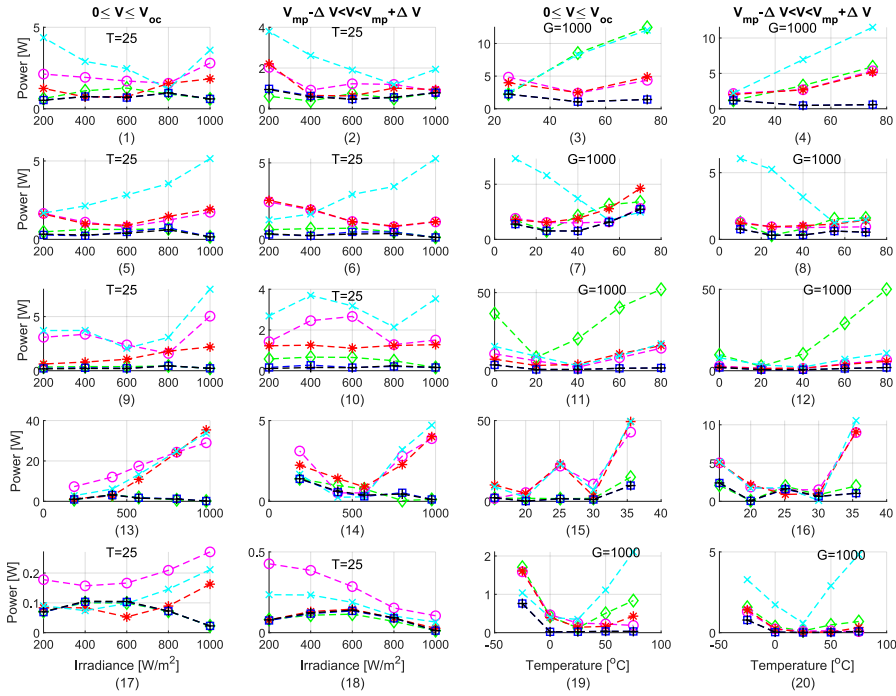
Fig. 3.5: MAEP for the six implemented PV-models. Column 1 and 2 (from left to right) present the MAEP at different light intensities for a voltage from 0 to V_{oc} and near to the MPP. Column 3 and 4 (from left to right) presents the MAEP at different temperatures for a voltage from 0 to V_{oc} and near to the MPP. From top to bottom, row 1 corresponds to the module KK280P3CD3CG, row 2 to the module JAP60S01270SC, row 3 to the module M60, row 4 to the module REC245PE, and row 5 to the module PC1D. Green Diamond: SD D.Soto. Pink circle: DD Salam. Red asterisk: SD Villalva. Blue cross: SD Sera. Blue square: SD *Model 1*. Black plus: SD *Model 2*.

The average MAEP values estimated with (3.45) for each module, model, and different levels of light intensity are shown in Table 3.6. Similarly, the mean MAEP values, but for different temperatures are provided in Table 3.7. The minimum value of MAEP for each module is bold typed while the lowest two values are highlighted in light gray. Therefore, according to the results, the proposed *Model 1* and *Model 2* are always in the lowest values of average MAEP. This shows the higher accuracy of the proposed approximations for a much wider range of temperatures and light intensities and not only around the MPP, but also in the whole voltage range from zero up to the open-circuit voltage.

Furthermore, Table 3.8 shows the average RMSE for each model and module for different levels of light intensities. On the other hand, Table 3.9 shows the average RMSE for each model and module for different levels of temperatures. Likewise, the lowest values of RMSE for each module are

Table 3.6: $MAEP_{av}$ for the six models and PV-modules. Several light intensities [70].

Module	A	B	C	D	*Model 1*	*Model 2*
			$0 \leq V \leq V_{oc}$			
KK280P	0.9018	2.0244	1.2194	2.9094	0.7090	**0.7086**
JAP60S01	0.5161	1.2969	1.3790	3.0688	0.3767	**0.3537**
REC245PE	**1.3757**	18.0345	14.9079	16.1447	1.4438	1.4019
PC1D	**0.0730**	0.1962	0.0943	0.1238	0.0741	0.0751
M-60	0.3509	3.0948	1.2941	4.0221	0.2741	**0.2497**
			$V_{mp} - \Delta V < V < V_{mp} + \Delta V$			
Module	A	B	C	D	*Model 1*	*Model 2*
KK280P	**0.6062**	1.2475	1.0887	2.2887	0.6870	0.6697
JAP60S01	0.5377	1.5028	1.5417	2.9210	0.3301	**0.2937**
REC245PE	0.6619	2.1668	2.1661	2.0229	**0.5833**	0.5948
PC1D	**0.0773**	0.2710	0.0941	0.1649	0.0859	0.0892
M-60	0.5091	1.8660	1.2206	3.0480	0.1913	**0.1626**

A: D. Soto solution [48]; B: Salam solution [103]; C: Villalva solution [46];
D: Sera solution [49].

Table 3.7: $MAEP_{av}$ for the six models and PV-modules. Several Temperatures [70].

Module	A	B	C	D	*Model 1*	*Model 2*
			$0 \leq V \leq V_{oc}$			
KK280P	7.7474	3.8610	3.7828	7.6119	**1.5745**	**1.5745**
JAP60S01	2.2357	1.8638	2.5242	4.2067	**1.4417**	**1.4417**
REC245PE	4.4608	16.5264	18.1640	18.2104	**2.9509**	2.9967
PC1D	0.7196	0.5435	0.5482	1.0006	**0.1748**	**0.1748**
M-60	31.6314	8.4136	8.3520	10.9760	**1.7181**	1.7187
			$V_{mp} - \Delta V < V < V_{mp} + \Delta V$			
Module	A	B	C	D	*Model 1*	*Model 2*
KK280P	3.4641	3.4009	3.2835	6.8969	**0.7464**	**0.7464**
JAP60S01	1.0997	0.9957	1.1559	3.4388	**0.5130**	**0.5130**
REC245PE	1.4043	3.7778	3.6210	3.8585	**1.1483**	1.1652
PC1D	0.6456	0.3602	0.4063	2.6676	**0.1846**	**0.1846**
M-60	20.4090	3.2953	2.9785	6.3183	**1.3026**	1.3038

A: D. Soto solution [48]; B: Salam solution [103]; C: Villalva solution [46];
D: Sera solution [49].

typed in bold fonts while the two lowest values are highlighted in light gray color. These results also show the superiority in accuracy of the proposed *Model 1* and *Model 2* over the other ones and not only around the MPP, but also in the whole voltage range from zero up to the open-circuit voltage.

Finally, Fig. 3.6 shows the 3D profile of the series resistances for the proposed *Model 1* and *Model 2* corresponding to the PV-module JAP60S01. It

Table 3.8: RMSE for the six models and PV-modules. Several light intensities [70].

$\frac{1}{N}\sum_{\forall N} RMSE_N$ $0 \leq V \leq V_{oc}$						
Module	A	B	C	D	*Model 1*	*Model 2*
KK280P	1.3137	2.8525	1.5932	3.9898	**1.0095**	1.0111
JAP60S01	0.7141	1.6432	1.7735	4.6595	0.5725	**0.5338**
REC245PE	1.6662	20.9017	17.4257	18.8156	1.6931	**1.6378**
PC1D	**0.2240**	0.3041	0.2313	0.2674	0.2269	0.2280
M-60	0.4484	4.9867	1.6724	6.0045	0.4360	**0.3891**
$\frac{1}{N}\sum_{\forall N} RMSE_N$ $V_{mp} - \Delta V < V < V_{mp} + \Delta V$						
Module	A	B	C	D	*Model 1*	*Model 2*
KK280P	**0.7261**	1.4178	1.2936	2.6797	0.7829	0.7621
JAP60S01	0.5597	1.5985	1.6444	3.7217	0.3637	**0.3293**
REC245PE	0.6686	2.2575	2.2036	2.0675	**0.5877**	0.5988
PC1D	**0.0808**	0.2790	0.0988	0.1692	0.0890	0.0922
M-60	0.5389	2.3731	1.3554	3.4790	0.2402	**0.1983**

A: D. Soto solution [48]; B: Salam solution [103]; C: Villalva solution [46];
D: Sera solution [49].

Table 3.9: RMSE for the six models and PV-modules. Several temperatures [70].

$\frac{1}{N}\sum_{\forall N} RMSE_N$ $0 \leq V \leq V_{oc}$						
Module	A	B	C	D	*Model 1*	*Model 2*
KK280P	12.3243	4.9558	4.7456	9.8631	**2.0624**	2.0624
JAP60S01	3.2788	**2.5414**	3.5234	6.0553	2.7530	2.7530
REC245PE	5.3401	19.2347	21.1252	20.9988	**3.4061**	3.4472
PC1D	2.5819	1.7673	1.8260	2.7153	**0.5664**	0.5664
M-60	47.7531	13.2887	12.8402	16.0188	**2.5192**	2.5198
$\frac{1}{N}\sum_{\forall N} RMSE_N$ $V_{mp} - \Delta V < V < V_{mp} + \Delta V$						
Module	A	B	C	D	*Model 1*	*Model 2*
KK280P	4.0382	3.5711	3.5024	7.4920	**0.9169**	0.9169
JAP60S01	1.3150	1.1779	1.4171	4.2604	**0.5914**	0.5914
REC245PE	1.4154	3.8430	3.6723	3.9007	**1.1597**	1.1768
PC1D	0.6689	0.4025	0.4243	2.7067	**0.1916**	0.1916
M-60	23.7117	3.9325	3.3512	7.4103	**1.4958**	1.4969

A: D. Soto solution [48]; B: Salam solution [103]; C: Villalva solution [46];
D: Sera solution [49].

is possible to see the effect of the linear increment of the resistance due to the conductive part when the temperature increases. Besides, resistance profile at zero light intensity resembles a semi-conductor since the development was based on the conductivity equations of *n-type* and *p-type* semi-conductors. Fig. 3.7 and Fig. 3.8 show the shunt resistances for the PV-modules PC JAP60S01 and MC M-60, respectively, where no effect of the linear increment

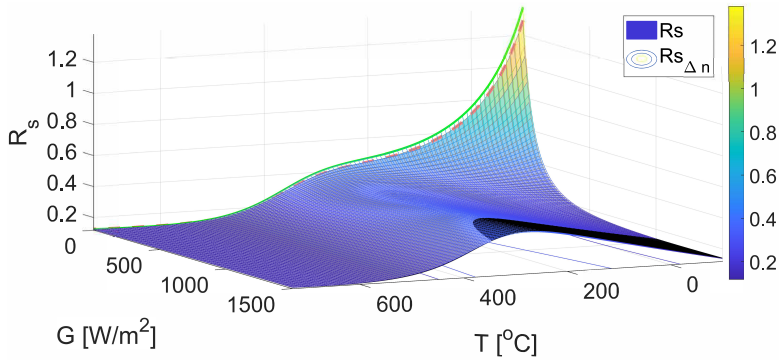is observed since shunt resistances lack conductive part.

Fig. 3.6: Series resistance of the PV-module JAP60S01 in terms of temperature and light intensity. The profiles corresponds to the *Model 1* (R_s) and *Model 2* ($R_{s,\Delta n}$).
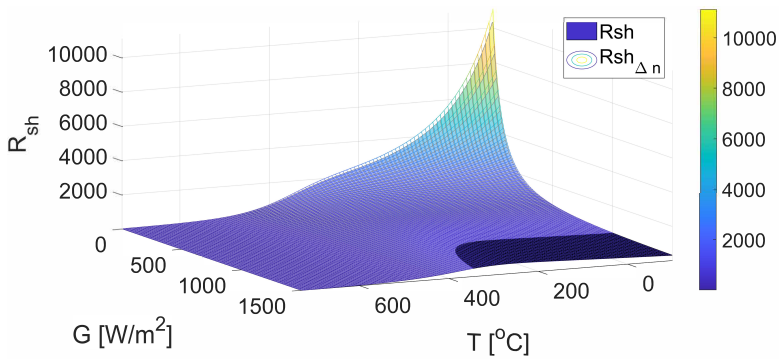
Fig. 3.7: Shunt resistance of the PC PV-module JAP60S01 in terms of temperature and light intensity. The profiles corresponds to the *Model 1* (R_s) and *Model 2* ($R_{s,\Delta n}$).

3.5 Conclusion

This chapter proposed new expressions for the translating equations of the series and shunt resistances of PV cells/modules based on the physical equation for the conductivity of semi-conductors. Besides, the thermal dependent equation for the bandgap energy was updated by adding a new term intending to represent the narrowing effect caused by the doping of extrinsic semi-conductors. The translating equations proposed were applied to a SD five-parameter model to compute the IV-characteristics of five different PV-modules. Besides, the results were compared with four

Fig. 3.8: Shunt resistance of the MC PV-module M-60 in terms of temperature and light intensity. The profiles corresponds to the *Model 1* (R_s) and *Model 2* ($R_{s,\Delta n}$).
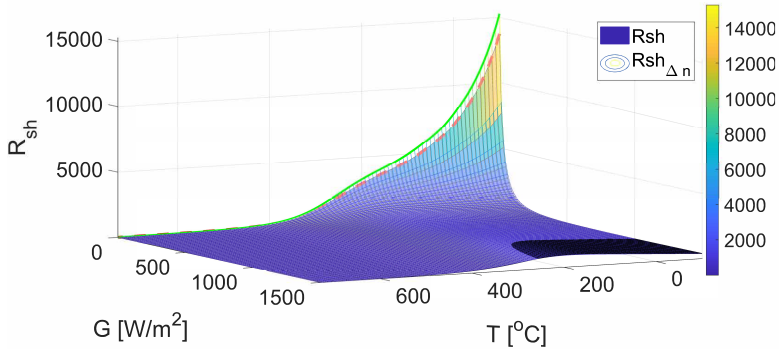
well-known approximations for the translating equations estimation. The results showed a much higher accuracy not only around the MPP, but also throughout the whole range of voltages starting from zero and up to the open-circuit voltage. The metrics used for the assessment were the MAEP for every condition of temperature and irradiance and the average MAEP and RMSE to count for all the different conditions. A disadvantage of the proposed approximations is the use of tuning parameters for constants not provided by the manufacturers on the datasheets and the need of more than one IV-characteristics, accordingly. The reduction in the number of tuning parameters would demand more physical analyses and data that is not usually provided by the manufactures, *e.g.* doping profiles and concentrations. Regarding the tuning parameters, it was observed that the series resistance of the MC technology was dependent totally on the conductive part, different to the PC based modules. Besides, the shunt resistance of the MC module was higher than the corresponding to the PC modules, which suggests that MC technology is better in quality due to a higher fill factor. This also can be observed with the corresponding higher value of α_{ph} (average ratio of the energy gained by the electron from the photon to the total energy contained in the impacting photon) for the MC module. Moreover, the larger narrowing effect of the MC based module suggests that the bandgap of MC modules are more sensible to large doping concentrations.

Chapter 4

Radiation-Induced Degradation Mechanisms of III-V PV-Cells for Space Applications

4.1 Introduction

The space-age started in the 1950s with the use of PV technology to supply energy into space missions [21]. However, two factors are usually taken into account not only for deciding the sort of generation technology, but also the characteristics of the devices. Firstly, the relative distance to the Sun, since it has been shown that the PV-technology is feasible for Jupiter's orbits at longest given that the light intensity is inversely proportional to the distance square [20]. Secondly, the environment, since outer space features extreme conditions such as very low temperatures and deep thermal cycles, micro-meteorites, GCRs, UV radiation, extremely low vacuum, electrostatic fields, lunar dust (for the case of the Moon), space debris (for terrestrial orbits), and highly energetic ion/nuclei particles [21]. Indeed, the degradation due to particle radiation of PV cells is usually considered so severe than it is one of the major concerns of researchers and manufacturers of the space sector. Fig. 4.1 depicts some equivalent fluences of energetic nuclei particles in terrestrial orbits, as well as the distribution of such radiations close and far from the Sun [39].

Even though radiation of highly energetic particles to the PV cells actually produce ionization in the material, the most damaging effect comes from
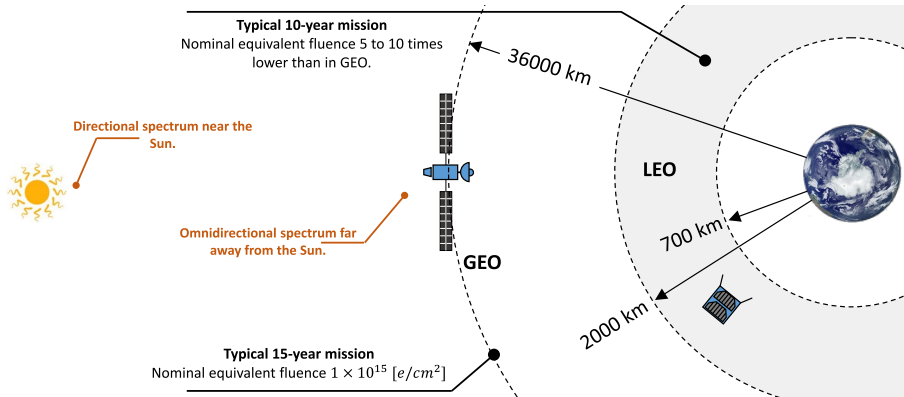
Fig. 4.1: Representation of particle fluences at the low earth orbit (LEO) and geostationary Earth orbit (GEO) [27, 95, 118–120]. The distribution of radiation encountered in some points of the outer space are also depicted. Close to the Sun, the distribution of particle radiation is directional given that particles do not have enough time to scatter each other and create omnidirectionality [35].

the displacement of atoms in the crystal structure of the semiconductors. The impacting of ion/nuclei particles produce mostly three kind of defects. Namely, *vacancies*, which corresponds to empty spaces where originally was located an atom. Then, such an atom is displaced to another position to produce an *interstitial*. Another displacement is characterized by two different atoms that swap positions each other, *anti-sites*, see Fig. 4.2(a) [39]. Depending on the energy level of the defects created, they can act like carrier trap centers producing a virtual removal of carriers, recombination centers due to deep defects shortening the diffusion of carriers, and generating centers producing electrons and/or holes [25, 27, 37, 118], see Fig. 4.2(b). Besides, the degradation produced by ion/nuclei particles depends heavily not only on the type, energy, and striking direction of the particle, but also on the characteristics of the PV cell. For instance, sort of material, the thickness of active wafers, and doping concentration and sign [35, 39, 121], see Fig. 4.3. Also the profile of degradation depends on the distribution of the particle spectrum. For instance, low energetic particles impacting PV cells normal to the surface can get trap inside of the wafers to form a region with the largest damage, usually called *Bragg peak* [35, 58], see Fig. 4.2(c). Several effects caused by the radiation of particles to PV cells are shown in Fig. 4.3. On the other hand, different strategies have been proposed to reduce the effects that radiation of ion/nuclei particles produce in the PV cells, see Fig. 4.4.

However, with the new and more challenging proposed missions for the coming future, many more issues will be faced. In this regard, the review studies are useful tools to identify the challenges to address. Nonetheless, so far, there is not enough review study on the degradation due to particle

radiation of III-V PV cells. The timeline on Fig. 4.5 shows review studies about radiation of III-V/Si based PV cells. This chapter presents a review of different studies committed to the degradation of PV cells, based on Si and materials of the groups III-V, due to particle radiation. Besides, a chronological structure is followed. The studies introduced belongs to the range of time from the 1990s to date.

4.2 Brief Review of Studies From 1950s to 1990s

PV technology has been considered the main option to power space missions since the space age began during the 1950s. The first technology for space application was based on Si wafers while improving up to reach the MJ PV technology during the 1990s [39]. Fig. 4.6 shows a timeline with the main improvements applied to the space PV cells from the 1950s to 1990s.

4.3 Summary of Degradation Studies Regarding PV-Cells Based on Si and III-V Materials (1991-2000)

Much of the effort done regarding the understanding and improving of PV cells for space applications during the decade of the 1990s was towards
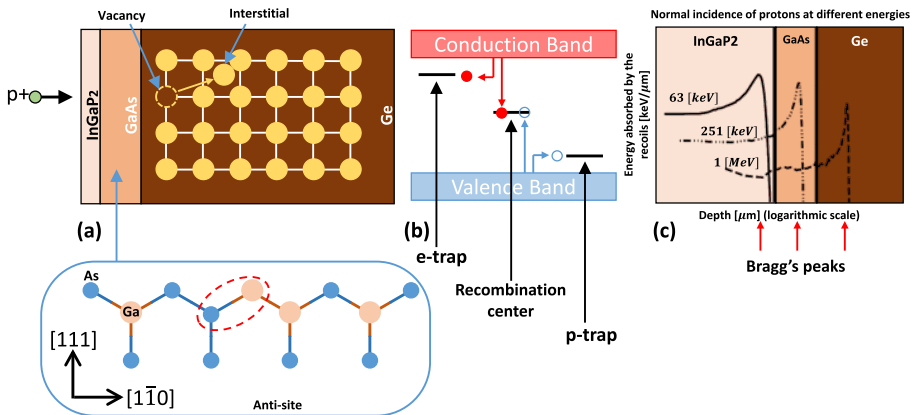
Fig. 4.2: (a) Defects produced by radiation of highly energetic ion/nuclei particles into PV cells. (b) The defects on the bandgap cab be classified into three categories. 1. Trap centers, which produce the carrier removal effect; 2. Generation centers, which can thermally produce carriers; 3. Recombination centers, which recombine minority with majority carriers [25, 37, 118]. (c) Defects distribution profile due to radiation of protons impacting normally a TJ PV cell [35].
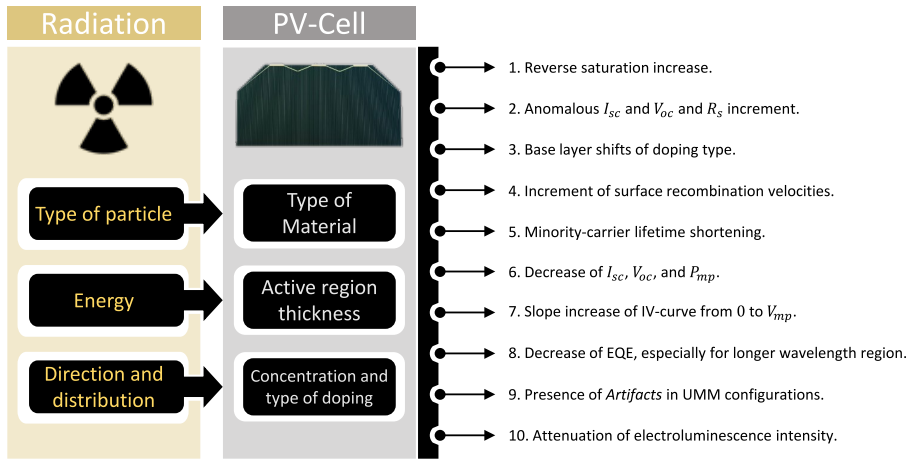
Fig. 4.3: Effects of particle radiation to PV cells. The specific conditions at which each effect appear are described in the following references. 1: [22–24], 2: [25, 26], 3: [23, 25], 4: [27–29], 5: [30], 6: [37], 7: [90, 118], 8: [22, 38, 90], 9: [90], 10: [122].
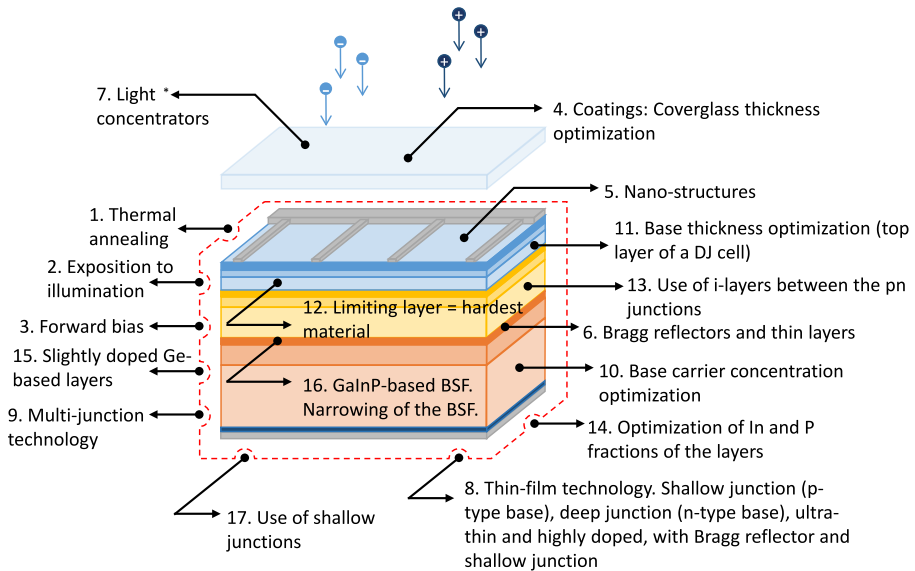
Fig. 4.4: Different strategies proposed on the state-of-the-art for reducing the effects of particle radiation to PV cells. 1: [38], 2: [31], 3: [31], 4: [35, 36], 5: [123], 6: [124–127], 7: [95], 8: [27, 35, 119], 9: [22], 10: [31, 32], 11: [31], 12: [33, 34], 13: [128], 14: [37, 38], 15: [58], 16: [129, 130], 17: [120]. *The application of more than 50 suns to PV cells in space environments is not advised. The reason lies mainly in the high temperatures reached, which can be complicated to control [95].

the Si- and GaAs-based PV cells with architectures SJ and double junction

(DJ) [39]. Table 4.1 provides a brief description of some studies regarding the degradation due to particle radiation of PV cells, based on Si and III-V materials, from the year 1991 to 2000. In addition, Fig. 4.7 shows the feature/element of the PV cells studied by different papers from the years 1991 to 2000.

4.4 Summary of Degradation Studies Regarding PV-Cells Based on Si and III-V Materials (2001-2010)

From 2001 to date, the research efforts regarding the degradation of PV cells due to particle radiation of PV cells was greatly towards the TJ architectures. A list of important publications on this issue are introduced on Table 4.2. Besides, Fig. 4.8 shows the different PV cells discussed on Table 4.2 while the main parts addressed are pointed out [39].

4.5 Summary of Degradation Studies Regarding PV-Cells Based on Si and III-V Materials (2011-2021)

During the period from 2011 to 2021 was observed still a trending on study TJ PV cells with a clear increase of interest on the metamorphic techniques (IMM and UMM) [39]. Besides, the GaAs-based PV cells are still of great importance due to their high efficiency but low radiation resistance. A summary of
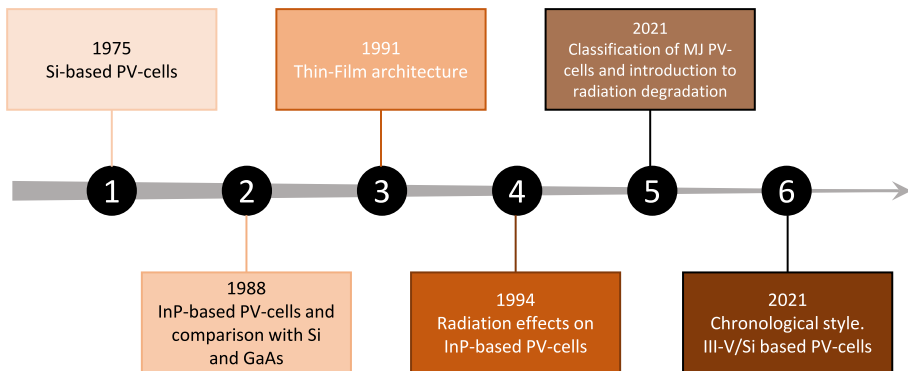
Fig. 4.5: Chronology of review studies focused on the degradation due to particle radiation of PV cells based on Si and III-V materials. 1: [131], 2: [132], 3: [133], 4: [134], 5: [93], 6: [39].
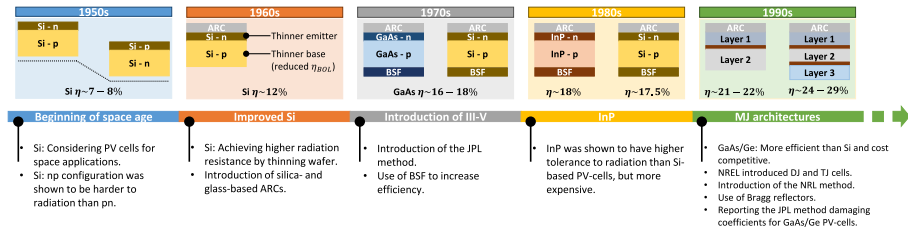
Fig. 4.6: Main improvements to the PV technology for space applications from the 1950s to the 1990s [36, 121, 124, 135–137].

Table 4.1: Study of the degradation of PV cells, based on Si and III-V materials, due to particle radiation (1991-2000) [39].

Year	Brief description	Ref
1991	Damage coefficients PV cells based on GaAs/Ge for estimation of degradation level (experimentally) through the JPL method.	[135]
	Use of Bragg reflectors (BRs). More than fifteen periods of single BRs are enough to produce 100% reflectances. The efficiency increases while the damage due to radiation reduces.	[124]
1996	Study of the degradation of PV cells based on GaAs. Initially, a slight short-circuit current increment while a more drastic reduction of open-circuit voltage can be the effects produced by an increase in temperature. The same trending is observed after the radiation, but smaller magnitudes in both parameters.	[138]
	Mechanism for modeling the anomalous degradation of Si-based PV cells. The degradation is separated in three consecutive parts: gradual degradation, explained by a shortening of diffusion length; increase of short-circuit current, explained by the widening of the charged region; and sudden failure, explained by a carrier concentration reduction.	[26]
1997	displacement damage dose (DDD) into PV cells, based on GaAs, and its dependence on the coverglass thickness.	[36]
1998	Degradation of PV cells made of Si with the DDD approximation. The protons produce defects at deeper energy levels than electrons do.	[25]
	Effects of proton radiation on the SRVs of Si-based PV cells. The SRV increases with fluence of particles.	[28]
1999	Dependency of Si-based PV cells degradation on base carrier concentration. The optimization of the base carrier concentration produces a shorter diffusion length at the beginning of life (BOL).	[32]
	Degradation study of the PV cell InGaP/GaAs and annealing by temperature, illumination, and forward bias. The highest temperature produced the higher annealing effect on the power. The major power recovery was obtained for the biggest temperature applied.	[31]
2000	Proposal of another theoretical mechanism for the degradation of PV cells made of Si. The Shockley-Read-Hall (SRH) recombination theory and the electroneutrality condition are the bases of the proposal.	[23]

studies published from 2011 to 2021 regarding the degradation of PV cells based on Si and III-V materials due to particle radiation is presented in

4.5. Summary of Degradation Studies Regarding PV-Cells Based on Si and III-V Materials (2011-2021)

Table 4.3.

Table 4.3: Study of the degradation of PV cells based on Si and III-V materials due to particle radiation (2011-2021) [39].

| Year	Brief description	Ref
2011	Thinning the middle layer of a TJ PV cell and incorporating a BR to improve the radiation resistance of the whole cell. The best efficiency improvement was achieved including a double BR (up to 2%). Unfortunately, the GaAs-based layer is still the limiting sub-cell.	[125]
2012	Splitting a light beam with a double BR (15 periods each). The range spectrum of light from 900 to 1050 [nm] is forwarded to an external PV cell made of Si. The efficiency was increased up to 3.5%.	[145]
2014	Change of the bottom layer material, from Ge or GaAs to InGaAs, of an IMM TJ PV cell. The efficiency improves up to 37.9%. The cell is 15 times lighter than a Ge-based substrate architecture. The radiation hardness of the middle and bottom layers was improved by growing *i*-layers between the *pn* junctions.	[128]
	Combination of a distributed 16-period BR and the tunnel diode (TD) in the top-middle layer junction to eliminate parasitic absorption of reflected light. The efficiency increased more than 10% respect to a TJ PV cell without the BR.	[146]
2018	Comparison of radiation resistance of two similar TJ PV cells (LM and UMM) using the NRL method. The top layer BOL of the UMM-based cell was lower than the corresponding to the LM, but the radiation hardness was higher.	[37]
	Study of radiation of TJ PV cells at low-intensity low-temperature (LILT). The bottom layer was the current limiting sub-cell at the lowest temperatures (< 200 [K]). A reduction of the bottom cell effective area was concluded rather than recombination of carriers since there was not observed any change of the reverse saturation current.	[24]
	It is proposed that photo-generated current of GaAs-based PV cells depends on the voltage after radiation. The dependence would come from the depletion area shortening with a forward bias, where the charged region would broad with the radiation. This would be responsible of the sloped IV-curve, which resembles a shunt resistance reduction.	[118]
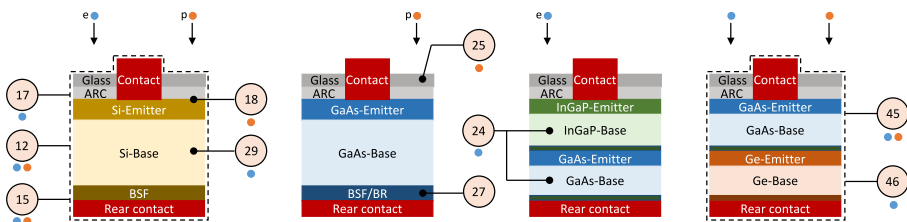
Fig. 4.7: Different PV cells studied from the year 1991 to 2000. Each part of the cell pointed is the element studied and/or modified and/or optimized in terms of radiation hardness. The corresponding references are 12: [25], 15: [23], 17: [26], 18: [28], 24: [31], 25: [36], 27: [124], 29: [32], 45: [135], 46: [138].

2019	Comparison of the degradation of UMM and LM PV cells due to radiation of low energetic protons. The UMM PV cell's power was reported to be slightly more degraded. The dark saturation current increases while the shunt resistance reduces, according to the authors.	[90]
	Degradation of PV cells based on GaAs due to particle radiation and its dependence on geometry and doping concentration. Two thin film (TF) PV cells architectures are reported with a power higher than 90% at the end of life (EOL). 1 Shallow junction and p-type base. 2 Deep-junction and n-type base.	[119]
	Application of different configurations of multiple BRs to LM and metamorphic (MM) PV cells. The highest efficiency of the LM PV cell was achieved with a configuration of three groups, 16 periods each. For the case of MM PV cell, it is proposed to use the BR as buffer also.	[147]
	Application of a 20 period BR to a GaAs-based PV cell with the middle layer thinned by half. An absolute efficiency increase of 0.24% is claimed.	[126]
2020	Effect of the junction depth and layer thickness on the degradation of GaAs-based PV cells. The best option reported is TF PV cells with back reflector and shallow junction.	[27]
	Comparison of GaAs-based with InP-based (at different fractions) PV cells. The higher the fraction of InP in the cells, the better the recovery after annealing procedure.	[38]
	Application of EL to assess a TJ PV cell in terms of degradation of the open-circuit voltage in individual layers. The GaAs-based sub-cell showed the largest damage.	[122]
	Degradation study of a DJ PV cell with LM structure using the NRL method. The top-layer based on GaAs was the current limiting layer.	[22]
	Degradation of TJ PV cells. Reverse saturation current increases due to radiation of highly energetic protons while the open-circuit voltage degrades, accordingly. The collision density of protons is higher than the corresponding to electrons, accordingly, the protons induce a larger degradation.	[148]
	Degradation of more than 300 Ge wafers. The doping concentration was reduced while a "mirror" layer was included to improve the absorption of the long-wavelength spectrum region. Lowly doped and passivated Ge-based PV-layers are suggested to be good candidates for space applications.	[58]
	Increase of radiation resistance of TJ PV cells by using the middle layer back surface field (BSF) based on GaInP. No significant difference at the BOL was reported.	[129]
	Study of radiation damage to a four junction (FJ) PV cell in the geosynchronous Earth orbit (GSO) and LEO. The largest damage in the GSO is due to the trapped electrons, followed by solar protons and GCRs. The largest damage in the LEO is due to the solar protons, followed by trapped protons and electrons.	[34]
2021	Study of defects created by 1 [MeV] protons in GaAs PV cells. The electron traps are the most important. Two deep electron traps and one hole trap are the most damaging (near to the Fermi-level). The radiation hardness is increased by thinning the BSF layer.	[130]
	Comparison of experimental and software SRIM results. SRIM overestimates the range of protons across InGP-based PV cells while it is very exact for the case of GaAs-based PV cells. The reason lies on the difference of electronic bonding distribution in both semiconductors.	[149]

4.5. Summary of Degradation Studies Regarding PV-Cells Based on Si and III-V Materials (2011-2021)

Radiation study of different architectures of GaAs-based PV cells (TF-based, substrate-based, and shallow and deep junctions). Two architectures are suggested for space applications: substrate- and TF-based with shallow junctions.	[120]

Additionally, Fig. 4.9 shows some of the PV cells architectures studied on the papers described here. The elements studied and/or modified and/or optimized of each cell are pointed out and the reference provided for more details. Table 4.4 provides important remarks identified during the review process. Besides, Fig. 4.10 provides some important points considered by the authors on the development of their experiments and simulations.

Table 4.4: Important remarks identified by different studies regarding the degradation of PV cells based on Si and III-V materials due to particle radiation [39].

Structure of Cell and Remarks	Refs.
Si	
A better degradation model can be achieved by considering the deepest traps in the mobility expression.	[25]
Deeper defects are produced by protons than electrons.	[25]
The higher the proton fluence, the larger the SRV.	[28]
Considering a threshold on the fluence. Towards lower values, the maximum efficiency is located in lower values of concentration of carriers in the base. Towards higher values, the maximum efficiency is located in higher values of concentration of carriers in the base.	[32]
A theoretical formulation explains that a base thickness in the range of the diffusion length allows the anomalous degradation.	[23]
An adjusted NIEL improves the estimation of the degradation level computed by the NRL method.	[57]
GaAs	
A radiation of unidirectional and mono-energetic protons having energies between 1 and 10 [MeV] upon bare PV cells resembles properly the space conditions.	[36]
From the largest to the smallest degradation caused by nuclei particles: protons, neutrons, and electrons.	[143]
The shallow junction architecture is more effective to keep a higher efficiency after radiation in comparison to the deep-junction architecture.	[27, 120]
The protons radiation produce mainly electron traps.	[130]
A higher remaining efficiency is achieved by a thinner BSF.	[130]
The voltage dependence of the photo-generated current produce a steeper slope of the IV-curves.	[118, 120]
PV cells can achieve EOL power higher than 90% with thin and highly doped configurations.	[119]
An increase of the radiation hardness can be achieved using multiple BRs while thinning the cell.	[124]
The optical properties of BRs based on 20 periods of $AlAs/Al_{0.1}Ga_{0.9}As$ are highly resistance to electron fluences between 2×10^{14} and 1×10^{15} $[e/cm^2]$ having energy of 1 [MeV].	[126]
GaInP	
A higher resistance to radiative environments (electrons) than PV cells base on GaAs and Silicon, which is the weakest.	[140]
GaAs, GaInP	

The software package SRIM is inaccurate to model protons range in PV cells based on GaInP given the high directionality of its electronic cloud.	[149]
The changes in optical parameters, due to radiation, increase the phonon intensity observed.	[149]
GaInP/GaAs/Ge	
The middle layer is the weakest against electrons and protons radiation.	[29, 33, 59, 122, 141]
The emitter degradation and SRV increase of the interface top-middle layer are the main reasons of degradation of the top layer.	[59]
A proton range around the pn junction produces the largest open-circuit voltage relative damage coefficient.	[141]
The optical losses in the upper tunnel diode is reduced by combining the diode itself with a BR.	[146]
InGaP$_2$/GaAs/Ge	
A 3 mils SiO$_2$ coverglass[1] can produce a uniform distribution of the damage due to bombarding of omnidirectional spectrum of protons having energies between 0.03 and 5 [MeV].	[35]
Radiation of protons having energies between 1 and 10 [MeV] are more suitable for ground-based experiments.	[35]
Due to the difference in damage distribution, radiation of PV cells with mono-energetic, normally incident, and low energetic protons stopping inside of the cell is not suitable for ground-based tests.	[35]
Highly energetic protons able to traverse the active layers of the PV cell are suitable to ground-based experiments.	[35]
GaAs is the weakest layer against radiation of protons.	[35]
(LM) Ga$_{0.51}$In$_{0.49}$P/GaAs/Ge	
The bottom layer becomes more degraded while temperature reduces up to be the layer limiting the current.	[24]
The reverse saturation current is not observed increasing at the EOL at very low temperatures.	[24]
The Ge-based layer is the most recovered after annealing.	[24]
(LM) GaInP/GaAs/Ge, (UMM) InGaP/InGaAs/Ge	
The degradation of power due to protons having energies of 50 keV and 150 keV has different magnitudes depending on the PV cell type. The UMM is majorly degraded by the former energy while the LM by the latter energy.	[90]
The main effect of low energetic protons is the shunt-resistance reduction.	[90]
(UMM) Ga$_{0.43}$In$_{0.57}$P/Ga$_{0.92}$In$_{0.08}$As/Ge, (LM)Ga$_{0.51}$In$_{0.49}$P/Ga$_{0.99}$In$_{0.01}$As/Ge	
The LM and UMM PV cells get degraded similarly due to protons radiation.	[37]
(MM) Ga$_{0.44}$In$_{0.56}$P/Ga$_{0.92}$In$_{0.08}$As/Ge	
The combination of a multi-BR with the buffer layer improves the PV cell efficiency and radiation hardness (light splitting).	[147]
GaInP$_2$/InGaAs/Ge	
The shunt-resistance is decreased by the radiation of protons.	[148]
The deep defects concentration is not increased considerably by the radiation of highly energetic protons.	[148]
A non-linear increment of traps in the interfaces is observed with the protons bombarding.	[148]
(LM) GaInP/GaInAs/Ge	
The radiation hardness is improved by changing the middle-layer BSF from AlGaAs to Ga$_{0.502}$In$_{0.498}$P.	[129]
The electrons radiation degrades mostly the GaAs-based middle layer.	[129]

The use of BRs allows to use external PV cells (light splitting) while the main cell is thinned, increasing the efficiency and radiation hardness, respectively.	[145]
GaInP/Ga$_{0.99}$In$_{0.01}$As/Ge	
The efficiency is increased by using double BR while optimizing the layers thickness. Even though a higher radiation hardness, a lower BOL efficiency should be expected.	[144]
(IMM) InGaP/GaAs/InGaAs	
The inclusion of i-layers in the middle and bottom layers, between the pn junctions, improves the radiation hardness.	[128]
(LM) GaInAsP/InP	
A better annealing can be expected in cells with higher InP fraction.	[38]
The GaAs-based cell shows a better performance post-radiation, but lower performance after annealing.	[38]
Ge	
The doping concentration reduction increases the EOL diffusion length.	[58]
The SRV is increased with the particle radiation.	[58]
InGaP/GaAs	
The GaAs layer is the weakest against electron radiation.	[31]
The incorporation of light and forward current to the annealing treatment improves the annealing.	[31]
GaInP/GaAs/Ga$_{0.7}$In$_{0.3}$As/Ga$_{0.42}$In$_{0.58}$As	
The third layer is the weakest against electrons radiation.	[34]
Optimization of the thickness of the layers can enhance the radiation hardness.	[34]
Any	
The outer space radiation conditions are resembled by particles having energies between 1 and 8 [MeV] upon bare cells.	[121]

Note 1: Typically used for GSO orbits (3 to 6 [mils]). A thickness between 6 and 30 [mils] are usually utilized in the highly elliptical orbits (HEOs).

4.6 Future Challenges

Some important challenges that still remain regarding the study of degradation due to particle radiation of PV cells based on Si and III-V materials, were identified through the development of this review study. These challenges should be addressed and overcome for a deployment of space systems, powered by solar energy, with a high level of RRROS. The challenges are listed in the following [39].

1. The GaAs is among one of the most commonly used compounds to build space PV cells given its relative low cost and efficiency. However, the low resistance again radiation of energetic ion/nuclei particles has been widely demonstrated and studied. In fact, the application of BRs has been proposed, which allow to thin the GaAs-based sub-cells while increasing the radiation hardness of the whole PV cell. Even though this technique is able to increase the efficiency and radiation resistance after a level of radiation fluence, still some studies emphasize the need of more research in this direction. It is regularly highlighted that the

Table 4.2: Study of the degradation of PV cells based on Si and III-V materials due to particle radiation (2001-2010) [39].

Year	Brief description	Ref
2001	The theoretical model of the degradation of Si-based PV cells with the recombination theory SRH and the condition of electroneutrality as the basis for the model, was re-considered while locating the traps near to the Fermi-level.	[139]
	Comparison of the JPL and NRL methods. The NRL method needs a reduced number of experimental profiles in comparison to the JPL method. However, the NRL method is not suitable to estimate degradation of thick PV cells, such as Si-based cells.	[121]
	Study of the degradation of PV cells (Silicon, GaAs, and GaInP) due to particle radiation.	[140]
2002	Use of the electroluminescence (EL) technique for computing the degradation of individual layers on a TJ PV cell. It is recommended to build the current-limiting layer with the least sensitive material to the radiation of particles.	[33]
2003	The inaccuracy of NRL method to compute the degradation of PV cells, based on Si, due to particle radiation is overcome by using an adjusted non-ionizing energy loss (NIEL).	[57]
	Use of a light beam as bias to measure the spectral response (SR) of individual layers of a TJ PV cell. The greatest damage to the cell was identified where the particles stopped.	[141]
2006	Analysis of a GaAs-based PV cell. The introduction rate of recombination centers was proposed to be proportional to the NIEL.	[142]
	Study of the effects of an omnidirectional spectrum of low energetic particles upon TJ PV cells. Besides, influence of coverglass thickness on the degradation of PV cells due to particle radiation. The most severe damage was shown to be when particles stuck at the GaAs layer (middle). A coverglass made of SiO_2 with thickness 10 $[\mu m]$ showed a good performance to keep the damage profile uniform across the cell.	[35]
2008	Study of the degradation of TJ PV cells due to low energetic protons. The higher the fluence, the higher the degradation. On the other hand, a higher degradation is observed by decreasing the particles' energy.	[59]
2009	A method based on PC1D to estimate the carrier removal rate (R_c) and degradation coefficient of diffusion length (K_L) is introduced. The R_c is linearly proportional to the NIEL while K_L is either linearly or quadratically proportional to the NIEL, depending on the particle type.	[29]
	It is shown that the method introduced in [29] is unable to fit experimental results for diffusion length shorter than 40 $[nm]$.	[30]
2010	The software *SCREAM* was introduced, which is based on the NRL method and still inaccurate for the degradation modeling of PV cells based on Si. A relationship between the NRL and JPL methods is shown.	[143]
	Single and double BRs are proposed for TJ PV cells while the top and middle layers are optimized. The middle layer thickness is optimized to improve radiation tolerance and the top layer for current matching. The double BR improves the efficiency up to 5% and the radiation resistance.	[144]

GaAs-based layer is the weakest again radiation of energetic particles and the most responsible for the cell degradation.

Fig. 4.8: Different PV cells studied from the year 2001 to 2010. Each part of the cell pointed is the element studied and/or modified and/or optimized in terms of radiation hardness. The corresponding references are 8: [35], 9: [121], 11: [59], 19: [29], 20: [30], 30: [33], 47: [139], 48: [140], 49: [57], 50: [141], 51: [142], 52: [144].
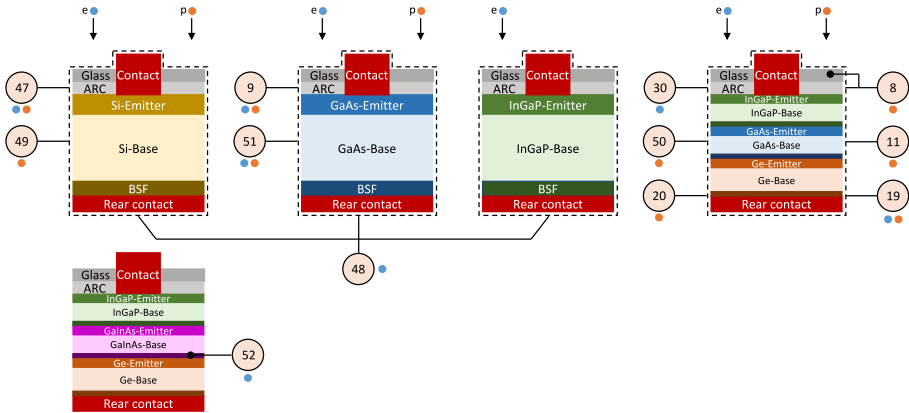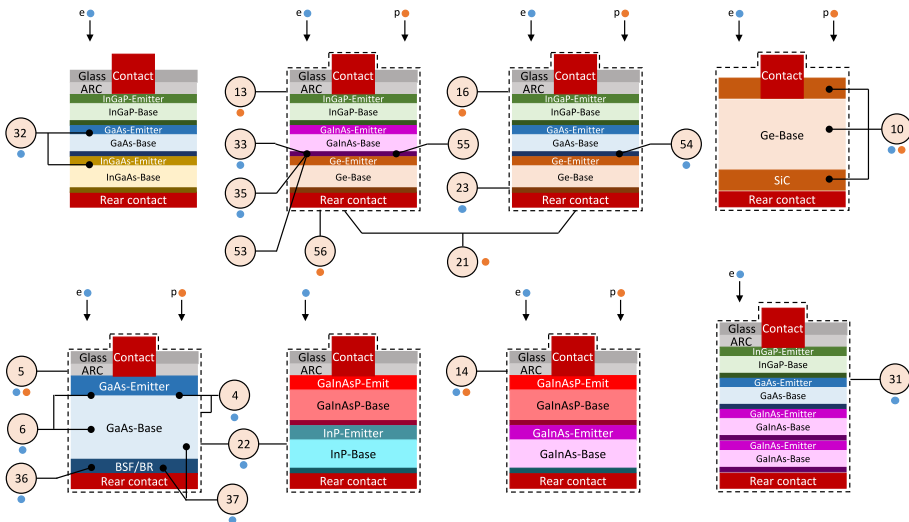

Fig. 4.9: Different PV cells studied from the year 2011 to 2020. Each part of the cell pointed is the element studied and/or modified and/or optimized in terms of radiation hardness. The corresponding references are 7: [120], 8: [35], 9: [121], 12: [25], 15: [23], 16: [24], 18: [28], 23: [122], 24: [31], 25: [36], 33: [129], 34: [130], 35: [125], 37: [127], 38: [94], 39: [150], 54: [146], 55: [147], 56: [148], 57: [149].

2. The high directionality of the electronic cloud around the atoms comprising compounds like the GaInP, which is one of the most commonly used for space PV cells, is not properly considered yet for the study of degradation due to particle radiation. It has been

demonstrated that package software like SRIM are inaccurate and overestimates the range of the particles inside of the semi-conductor. Therefore, to be able of modeling properly and designing better space PV cells, more investigation in this regard is required.

3. Several studies have suggested degradation of the joints between the layers due to the radiation of nuclei particles. Nonetheless, the need for an accurate model with a basis on physics is still present. Therefore, more experimentation and physical analysis is needed in this respect.

4. The effect of extreme conditions, such as high and very low temperatures, as well as high and low sunlight intensities upon the degradation due to particle radiation of space PV cells is still barely studied. Nonetheless, the future space missions will face several of such hazardous conditions. Therefore, the experimentation and physical modeling of such environments upon the PV cells based on Si and III-V
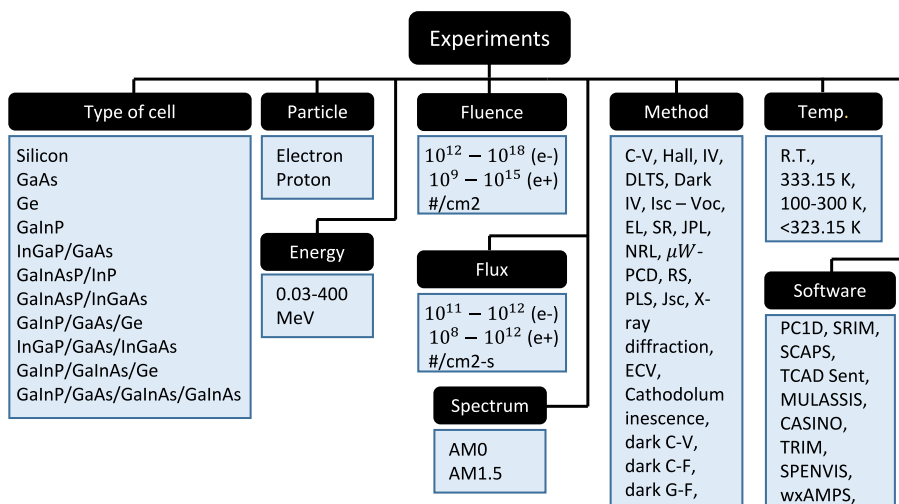

Fig. 4.10: Important features considered by different authors regarding experimentation. The values of energy, fluence, and flux covers the ranges considered by different studies. The spectrum AM0 is usually considered for terrestrial and lunar orbits, while AM1.5 for spectrum on Earth.   The experimental methods are defined as C-V: capacitance-voltage, Hall: Hall effect measurements, IV: current-voltage measurements, DLTS: deep-level transient spectroscopy, Dark IV: current-voltage measurements at darkness, $I_{sc} - V_{oc}$: short-circuit current vs open-circuit voltage, EL: electroluminescence, SR: spectral response, JPL: JPL method, NRL: NRL method, μW-PCD: microwave photo-conductance decay, RS: Raman spectroscopy, PLS: photo-luminescence spectroscopy, J_{sc}: short-circuit current density, ECV: electrochemical capacitance-voltage, Dark C-V: capacitance-voltage measurements at darkness, Dark C-F: capacitance-frequency measurements at darkness, Dark G-F: conductance-frequency measurements at darkness.

materials is of paramount importance to achieve high levels of RRROS.

5. Different features of the space PV cells change after a radiation of energetic particles, thereby indicating the level of damage of the cell. The decrease of the IV-curve's slope from the short-circuit to the MPP condition has been widely observed on radiated PV cells. However, more than one explanation has been provided to this effect. The reduction of the shunt resistance and a dependence of the photo-generated current on the voltage after radiation are two of the most commonly discussed origins for this effect. Therefore, more experimental and physical modeling studies are required in this regard to clarify the actual origin of such an effect and improve the PV cell designs and models.

4.7 Conclusion

During the last decades an increasingly interest in the MJ PV technology for space applications has been observed. One major reason is due to the high efficiency and radiation resistance. In this regard, several effects on the PV cells based on Si and III-V materials have been identified and accordingly different techniques have been proposed to reduce their magnitude. However, still several challenges have to be overcome to increase the PV systems lifetime with a high efficiency. This chapter has been dedicated to summarizing different studies regarding the degradation due to particle radiation of PV cells based on Si and III-V materials. Besides, some of the main remaining challenges are introduced.

Chapter 5

Characterization of III-V MJ PV-Cells

5.1 Introduction

The degradation mechanisms of PV cells, based on Si and III-V materials, due to particle radiation were thoroughly discussed in Chapter 4. Besides, several effects that PV cells present after radiation of nuclei particles were introduced with a review of important scientific publications in a chronological style. In this sense, this chapter introduces and briefly discusses the experimental data obtained from the characterization of 39 $Ga_{0.5}In_{0.5}P/Ga_{0.99}In_{0.01}As/Ge$ PV cells. A further analysis of the results along with a proposed mechanism of the degradation of III-V MJ PV cells is under progress and will not be presented here.

The samples are comprised of 2×2 $[cm^2]$ bare[1] PV cells, which were divided into two batches with three groups each. The first 20 cells correspond to the first batch, which were previously radiated by protons having 1 [MeV] of energy, and impacting normally to the samples. The groups of the first batch correspond to fluences of 5×10^{10}, 3×10^{12}, and 1×10^{13} $[p/cm^2]$. The second batch is comprised of 19 cells, which were previously radiated by 2 [MeV] protons impacting normally to the surface of the samples. The corresponding groups are comprised of three different fluences, 1×10^{11}, 1×10^{12}, and 5×10^{12} $[p/cm^2]$.

The experiments involved were the measurement of illuminated IV-curves, dark IV-curves, and EQE curves at RT, and IV-curves at very low temperatures. Besides, a brief description of the setups utilized in these experiments is introduced. This outcome is a product of a research stay
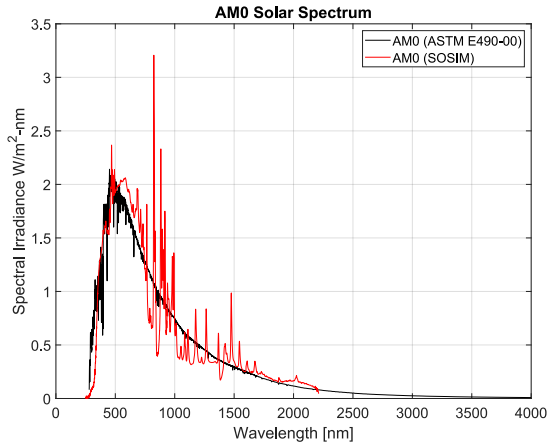
---

[1]no-shielding.

Fig. 5.1: Comparison between the solar spectrum AM0 provided by National Renewable Energy Laboratory (NREL) and the spectrum generated by the SOSIM [151].

in the company *AIRBUS-Defence and Space*, Munich, Germany, during the period from August to October 2021 and under the supervision of Dr. Claus Zimmermann.

5.2 Measurement of Illuminated IV-Curves

The measurements were performed at 25 $[°C]$ by using a square beam SOSIM with two halogen and one xenon lamps and calibrated with CASOLBA2005 standards. Besides, the data acquisition was done with a Keithley 2430, 3A, source-meter. The spectrum produced by the SOSIM can be observed at Fig. 5.1.

The illuminated IV-curves show a higher degradation with the increase of the protons fluence in both energies, see Fig. 5.2. Thus, a reduction of the open-circuit voltage and short-circuit current with the increase of protons fluence is observed. Furthermore, in both energies, a becoming steeper slope of the IV-curve from the open-circuit to the MPP condition with the particle fluence is observed. This effect is more notorious at the lowest 1 $[MeV]$ energy. Nowadays, two different explanations have been provided to this phenomenon. Some studies have claimed that the becoming steeper slope of the IV-curve is result of the PV cell's shunt resistance decrement, which in turn represents the leakage current due to the presence of defects in the semiconductor [90,148]. On the other hand, other works have reported that this phenomenon is due to the photo-generated current dependency on the voltage after the radiation [118,120].
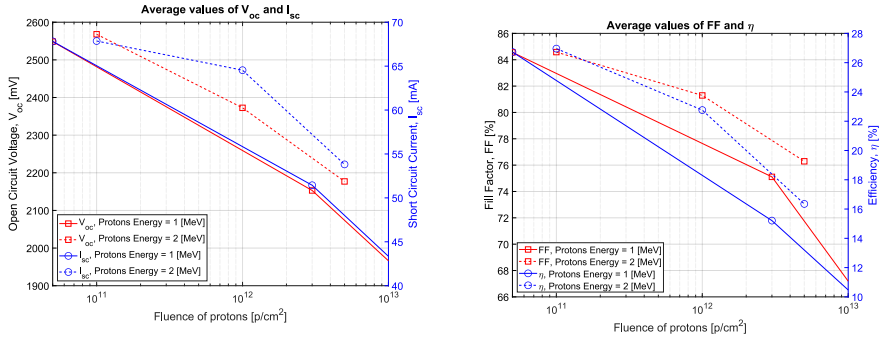
Fig. 5.3a shows the open-circuit voltage and short-circuit current at
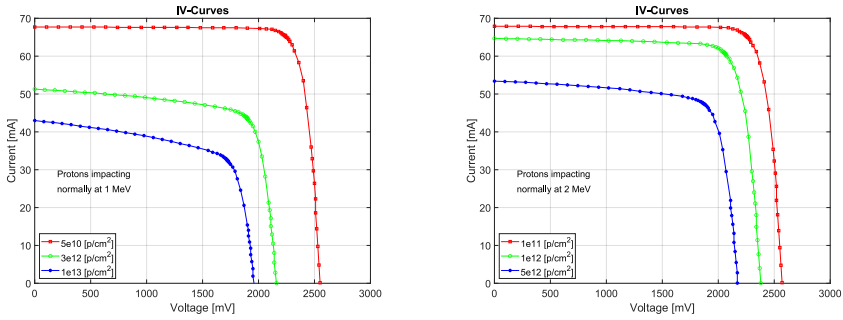
(a) Radiation with normal incident protons at 1 [*MeV*]. **(b)** Radiation with normal incident protons at 2 [*MeV*].

Fig. 5.2: IV-curves of similar 2×2 [cm^2] PV cells at 1 $AM0$ and 25 [$°C$].

(a) Open-circuit voltage and short-circuit current degradation.

(b) Fill factor and efficiency degradation.

Fig. 5.3: PV cell degradation due to radiation of protons having 1 and 2 [*MeV*] of energy.

different levels of proton fluence and for both energies. A higher degradation not only on the open-circuit voltage, but also the short-circuit current, is observed for the lowest proton's energy of 1 [*MeV*]. Moreover, Fig. 5.3b shows the fill factor and efficiency for different fluences and both levels of energy. Even though, both proton's energies reduces the PV cell efficiency and fill factor with a fluence increase, once again the protons having 1 [*MeV*] of energy degrades them more severely. The degradation of the maximum power is also compared for both energies in Fig. 5.4. Likewise, the power degradation is larger when the cells are radiated with protons having 1 [*MeV*] of energy than having 2 [*MeV*].
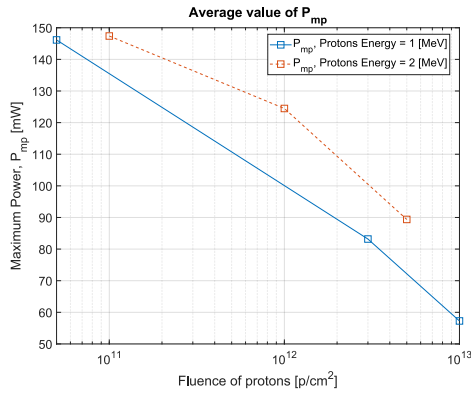
Fig. 5.4: Maximum power at different fluences and for both proton's energies.

5.3   Measurement of Dark IV-Curves

The measuring of dark IV-curves at 25 $[^\circ C]$ was carried out using a Keithley 2430, 3A, source-meter. Fig. 5.5a and Fig. 5.5b show the forward dark IV-curves of six cells radiated by different proton fluences at 1 and 2 $[MeV]$ of energy, respectively. From these dark IV-curves, a higher degradation with the increase of the fluence is observed, regardless the energy of the particles. The increase of the current with the fluence indicates a larger number of defects created by the radiation of particles. Besides, the higher current produced by the radiation of 1 $[MeV]$ protons confirmed again that protons with this energy induce a higher degradation to the PV cells than protons
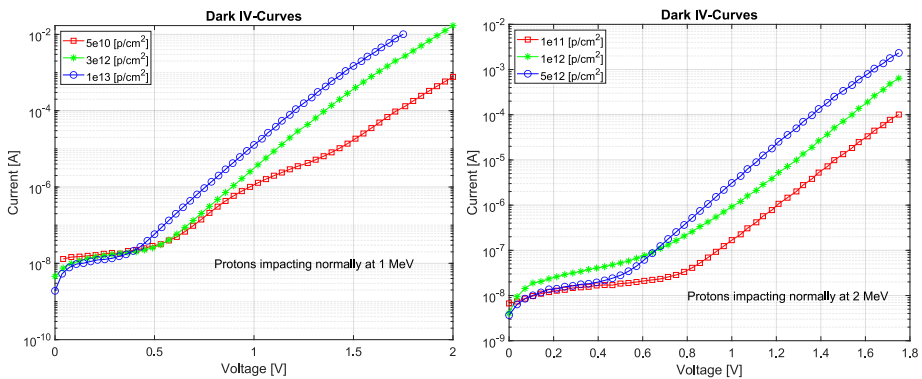
(a) Radiation with normal incident protons at 1 $[MeV]$. **(b)** Radiation with normal incident protons at 2 $[MeV]$.

Fig. 5.5: Dark IV-curves of 2×2 $[cm^2]$ PV cells at 25 $[^\circ C]$.

Fig. 5.6: EQE-curves of a TJ PV cell before and after removal of *artifacts*.

having 2 $[MeV]$ of energy.

5.4   Measurement of EQE-Curves

The EQE curves were measured using a SpeQuest Quantum Efficiency of ReRa Solutions, which contains halogen, xenon, and LED lamps and calibrated by a reference PV cell made of Silicon $(250 - 900 \, [nm])$ and another of Germanium $(900 - 1900 \, [nm])$. Be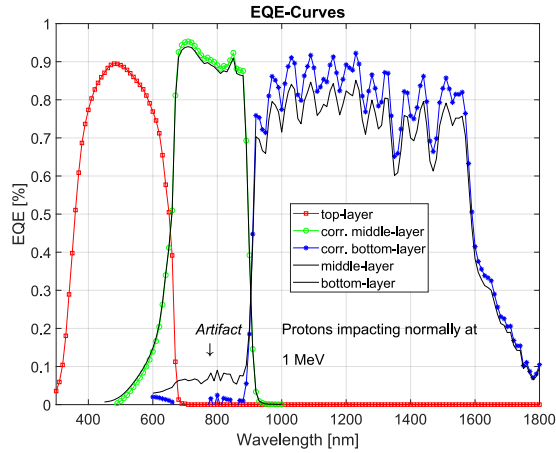sides, it features a monochromator able to disperse the light into monochromatic bands of 10 $[nm]$ bandwith from 250 to 2000 $[nm]$. The setup applies bias light to measure the EQE of individual layers of MJ PV cells. Fig. 5.6 shows the EQE measurement of a sample, which was radiated by 1 $[MeV]$ protons at a fluence of $5 \times 10^{10} \, [p/cm^2]$. The *artifacts* created by the radiation of protons were removed with the algorithm introduced by [152].

Fig. 5.7a shows the EQE-curves of three similar PV cells, but radiated by different fluence of protons at 1 $[MeV]$ of energy. From such a figure, it is observed that the higher the fluence, the larger the damage represented by a lower EQE in each layer. Besides, it should be noticed that the middle-layer, which is made of $Ga_{0.99}In_{0.01}As$, is the most damaged layer, such as it has been claimed by some studies [29, 35, 59]. Furthermore, it can be observed in each individual layer that its corresponding EQE curve is degraded more in the longer wavelength region. The reason behind this lays on the fact that longer wavelength photons are absorbed deeper in the layers. Then, the higher the absorbed photon wavelength, the larger the distance that a generated carrier has to travel to reach the charged region, increasing thereby
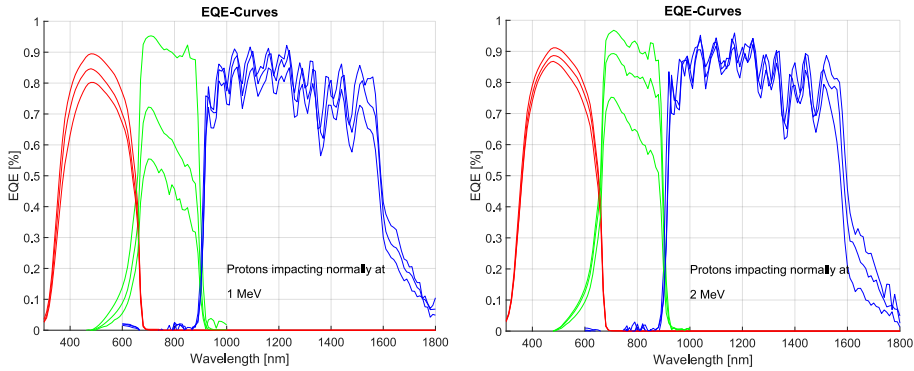
(a) Curves for three different fluences: $5 \times 10^{10}, 3 \times 10^{12}, 1 \times 10^{13}$ $[p/cm^2]$. Radiation with normal incident protons at 1 $[MeV]$.

(b) Curves for three different fluences: $1 \times 10^{11}, 1 \times 10^{12}, 5 \times 10^{12}$ $[p/cm^2]$. Radiation with normal incident protons at 2 $[MeV]$.

Fig. 5.7: EQE-curves of 2×2 $[cm^2]$ PV cells at RT. The color of the curves indicates the EQE of a specific layer: red →top-layer, green →middle-layer, blue →bottom-layer.

the probability of the carrier to be recombined. On the other hand, Fig. 5.7b shows similar EQE curves, but corresponding to a radiation of protons having energy of 2 $[MeV]$. Comparing both figures in Fig. 5.7, once again is observed a higher degradation of the samples radiated by protons with 1 $[MeV]$ of energy.

5.5 Measurement of Deep-Temperature IV-Curves

The measurement of deep-temperature IV-curves was carried out in the same square beam SOSIM used to measured the illuminated IV-curves at 25 $[°C]$. Besides, the SOSIM was calibrated with CASOLBA2005 standards. Additionally, a high vacuum chamber with a cooling system was utilized intending to resemble outer space conditions. In general terms, the setup features:

1. Two vacuum pumps. The primary vacuum pump is started up to reach a stable vacuum at a medium level. Then, the secondary or high vacuum pump is started to get a high vacuum level.

2. A nitrogen container with a pipe connected from the container to a nitrogen pump and passing through the cooling plate, which is allocated inside of the vacuum chamber.

3. Vacuum chamber with a cooling plate. The PV cells are attached on the top of the cooling plate with RTV silicone adhesive sealant. This allows

to fix firmly the samples to the cooling plate while having an effective thermal contact.

4. Low temperature sensors, which are allocated between the cooling plate and the RTV, just under the PV cells.

5. Selector of samples. This relay-based device allows to select a specific sample to be measured. The electrical signal are sent to the SOSIM while the thermal sensing to an additional control.

6. Thermal control. External control of the cooling plate temperature. The input signal belongs to the temperature measured from the selected sample, the output control signal is to switch on/off either a heater or the nitrogen pump, and the reference is given manually by the user.

7. Vacuum level monitoring. Display to show the level of the vacuum in the two stages.

8. Connectors to the samples. The positive is common for all the PV cells while the negative is provided individually to each sample. The sensing is performed individually to each cell.

9. Base with elevation system to adjust the height of the PV standards to setup the SOSIM. The standards are fixed by means of vacuum holes and the temperature is regulated by an additional thermal control.

10. Data acquisition system with a Keithley 2430, 3A, source-meter.

The setup was assembled twice with twelve samples maximum in each iteration due to available space issues. In total, four PV cells corresponding to each fluence of protons was measured at low temperatures[2]. The experiment temperatures were 25, -100, -163.15, -180, and again 25 $[°C]$ at each iteration. The selection of the two lowest temperatures are representative of the maximum levels found near to the *Shackleton crater* on the south pole of the Moon, which ranges from -193.15 to -163.15 $[°C]$ [69,71]. However, the minimum temperature was limited by the boiling point of the nitrogen (-195.8 $[°C]$) and the thermal looses of the system. On the other hand, the -100 $[°C]$ temperature was measured to have more useful data on the PV cell behavior at low temperatures. The PV cells were measured at 25 $[°C]$ at the beginning and end of the experiments to verify that the same values are obtained and nothing on the system was changed during the measurements. Otherwise, the experiment should be repeated.

The IV-curves were performed at the same light intensity and spectrum 1 *AM*0. Fig. 5.8 shows the IV-curves corresponding to the lowest and highest fluence of protons having 1 and 2 $[MeV]$ of energy. In Fig. 5.8, all the subplots

---

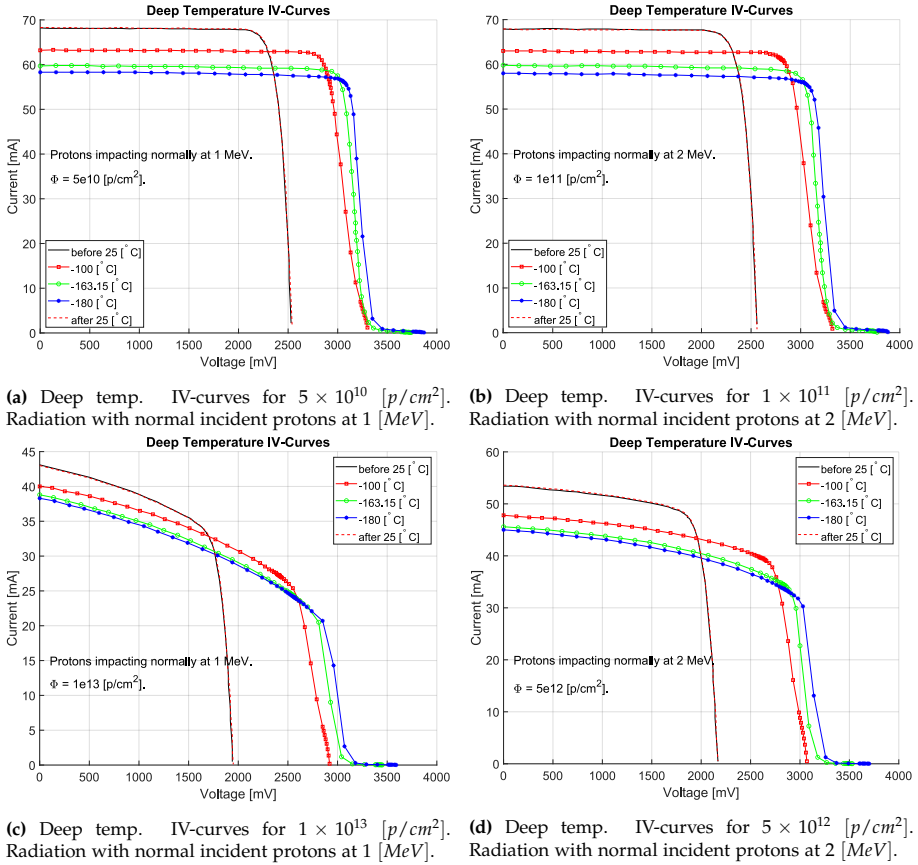[2]It was possible to measure 24 cells in total due to issues related to the company schedule.

(a) Deep temp. IV-curves for 5×10^{10} $[p/cm^2]$. Radiation with normal incident protons at 1 $[MeV]$.

(b) Deep temp. IV-curves for 1×10^{11} $[p/cm^2]$. Radiation with normal incident protons at 2 $[MeV]$.

(c) Deep temp. IV-curves for 1×10^{13} $[p/cm^2]$. Radiation with normal incident protons at 1 $[MeV]$.

(d) Deep temp. IV-curves for 5×10^{12} $[p/cm^2]$. Radiation with normal incident protons at 2 $[MeV]$.

Fig. 5.8: IV-curves of 2×2 $[cm^2]$ PV cells at low temperatures.

show that the corresponding IV-curves before and after the measurements are overlapped as expected. Fig. 5.8a shows the IV-curves for a fluence of 5×10^{10} while Fig. 5.8c for a fluence of 1×10^{13} $[p/cm^2]$, both for PV cells radiated with protons at 1 $[MeV]$ of energy and low temperatures. It should be noticed that a steeper slope appears with the highest fluence regardless the energy of the proton. Besides, the section of the IV-curve to the right of the MPP, which is highly related to the series resistance of the PV cell, changes in shape when the temperature goes down. Indeed, a kind of "tail" is observed just before the open-circuit condition and it is more emphasized at lower temperatures. One possible factor influencing such a behavior might be the way in which such experiments were carried out. Firstly, the cells were set to the low temperature reference, then, the SOSIM shutter was opened and after a second or so, the IV-curve was recorded. Throughout the time of each measurement, a progressive increase of the PV cell temperature was observed

(a) Deep temp. P-curves for 5×10^{10} $[p/cm^2]$. Radiation with normal incident protons at 1 $[MeV]$.

(b) Deep temp. P-curves for 1×10^{11} $[p/cm^2]$. Radiation with normal incident protons at 2 $[MeV]$.

(c) Deep temp. P-curves for 1×10^{13} $[p/cm^2]$. Radiation with normal incident protons at 1 $[MeV]$.

(d) Deep temp. P-curves for 5×10^{12} $[p/cm^2]$. Radiation with normal incident protons at 2 $[MeV]$.
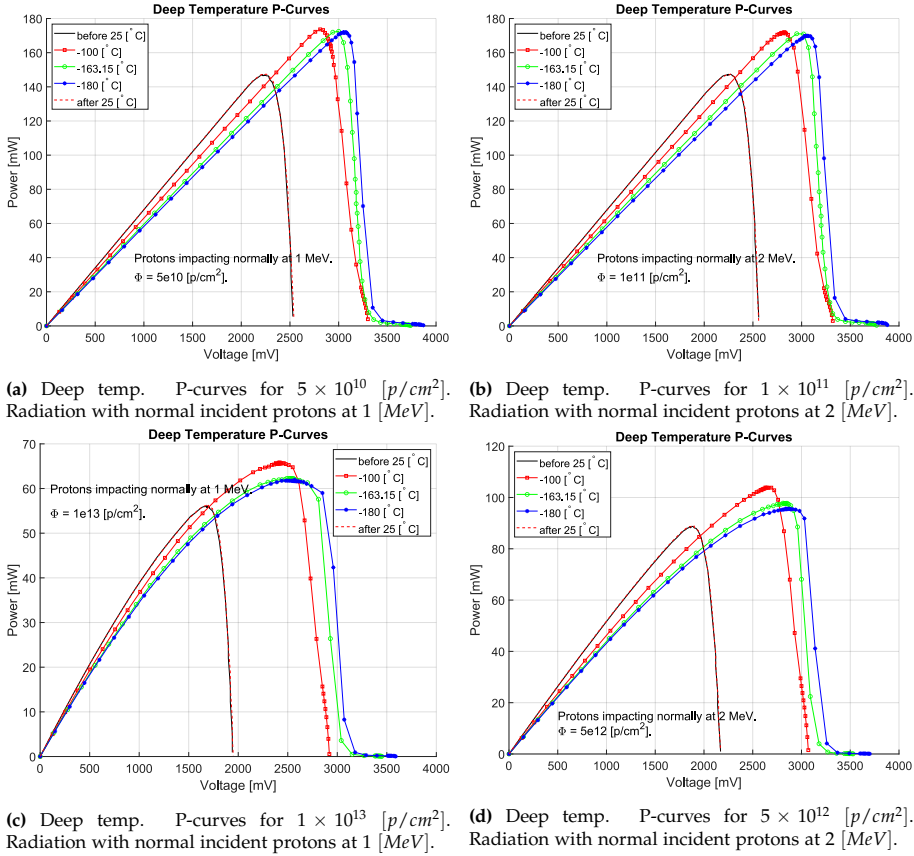
Fig. 5.9: P-curves of 2×2 $[cm^2]$ PV cells at low temperatures.

due to the light. This effect was more notorious at lower temperatures. On the other hand, Fig. 5.8b and Fig. 5.8d show the IV-curves of PV cells radiated by a fluence of 1×10^{11} and 5×10^{12} $[p/cm^2]$, respectively, both with protons at 2 $[MeV]$ of energy and different low temperatures.

Fig. 5.9 shows the output power of radiated PV cells, at low temperatures, by protons at different fluences and energies of 1 and 2 $[MeV]$. Each plot also shows the P-curves before and after the measurement, which are overlapped every time as expected. Due to the extreme low temperature, all the PV cells show an increase of power with respect to the corresponding power at 25 $[°C]$. However, a maximum power is observed at a temperature of -100 $[°C]$ for all the levels of degradation, but becoming more emphasized for the PV cells with the largest degradation (Fig. 5.9c and 5.9d). According to these results, a maximum available power from this kind of PV cells is estimated to be at a temperature between 25 and -163.15 $[°C]$ when the cells have been
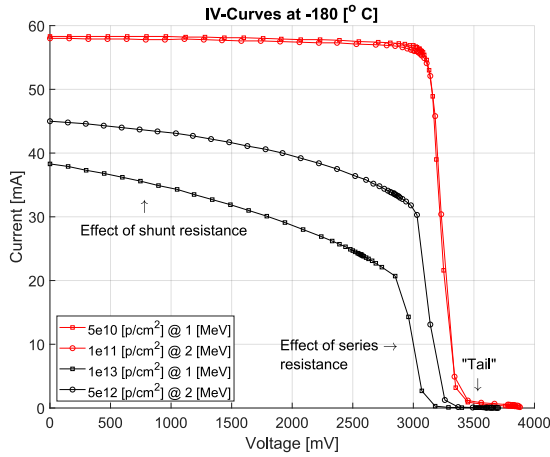
Fig. 5.10: IV-curves of four PV cells at -180 $[°C]$ and radiated by different fluences of protons having energy either 1 or 2 $[MeV]$.

radiated by protons at 1 or 2 $[MeV]$.

Fig. 5.10 shows a comparison of the IV-curves of four similar PV cells radiated at the minimum and maximum fluences of protons considered here. Besides, the protons' energy is either 1 or 2 $[MeV]$ and the cell temperature is -180 $[°C]$. From this figure, steeper IV-curve slopes are observed at the highest fluences in both energies. Furthermore, the sections of the IV-curves usually associated to be related with the shunt and series resistances are indicated, which are changing with the increase of fluence. From this figure, it is confirmed once again that protons having 1 $[MeV]$ of energy induce a higher degradation on the cells than protons having 2 $[MeV]$. For instance, the red profiles show that a fluence of 5×10^{10} $[p/cm^2]$ at 1 $[MeV]$ induce practically the same degradation on the PV cell than a double fluence of protons having 2 $[MeV]$.

5.6   Conclusion

A brief discussion of the experimental results for the characterization of 39 III-V TJ PV cells along with a short introduction to the setups utilized was presented here. The cells utilized for the experiments were of the kind $Ga_{0.5}In_{0.5}P/Ga_{0.99}In_{0.01}As/Ge$, bare, and previously radiated by normally impacting protons having energies of 1 and 2 [MeV]. The measurement of IV-curves confirmed a higher PV cell degradation for higher fluences regarding the same energy of the protons while a higher degradation for the lower energy regarding the same fluence. Such a degradation results

in a reduction of the short-circuit current, open-circuit voltage, maximum power, efficiency, and fill-factor. Besides, the slope increment of the IV-curves between the short-circuit current and MPP conditions was confirmed. On the other hand, the measurement of dark IV-curves confirmed the increase of dark current at RT for radiated PV cells due to the increase of defects created by the radiation. Thus, the larger the degradation level, the higher the dark current presented. Moreover, the measurement of EQE-curves demonstrated the appearance of *artifacts* in radiated PV cells. Besides, such as several previously reported studies, a larger degradation of the GaAs-based layer (middle layer) was observed. Furthermore, the radiated cells presented a lower performance for long-wavelength photons. Finally, performance measurement of radiated PV cells at very low temperatures was carried out with the use of a high vacuum thermal chamber. Unexpected IV-curves were observed with a sort of "tail" just before the open-circuit voltage condition. Such a weird shape gets more emphasized for deeper temperatures. We believe that this behavior has to do with the series resistance dependency on the temperature and possibly with the increase of temperature during the measurement. However, more theoretical and experimental analysis is needed. Besides, an increase of the output power is observed due to the very low temperatures. Nevertheless, the highest MPP is presented at -100 $[^{\circ}C]$ for all the levels of radiation, which might indicate that a maximum output power will be allocated between the RT and -163.15 $[^{\circ}C]$, but more theoretical and experimental analysis is required. This can have important implications for the proper design and sizing of the PV cells for future Lunar missions.

Chapter 6

Illumination Condition on the Lunar South Pole and an Optimal Allocation to Harvest Solar Energy

6.1 Introduction

So far, many organizations have already scheduled missions to our natural satellite looking forward to establish permanent Lunar bases. For instance, the *Artemis program* of NASA for the year 2024 [16], the Lunar base of JAXA for the year 2030 [153], and the International Lunar Research Station (ILRS) of the CNSA/ROSCOSMOS for the year 2036 [18]. However, the settlement of a Lunar base will demand a complete electric power system with very high levels of RRROS. In this regard, recently the concept of SMGs has been proposed, which take advantage of the experience with terrestrial systems in islanded mode [74–77].

In terms of energy generation, the fission based reactors are usually considered as the main energy source for a Lunar base given their advantages in terms of size, weight, modularity, and independence of other environmental features [79, 154]. However, high risks of contamination not only to the environment, but also the crew, exist and proper disposal of wastes must be carried out. Besides, the reactors should be carefully shielded and operated to prevent any disaster. Another technology has been reported aiming to harvest energy from the electrostatic field naturally presented all over the Lunar surface [19]. Nonetheless, this technology

is at laboratory test stage yet. On the other hand, the PV-technology is
a mature and well-tested source of energy for space applications, which
has been utilized since the 1950s by the space sector [86]. Besides, apart
from the fact that sunlight is the main source of energy on the Moon,
PV-technology is safe for the environment and living beings and modular [76,
86]. Nevertheless, issues related to the exposure to micrometeorites, very low
and extreme temperature cycles, deep vacuum, electrostatic fields, radiation
of highly energetic photons (UVs and GCRs) and ion/nuclei particles
degrade the wafers of the PV cells strongly [21, 39]. In this sense, not
only the PV-technology itself is still under study, but also the environmental
conditions that will be faced in outer space.

For the case of the Moon, the illumination condition is among the most
widely studied environmental features. It turns out that some locations near
to the *Shackleton Crater* on the Lunar south pole have continuous illumination
for around six months and posterior periods of light-darkness during the
remaining half year [61, 65, 82]. Therefore, the need of ESSs is compulsory.
However, the current technology of batteries might represent a big issue
regarding the volume and weight, as well as a fast degradation due to
environmental conditions, such as extreme temperatures and radiation of
ion/nuclei particles. In this regard, several studies have been carried out to
characterize the illumination conditions and ESS needs for a human based
upon the Lunar poles [63–68, 155], see Fig. 6.1.

Nevertheless, all such studies are focused mostly to find single-sites
with the highest levels of illumination, which usually results in very tall
structures, especially when the goal is preventing the use of any ESS. In
this sense, recently, it has been proposed to optimally find a combination
between different sites, such as a multi-microgrid (MMG) on Earth, upon
the Lunar south pole. This aims to substantially reduce the ESS or even
eliminate the need of any storage device while keeping the shortest distance
between the sites and night-time [86]. The new technique implements a
novel strategy to process the critical angles[1] from a DEM provided by the
LOLA experiment [85] and the Sun trajectory across the Lunar sky. The
analysis shows that the best compromise solution is found for a two-sites
configuration, one located at 222.7638° longitude, −89.4502° latitude and the
other at 291.5466° longitude, −88.6782° latitude, both with towers of 500
[*m*]. This configuration results in a longest night time of only 13 [*h*] and
a separation between the sites of about 37.246 [*km*]. Additionally, a possible
configuration for preventing the use of any ESS is found at 37.0207 longitude,
−85.2897 latitude, with towers of only 100 [*m*], but having a separation of
158.825 [*km*] between the sites. Moreover, these distances, in the range of

---

[1]The highest angle of the topographic elevations which would be perceived by an observer at
a POI on the Moon.

kilometers, will be able to be overcome in a coming future by using the power transmission by lasers, that is currently under active investigation [156–158], instead of power cables.

This chapter is committed to introduce a new technique to compute the Lunar relief and the Sun trajectory across the Moon's Sky. Then, based on the results of the proposed models, the time-series illumination profiles over a whole axial precession cycle (APC) is computed and compared with previous published studies. The new physical based approximation is suitable for engineering purposes with a high degree of accuracy and simplicity aiming to find the illumination condition of an *n*-sites configuration. This approximation has been already submitted for publication at [86].

6.2 Topography of the Lunar Poles

For this study, the topographic data was obtained from the LOLA experiment, which is still running on the LRO. The resolution of the data provided by LOLA is the highest registered so far. For the radial (R) and along-track (S) axis, the resolutions were reported as $\sim$ 10 and $\sim$ 50 $[m]$, respectively, for the year 2010 [83]. One year after the launching in 2010, [159] reported a cross-track resolution of approximately $0.04°$, which
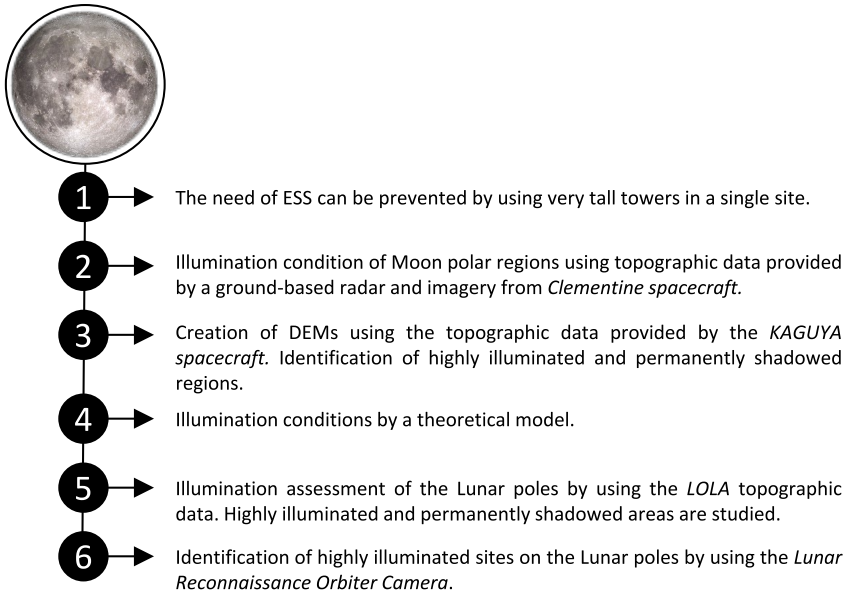

1 The need of ESS can be prevented by using very tall towers in a single site.

2 Illumination condition of Moon polar regions using topographic data provided by a ground-based radar and imagery from *Clementine spacecraft.*

3 Creation of DEMs using the topographic data provided by the *KAGUYA spacecraft.* Identification of highly illuminated and permanently shadowed regions.

4 Illumination conditions by a theoretical model.

5 Illumination assessment of the Lunar poles by using the *LOLA* topographic data. Highly illuminated and permanently shadowed areas are studied.

6 Identification of highly illuminated sites on the Lunar poles by using the *Lunar Reconnaissance Orbiter Camera*.

Fig. 6.1: Some studies regarding the assessment of illumination conditions upon the Lunar poles. 1: [65, 66], 2: [64–66], 3: [67], 4: [63], 5: [68], 6: [155].
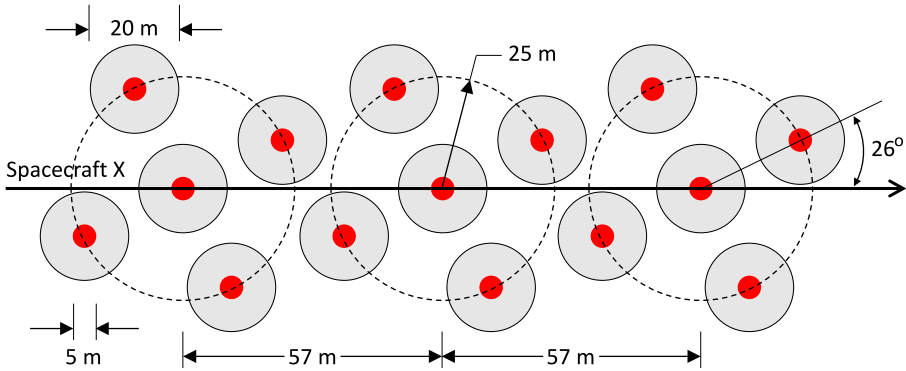
Fig. 6.2: Footprint of the LOLA lasers upon the Moon's surface. The spacecraft LRO can move in both directions of the arrow [86].

corresponds to ~ 1.2 $[km]$ and ~ 200 $[m]$ at the Moon's equator and $\pm 80°$ latitude, respectively. The database, which is updated regularly while more information is collected, was downloaded from [85]. The NASA's orbiter LRO gets the data by means of the LOLA, which splits a laser beam in five parts with an average diameter of 5 $[m]$ each upon the Lunar soil. The orbit is about 50 $[km]$ with a ground-track speed of 1600 $[m/s]$ and a shutting frequency of 28 $[Hz]$, which results in 140 measurements every second [83, 160]. However, the actual valid measurements go from 80 to 90 measurements per second [83]. Besides, regarding the velocity of the orbiter and the round trip time of the laser beam, an ideal resolution should be around the 9 $[cm]$. Nevertheless, the actual resolution achieved is around ~ 12 $[cm]$ [83]. Fig. 6.2 shows the pattern drawn by the lasers over the Lunar surface with the time.

Table 6.1 shows the derived gridded data record (GDR) used for this study, which can be accessed at [85]. The data format comes in the way of a binary image with 16-bit integers and provides the polar stereographic projection of the Lunar soil in one of the Moon's poles. The value of each pixel gives the height of the terrain elevation with respect to an average Lunar

Table 6.1: Database of the DEM used for this study (GDR).

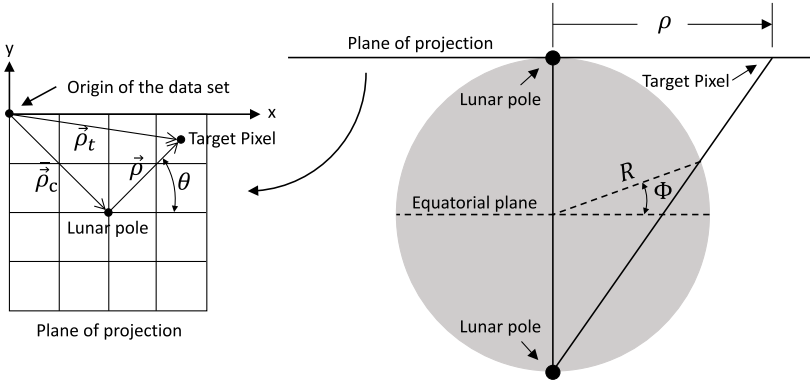| File name: ldem_75s_120m.img		
Variable	**Symbol**	**Value**
Resolution	a	0.120 $[km/pixel]$
	r_{pix}	252.695 $[pixel/deg]$
SF	SF	0.5

Fig. 6.3: Polar stereographic projection of the Lunar terrain in one of the poles [86].

radius and is computed as

$$h = (DV)(SF) + R, \tag{6.1}$$

where h is the elevation of the terrain in $[m]$, DV is the digital-value in $[m]$, $SF = 0.5$ is the scaling factor, and $R \approx 1737400\ [m]$ is the Lunar average radius.

Assuming that the database has origin on the left-top corner of the data array, then, any target pixel inside of the array can be perfectly identified from a framework wit origin at the center of the database (right on the pole) as following, see Fig. 6.3.

$$\vec{\rho} = \vec{\rho}_t - \vec{\rho}_c, \tag{6.2}$$

where $\vec{\rho}$ is a radio-vector with origin at the center of the database (on the pole) and end to a target pixel of the database. Besides, $\vec{\rho}_t$ and $\vec{\rho}_c$ are the radio-vectors with origin at the left-top corner of the database and pointing towards a target pixel and the center of the array, respectively. From Fig. 6.3, it is also possible to obtain the equations for the latitude and longitude as,

$$\Phi = \left[\frac{\pi}{2} - 2\arctan\left(\frac{\rho}{2R}\right) \right] \alpha_{ls} \rightarrow \text{latitude}, \tag{6.3}$$

$$\theta_l = \frac{\pi}{2} - \theta \rightarrow \text{longitude}, \tag{6.4}$$

where α_{ls} has a value of 1 and -1 when refers to north and south latitudes, respectively.

Then, the reference frame can be shifted again to have origin at the POI as follows.

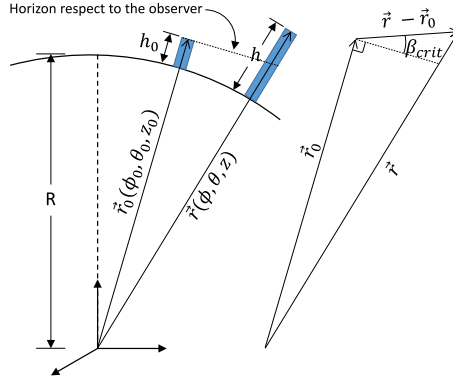$$\vec{\rho}_p = \vec{\rho} - \vec{\rho}_0, \tag{6.5}$$

77

Fig. 6.4: Spherical radio-vectors with origin the Moon's CM and estimation of the critical angle.

where $\vec{\rho}_p$ is the radio-vector with origin at the POI and pointing towards a target pixel, while $\vec{\rho}_0$ is the vector with origin at the database center and end at the POI. Then, a virtual unitary vector pointing towards the Sun and lying on the stereographic projection, $\hat{\rho}_s$, is assumed. The elevation of every pixel on the radio-vector $\hat{\rho}_s$ direction is computed with respect to the POI to estimate the critical angle, see Fig. 6.4. Finally, the critical angle is computed by [86] as

$$\beta_{crit} = \frac{\pi}{2} - \min\left\{\arccos\left[\frac{\vec{r}_0 \cdot (\vec{r} - \vec{r}_0)}{|\vec{r}_0||\vec{r} - \vec{r}_0|}\right]\right\}, \tag{6.6}$$

where $\vec{r}$ is a spherical radio-vector with origin at the Moon's center of mass (CM) and pointing towards a target pixel. The subscript 0 refers to the POI.

6.3 Estimation of the Sun Trajectory

The estimation of the Sun elevation seen from a POI over the Moon can be computed by solving numerically the dynamics of a *three-body problem* represented by the Sun, Earth, and Moon at every time-step, Δt. Thereby, the linear momentum and position of each of these celestial bodies can be approximated by solving the Newton's gravitation law step by step with the
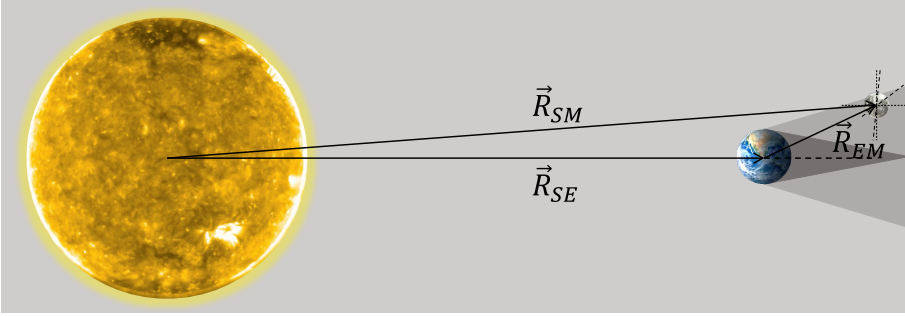
Fig. 6.5: Graphical representation of the *three-body* system analyzed in this study. The figure is not drawn at scale [86].

Euler-method as follows [86],

$$\vec{p}_{n,k} = \vec{p}_{n,k-1} + \vec{F}_{n,k}\Delta t, \quad n = 1,\dots,N, \tag{6.7}$$

$$\vec{R}_{n,k} = \vec{R}_{n,k-1} + \frac{\vec{p}_{n,k}}{m_n}\Delta t, \quad n = 1,\dots,N, \tag{6.8}$$

$$\vec{F}_{n,k} = \sum_{\substack{j=1 \\ j\neq n}}^{N} Gm_n m_j \frac{\vec{R}_{j,k-1} - \vec{R}_{n,k-1}}{\left|\vec{R}_{j,k-1} - \vec{R}_{n,k-1}\right|^3}, \quad n = 1,\dots,N, \tag{6.9}$$

where the subscript k is indicating the time-step at which the respective variable is computed, n is the current selected body, and $N = 3$ is the total number of bodies involved in the study. Besides, $G \approx 6.67408 \times 10^{-11}$ $[m^3/kg - s^2]$ is the gravitational constant, m is the mass of the celestial body, $\vec{R}$ is the position vector of the respective body with origin and the CM of the system, $\vec{p}$ is the linear momentum, and $\vec{F}_n$ is the total force on the body n due to the other bodies. Fig. 6.5 shows graphically a representation of the *three-body* system used for this study.

The position vector joining the CM of the system (It is assumed to be the Sun's CM, see Table 6.2) with the POI on the Moon can be estimated by, see Fig. 6.6,

$$\vec{R}_{Sl} = \vec{R}_{SM} + \vec{r}_{cl}, \tag{6.10}$$

where $\vec{R}_{SM}$ is the vector from the Sun to the Moon and $\vec{r}_{cl}$ is the radius vector from the center of the Moon to the POI. The vector $\vec{r}_{cl}$ is computed in two steps. A vector in a polar reference frame is computed[2] and then transformed

---

[2]Reference frame aligned to the poles and Lunar equatorial plane.

to the precession reference frame. This is done as follows [86], see Fig. 6.7,

$$\vec{r}_{cl} = T_{d,s}\vec{r}_{cl,d}, \tag{6.11}$$

$$T_{d,s} = \begin{bmatrix} \cos\theta_{cn} & -\cos\phi_{cn}\sin\theta_{cn} & -\sin\phi_{cn}\sin\theta_{cn} \\ \sin\theta_{cn} & \cos\phi_{cn}\cos\theta_{cn} & \sin\phi_{cn}\cos\theta_{cn} \\ 0 & -\sin\phi_{cn} & \cos\phi_{cn} \end{bmatrix}, \tag{6.12}$$

$$\theta_{cn} = -\omega_{pres}t + \theta_{cn,0}, \tag{6.13}$$

$$\vec{r}_{cl,d} = \vec{r}_{cl,x}\hat{i} + \vec{r}_{cl,y}\hat{j} + \vec{r}_{cl,z}\hat{k}, \tag{6.14}$$

$$\vec{r}_{cl,x} = |\vec{r}_{cl}|\sin\phi_{cl}\cos\theta_{cl},$$

$$\vec{r}_{cl,y} = |\vec{r}_{cl}|\sin\phi_{cl}\sin\theta_{cl},$$

$$\vec{r}_{cl,z} = |\vec{r}_{cl}|\cos\phi_{cl},$$

$$|\vec{r}_{cl}| = R + h,$$

$$\phi_{cl} = \frac{\pi}{2} - \Phi_l,$$

$$\theta_{cl} = \omega_{mr}t + \theta_{cl,0},$$

$$\omega_{mr} = \frac{|\vec{v}_{EM}|}{|\vec{R}_{EM}|},$$

where the subscript 0 means at the initial condition. The angles ϕ_{cn} and θ_{cn} are the obliquity (inclination) to the Ecliptic plane and the rotational angle due to the precession movement at an angular velocity of ω_{pres}, respectively. The vector $\vec{r}_{cl,d}$ is attached to the polar reference frame while the $\vec{r}_{cl}$ to the precession reference frame. The angle ϕ_{cl} is between the north pole, the Lunar
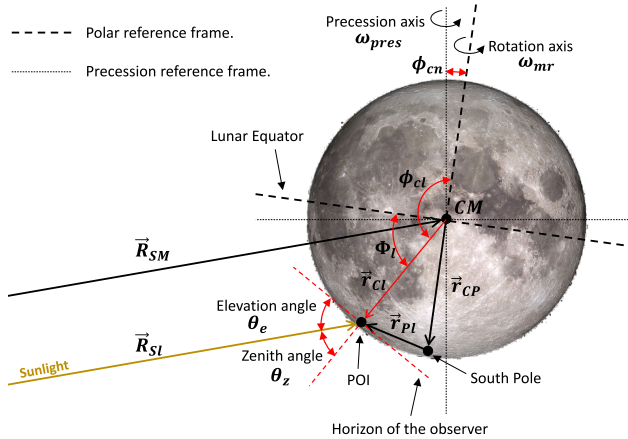

Fig. 6.6: Graphical representation of an arbitrary POI over the Lunar south pole and the two reference frames, namely the polar and precession reference frames. The figure is not drawn at scale [86].
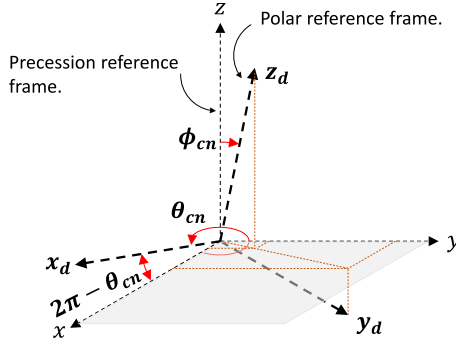
Fig. 6.7: Representation of the polar and precession reference frames [86].

CM, and the POI while θ_{cl} is the rotation angle of the Moon in its own axis. Besides, Φ_l is the POI's latitude. Finally, ω_{mr} is the speed of the Moon's spin and $\vec{v}_{EM}$ and $\vec{R}_{EM}$ are the velocity and position of the Earth respect to the Moon, respectively.

Then, the elevation and zenith angles are computed as follows [86],

$$\theta_e = \frac{\pi}{2} - \theta_z, \tag{6.15}$$

$$\theta_z = \arccos\left(-\frac{\vec{R}_{sl} \cdot \vec{r}_{cl}}{|\vec{R}_{sl}||\vec{r}_{cl}|}\right). \tag{6.16}$$

Please, see Table 6.2 where it is described the main assumptions done for the development of this model. Besides, see Table 6.3 for the physical values used in all the variables described.

6.4 Sites Selection, Validation of Models, and Initial Conditions

Several papers have reported that Lunar poles are suitable for solar energy harvesting [64–66, 68, 155]. In this sense, the selection of twenty previously found sites on the Lunar south pole, by [68], is done for this study and presented on Table 6.4. Then, a seeking around each site was carried out to find out the tallest point. These adjusted sites along with the absolute difference respect to the previously reported sites are also provided on Table 6.4. The origin of such differences is due to many reasons while being among the most important the following [86].

1. The data reported was found with a database updated from July-2009 to February-2010 while the database used for this study is updated seven years more up to February-2017.

81

2. For the reported study the resolution is 240 $[m]$ while for this study is 120 $[m]$.

3. The Sun as viewed from the Moon is considered as a disk whereas for this study is assumed a source point.

4. The reported study linearly interpolates the Lunar relief between two adjacent pixels whereas this study keeps the value constant up to reach the next value.

5. The models used for estimation of the Sun trajectory and Moon orientation are different in the reported and this study.

6. The average illumination is estimated during four APCs in the reported results whereas for this study just one APC is utilized.

On the other hand, the computed Sun trajectory during the whole APC is compared with the results provided by the Horizons System of the JPL of NASA [161]. The results for the site 16 are shown in Fig. 6.8. The error observed belongs in a great extend to the numerical method utilized for solving the three-body problem (Euler method) since it adds a small error every iteration while the error magnitude is proportional to the time-step size. It is suggested by the authors in [86] to use more sophisticated algorithms, such as the Runge-kutta fourth order.

The initial conditions for the simulation were obtained from the conditions of the system Sun-Earth-Moon to date 06-July-2023 [161],

Table 6.2: Assumptions done during the development of this model [86].

1	The Sun-Earth-Moon barycenter is at the CM of the Sun.
2	The Sun-Earth-Moon is a closed system, $\sum_{\forall k} \vec{p}_k = 0$.
3	The initial position of vector $\vec{r}_{cl,d}$, which connects the Lunar CM with the POI, is assumed to be $\theta_{cl} \approx \theta_{l,0} - 260.69^o$. This value was fitted by comparing the result with the Ephemerides [161].
4	The obliquity to the ecliptic, ϕ_{cn}, is assumed constant during the whole axial precession period.
5	It is assumed that ω_{pres} is constant in the whole precession period.
6	The initial θ_{cn} is assumed to be $\theta_{cn,0} \approx 35^o$. This value was fitted by comparing the result with the Ephemerides [161].
7	The model neglects any relativistic effect.
8	The Lunar synodic period (Lunar month) is assumed constant.
9	The Sun is assumed like a source point of light.
10	Eclipses with Earth are not considered.
11	No slopes of the terrain are considered.
12	Reflections are assumed negligible.

Table 6.3: Parameters used for this study [80, 81, 86, 162].

Body	Parameter	Value	Units
Sun	Mass	1988500×10^{24}	$[kg]$
	Sidereal year	365.256	$[days]$
	Av. Distance to Earth	1	$[AU]^*$
Earth	Mass	5.9724×10^{24}	$[kg]$
	Aphelion	152.099×10^9	$[m]$
	Perihelion	147.092×10^9	$[m]$
	Min. orbital velocity	29290	$[m/s]$
Moon	Mass	7.346×10^{22}	$[kg]$
	Apogee	0.4055×10^9	$[m]$
	Perigee	0.3633×10^9	$[m]$
	Orbit inclination	5.145	$[^o]$
	Obliquity to Ecliptic (ϕ_{cn})	1.535	$[^o]$
	Axial precession	18.6	$[yrs]$
	Average radius, R	1737.4×10^3	$[m]$
	Max. orbital velocity	1082	$[m/s]$
	Sidereal period	27.3217	$[days]$
	Synodic period	29.53	$[days]$
	Av. spin vel. (ω_{mr})	$\frac{2\pi}{27.3217 \times 24 \times 3600}$	$[rad/s]$
	Precession ang. vel. (ω_{pres})	$\frac{2\pi}{18.6 \times 365.242 \times 24 \times 3600}$	$[rad/s]$
Bases	Mass	1988500×10^{24}	$[kg]$
	Time	$365.256 \times 24 \times 3600$	$[s]$
	Distance	149597870.7×10^3	$[m]$

* 1 AU is 149597870.7×10^3 $[m]$.

see Fig. 6.9 [86]. Table 6.3 provides the values for the minimum and maximum velocities of Earth and Moon, respectively.

The illumination condition at each POI is obtained by a subtraction of the terrain to the Sun elevation. A complete description of the process followed can be observed on Fig. 6.12. Two examples are shown in Fig. 6.10 and Fig. 6.11 for the Sites 1 and 20, respectively, and a height of 100 $[m]$ each.

6.5 Optimal Selection of Sites

The sunlight availability would be of vital importance for a PV-based Lunar station. In this regard, to be able to harvest solar energy still during darkness periods, it is proposed to setup any Lunar base like a MMG, which can be named space multi-microgrid (SMMG). The distribution of the PV system in different locations on the Moon will increase naturally the level of RRROS of

Table 6.4: Highly illuminated sites on the Lunar south pole at a height of 10 [m] [86]. The last column provides the absolute error between the adjusted positions and the sites reported by [68].

#	Long.	Lat.	Average illumination (%)	Adjusted Long.	Adjusted Lat.	Average illumination (%)	Absolute Error (%)
1	222.69	-89.45	93.10	222.6627	-89.4511	0.9184	1.2634
2	222.73	-89.43	92.53	222.6415	-89.4333	0.8509	7.4435
3	223.28	-89.44	92.26	222.8084	-89.4390	0.9168	0.5780
4	204.27	-89.78	87.41	203.6490	-89.7797	0.8690	0.5090
5	203.46	-89.77	87.42	203.2861	-89.7731	0.8434	3.0807
6	37.07	-85.30	87.30	37.1013	-85.2963	0.7884	8.4630
7	123.64	-88.81	85.59	123.7604	-88.8084	0.8494	0.6544
8	197.05	-89.69	85.93	197.1382	-89.6866	0.8618	0.2459
9	222.14	-89.44	91.86	222.4191	-89.4407	0.9176	0.1007
10	37.01	-85.30	87.33	37.0207	-85.2897	0.8244	4.8861
11	291.90	-88.67	84.74	291.7803	-88.6704	0.8612	1.3844
12	198.43	-89.69	85.19	197.7447	-89.6884	0.8018	5.0133
13	202.69	-89.76	86.88	202.8645	-89.7624	0.8239	4.4913
14	222.59	-89.47	89.57	222.5634	-89.4734	0.8787	1.6973
15	223.25	-89.45	91.82	222.7638	-89.4502	0.9223	0.4067
16	291.58	-88.68	84.68	291.5466	-88.6782	0.8441	0.2707
17	205.14	-89.79	86.19	203.8539	-89.7880	0.8197	4.2172
18	37.57	-85.55	82.62	37.5851	-85.5405	0.7524	7.3826
19	123.95	-88.80	84.92	123.9526	-88.8025	0.6758	17.3381
20	31.73	-85.43	83.32	31.7488	-85.4099	0.8362	0.3016

the entire system. Besides, the longest night period is reduced while a short distance between the adjusted sites is kept.

Even when the technique proposed by [86] is limited for 20 sites, see Table 6.4, the effectiveness of the proposed technique can be improved by increasing the number of sites and their type. However, an increase of the processing time should be expected.

The optimal selection of the sites is carried out like an optimization problem, where the objective function (OF) is defined as follows [86],

$$OF = a\frac{N_h - N_{h,min}}{N_{h,max} - N_{h,min}} + b\frac{L - L_{min}}{L_{max} - L_{min}}, \tag{6.17}$$

where a and b are the weight factors, which meet the condition $a + b = 1$. Besides, the subscripts min and max represent the minimum and maximum value of the respective variable. Moreover, N_h and L are the longest night-period of the whole APC and the total distance of all the sites connected together in a ring-configuration, respectively. The particle swarm optimization (PSO) algorithm is used to solve the problem. For these
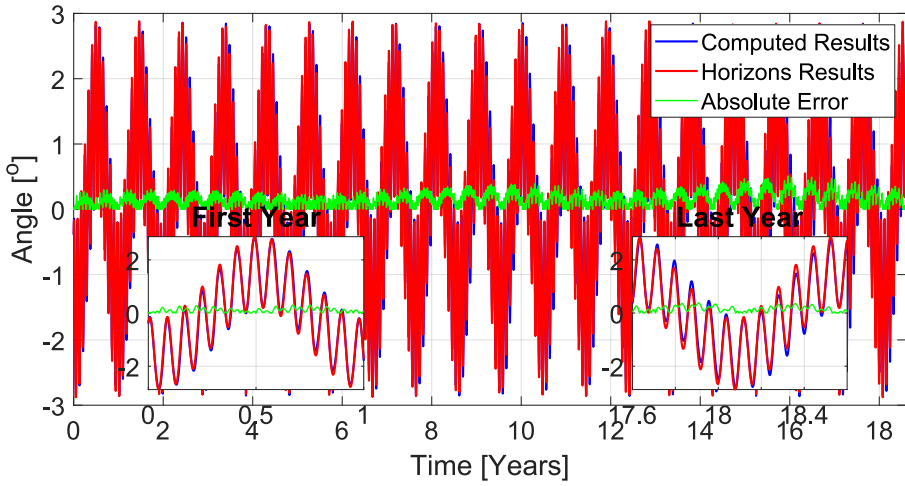
Fig. 6.8: Sun trajectory during one APC from 06-July-2023 to 14-February-2042. The computed results are compared with the trajectory provided by the Horizons System of the JPL of NASA [161]. The left-hand inset shows a zoom into the first year while the right-hand inset into the last year [86].
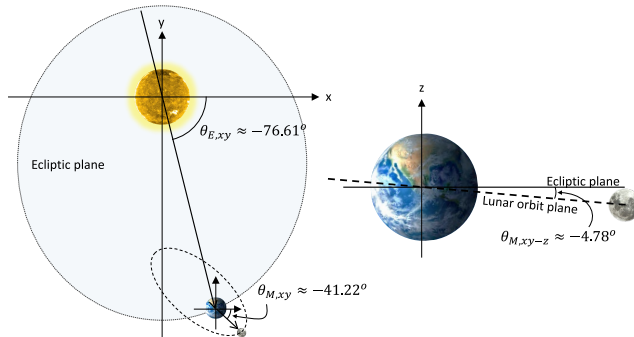

Fig. 6.9: Initial conditions of the three-body problem Sun-Earth-Moon to date 06-July-2023 [86, 161].

adjusted sites, it was found $N_{h,min} = 0$, $N_{h,max} = 313$ $[h]$, $L_{min} = 0$, and $L_{max} = 380.0286$ $[km]$.

The best compromise solution was sought by changing the number of selected sites from 1 to 5 and the tower height between 10, 100, and 500 $[m]$. The decision vector for the optimization problem contains the ID number given to each selected site, see Table 6.4.

Fig. 6.10: Graphical representation of the critical elevation angles shaping the Lunar relief around
the Site 1 and the Sun trajectory. The thick red line is the terrain elevation while the thick blue
profile gives the illumination condition where 0 means darkness and 1 light. The colorful profiles
describe the trajectory of the Sun during the whole APC. Besides, the thick dashed and black
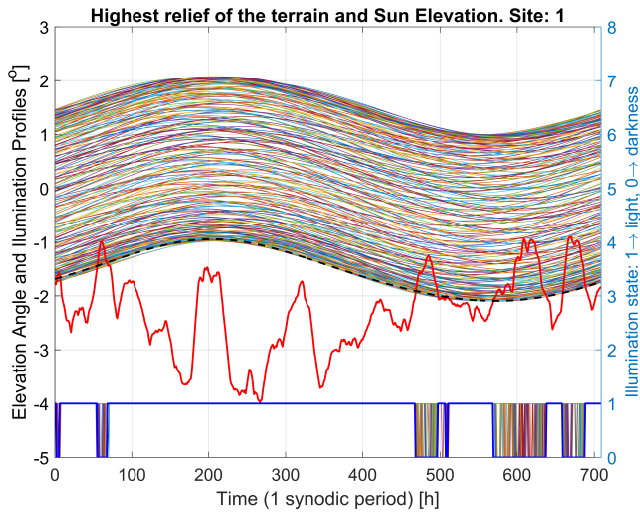line is highlighting the worst Lunar day (WLD) [86].

Fig. 6.11: Graphical representation of the critical elevation angles shaping the Lunar relief around
the Site 20 and the Sun trajectory. The thick red line is the terrain elevation while the thick blue
profile gives the illumination condition where 0 means darkness and 1 light. The colorful profiles
describe the trajectory of the Sun during the whole APC. Besides, the thick dashed and black
line is highlighting the WLD [86].

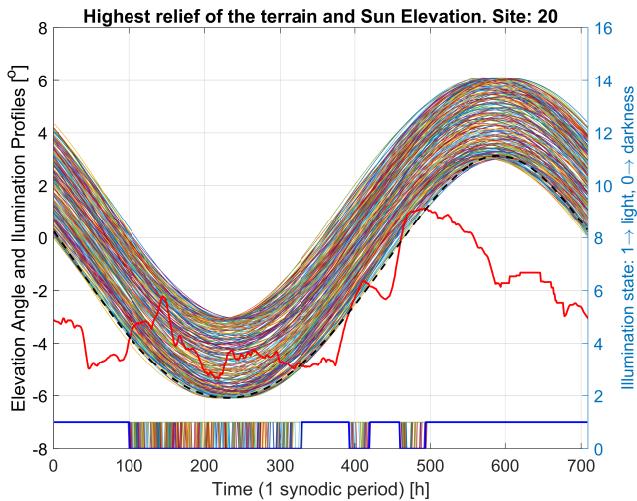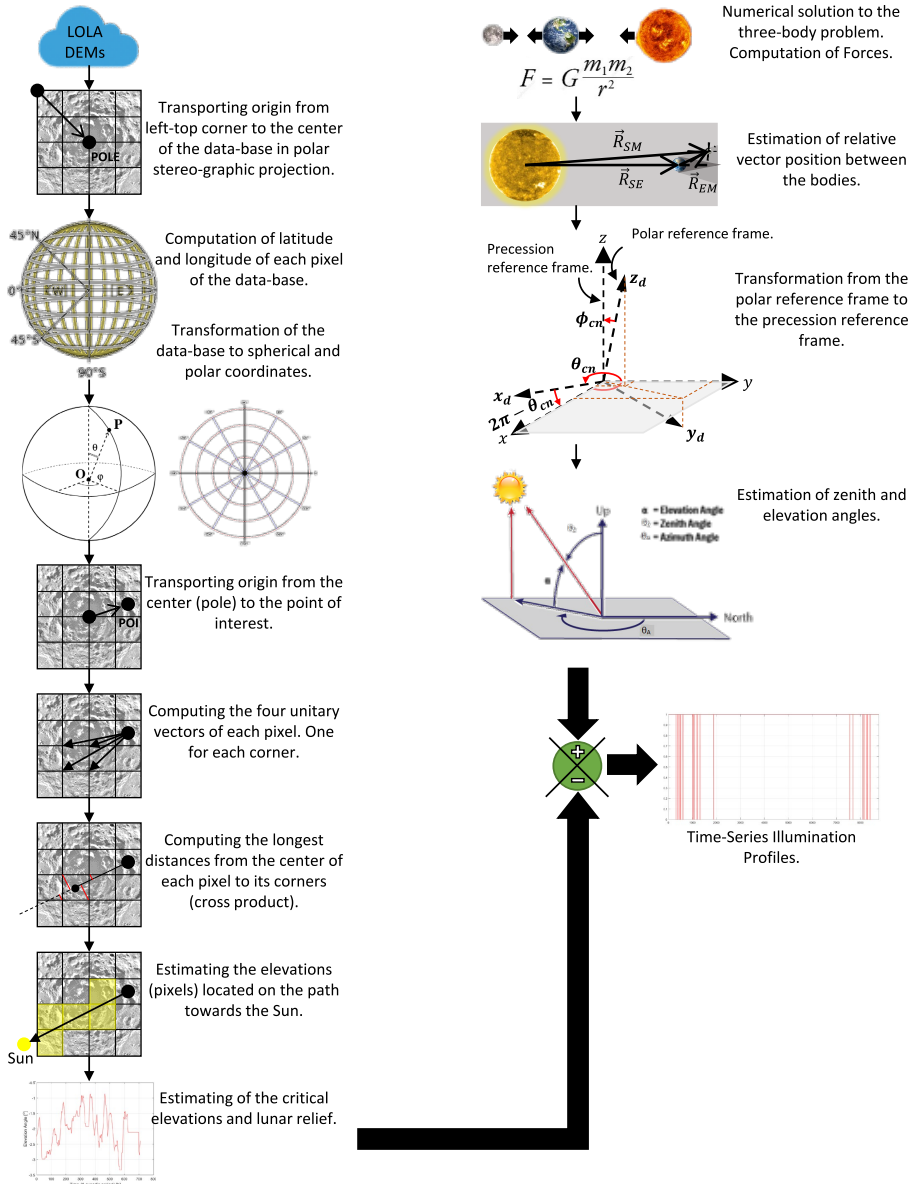**Fig. 6.12:** Flowchart of the process followed to compute the time-series illumination profile of a single site.

6.6 Results

The search for the best compromise solution is done by a sweep of weight values from $a = 0$ to $a = 1.0$ in steps of 0.1, and from $b = 1.0$ to $b = 0$,

Table 6.5: Selection of the best compromise site configuration for each tower-height (first row of each feature) and the site configuration with the shortest longest-night period for each tower-height (second row of each feature) [86].

Tower height = 10 [m]						
No. of sites	One	Two	Three	Four	Five	Six
Arrangement	4	$7-14$	$14-19-7$	$14-15-1-7$	$15-14-7-9-1$	$1-14-7-9-3-5$
of sites[1]	-	$7-14$	$14-11-7$	$17-7-14-16$	$17-16-14-7-4$	$17-4-5-7-14-16$
Longest	69	29	29	29	29	29
night [h]		29	10	10	10	10
shortest	1	1	1	1	1	1
day [h]		1	18	18	18	18
Total	0	83.446	84.0131	84.5871	84.9547	85.2244
distance[2] [km]		83.446	155.5108	154.9688	155.1966	155.4243
Tower height = 100 [m]						
No. of sites	One	Two	Three	Four	Five	Six
Arrangement	4	$14-7$	$13-8-16$	$13-16-12-8$	$5-16-12-8-13$	$8-12-16-4-5-13$
of sites[1]	-	**$10-14$**	$14-16-7$	$16-17-7-14$	$4-7-14-16-17$	$4-5-7-14-16-17$
Longest	61	28	27	27	27	27
night [h]		**0**	9	9	9	9
shortest	1	1	1	1	1	1
day [h]		**C.I.**	21	630	630	630
Total	0	83.446	84.6495	84.6592	84.8369	85.0202
distance[2] [km]		**317.6517**	154.8194	154.9688	155.1966	155.4243
Tower height = 500 [m]						
No. of sites	One	Two	Three	Four	Five	Six
Arrangement	3	**$15-16$**	$16-3-15$	$1-15-16-3$	$9-2-16-15-1$	$9-3-16-11-15-1$
of sites[1]	-	**$16-17$**	$16-3-7$	$3-16-7-9$	$16-17-7-9-3$	$16-7-14-1-15-3$
Longest	40	**13**	13	13	13	13
night [h]		**11**	2	2	2	2
shortest	1	**2**	2	2	2	2
day [h]		**3**	631	631	631	631
Total	0	**74.4915**	74.8027	75.0116	75.5412	76.0899
distance[2] [km]		**80.2754**	155.3202	155.373	155.5225	155.7416

[1] The sites should be connected in the order they are indicated. The sites are in ring-configuration. [2] In ring configuration. C.I.: Continuously illuminated.

accordingly. The best solution for each set of weight factors is found by the PSO algorithm. The same analysis is carried out for each tower height, *i.e.* 10, 100, and 500 [m], and the best compromise solution for each configuration is presented on the first row of each feature in Table 6.5. The best compromise solution is found by using the well-known *membership technique* giving a weight of 70% to the longest night and 30% to the total length. Besides, the second row in each feature of Table 6.5 gives the result of the configuration with the shortest longest-night time.

From Table 6.5, the shortest night-time for single site configurations is about 69, 61, and 40 [h] for tower heights of 10, 100, and 500 [m], respectively. After two-sites configurations with a tower height of only 10 [m], the longest night-time can be reduced drastically up to 29 [h] but separations of more than 40 [km] between the sites. The same situation can be observed with
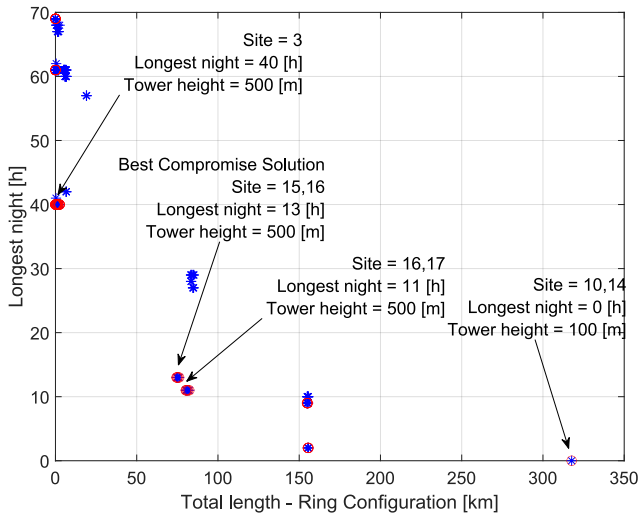
Fig. 6.13: Candidate solutions. The non-dominated solutions are emphasized by red circles [86].

the configurations considering tower height of 100 [m], but the need of ESS can be eliminated thankfully. For configurations of two-sites having tower height of 500 [m], the longest night-time can be reduced up to 11 or 13 [h] while having separations of around 40 [km] and 37 [km], respectively. For more than two sites, it is possible to practically prevent the use of any ESS while having tower heights of 500 [m]. However, distances in terms of tens of kilometers should be covered.

Fig. 6.13 shows a group of candidate solutions while the *Pareto front*, or non-dominant solutions, is highlighted by red circles. Again, the membership approximation technique is used to take a decision of the best compromise solution while giving a weight factor of 70% to the longest night and 30% to the total length. According to the results, the best compromise solution is comprised of a two-sites configuration (15 and 16) in towers of 500 [m] and having a separation of about 37.24 [km] between the sites. Nonetheless, it is also observed a solution to prevent the use of any ESS with a two sites configuration (10 and 14), but having a separation between the sites of about 158.82 [km].

The Fig. 6.14 shows the individual illumination profiles of the sites 15 and 16, as well as the time-series illumination profile of the same two-sites configuration for the first year. The condition of zero means darkness, one means that just one site is illuminated, and two means that both sites are simultaneously illuminated. As it can be observed, the combination of both sites reduces the number of darkness (no-energy). Moreover, Fig. 6.15 shows the stereographic projection of the Lunar south pole where the adjusted sites
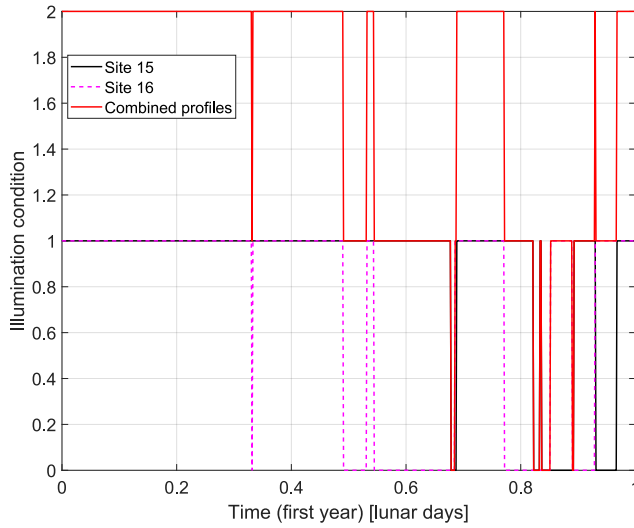
Fig. 6.14: Time-series illumination profiles of site 15 and 16, as well as the combination profile of both sites [86].

given on Table 6.4 are indicated. Besides, the best feasible solution (sites 15 and 16) are joined by a red-dashed line and the configuration to prevent the use of any ESS is joined by a gree-dashed line. The position of the sites of interest, emphasizes the possibility of transmit the power wirelessly by using lasers in a coming future. This is not only because there are not obstacles that can interrupt the shortest distance between the sites, but also because the too rough Lunar relief.
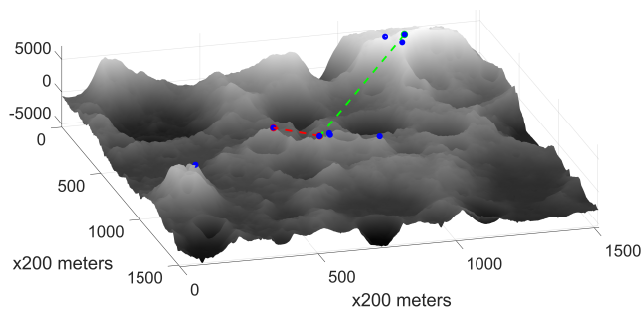

Fig. 6.15: Stereographic projection of the Lunar south pole with the adjusted sites used for this study, see Table 6.4. Besides, the best compromise solution (red-dashed line) and the solution to prevent the use of any ESS (green-dashed line) are presented [86].

6.7 Conclusions

This chapter has presented a new technique recently proposed to compute the time-series illumination profile around a POI on the south pole. The results were compared with previous reported values, resulting in good agreements. The differences between both results was due to factors like the resolution, time-span of the data-sets, interpretation of the data between two consecutive pixels, *etc.* Besides, a new technique recently proposed for the Sun elevation estimation in any point of the Lunar poles is also presented. The results for a whole APC were compared with the data provided by the Horizons System of the JPL of NASA. It was suggested that the main source of error was due to the type of numerical method utilized to solve the three-body problem comprised of the celestial bodies *Sun-Earth-Moon*. Additionally, a new recently proposed technique to harvest the solar energy from the Lunar poles was presented. Instead of collecting the energy from a single-site, the proposal is to harvest energy from multiple sites while keeping the shortest possible distance between the sites. The objective functions are to minimize the longest night-time while keeping the shortest total distance between the sites in a ring configuration. According to the results, the best compromise solution on the south pole is a two-sites configuration with $500 \, [m]$ height towers, having a separation of about 37.25 $[km]$ between the sites. The Site 15 is located at longitude $222.76°$ and latitude $-89.45°$ while the Site 16 at longitude $291.55°$ and latitude $-88.68°$. Moreover, a two-sites configuration (site 10 and 14) prevents the use of any ESS with $100 \, [m]$ towers but having a separation of more than $150 \, [km]$. Even though the separation between the sites is in terms of kilometers, it is deeply believed that such distances can be shortened by increasing the number and type of sites involved in the optimization problem. Besides, it is also believed that the current developments on the power beaming technology will help to overcome such distances while preventing the use of long power cables.

Chapter 6. Illumination Condition on the Lunar South Pole and an Optimal
Allocation to Harvest Solar Energy

Chapter 7

Conclusions and Future Works

7.1 Overall Conclusion

The humankind is preparing to colonize other celestial bodies, but still many challenges should be overcome to apply successfully the PV-technology with a high level of RRROS for energy generation in places relatively close to the Sun. Besides, even though the PV is a well-tested and mature technology, it has to meet many more and much more demanding requirements than its terrestrial counterparts. When the terrestrial applications look for a higher efficiency at a lower price, the space applications look for lightweight, small, and radiation resistance PV cells, *etc.* Regarding the degradation due to particle radiation of PV cells based on Si and III-V materials, the main challenges identified in this thesis work are: *1.* Still the GaAs-based layer in the PV cells is usually reported as the main responsible for the whole PV cell degradation. *2.* The directionality of the electronic cloud in the semiconductors' crystal is still not properly considered. *3.* There is lack of a proper model for the interfaces' degradation. *4.* The study of PV performance at extreme temperatures and light intensities is still on the first stages. *5.* There is still a discussion about the origin of the steeper IV slope appearing after the radiation of PV cells.

On the other hand, the improved physical-based model for the PV systems proposed to use in this thesis have shown to be much more accurate than other currently used models. The better accuracy is not only around the MPP as usually assessed in the literature, but also in the whole voltage range starting from the short-circuit to the open-circuit condition. Besides, the model has proven to be more accurate in a much wider range of

temperatures and light intensities than current models. Furthermore, the results have a physical interpretation, unlike some approximations with a high accuracy but no physical meaning. However, the use of tuning parameters is still a drawback of this new approximation, which can be overcome by more theoretical analysis and experimental data. Additionally, the results confirmed as well that the MC Si-based PV cells are better in quality than the PV cells based on PC technology.

The experimental characterization of the TJ III-V PV cells confirmed several of the previously identified effects reported by other authors. The techniques utilized for the characterization are the illuminated IV-curves, dark IV-curves, and EQE-curves at RT, while IV-curves at -100, -163.15, and -180 $[°C]$. Among the effects identified are the larger degradation induced by protons having 1 $[MeV]$ than protons having 2 $[MeV]$, the degradation increase with the fluence regardless the energy of the particle (considering only the two energies of this study), the steeper slope of the IV-curves after the radiation, increase of the dark current, among many others. Some unexpected results appeared as well. The IV-curve of radiated PV cells at very low temperatures presents an anomalous "tail", which can be due to the experimental procedure and/or the dependency of the series resistance on the temperature and bias voltage. However, more theoretical and experimental work is required to clarify it. The output power of the PV cells increased by the low temperatures, but reaching a maximum level, which is estimated to be allocated between 25 and -163.15 $[°C]$.

Finally, the method proposed to use for the optimal allocation of a space MMG has shown to be very effective in reducing significantly the ESS size while keeping a distance between the sites in the range of tens of kilometers. However, a much shorter distance between the sites could be estimated if more potential locations on the Moon are simultaneously analyzed by the optimizer, but a longer processing time should be expected. Besides, it is expected that the new technology for power transmission based on laser/microwaves can help to overcome the issue of the distance between the sites. On the other hand, the height of the towers to allocate the PV system has been reduced hugely from the range of kilometers, according to the current literature, to the range of meters, which makes the solution more feasible. The method includes a new technique to compute the Lunar relief around any POI on the Lunar poles and based on the topographic data provided by the LOLA experiment on the LRO orbiter of NASA. The technique has shown to match closely to other current solutions. Another novel technique to estimate the Sun elevation in the Lunar sky is also proposed, which matches very closely to the results provided by the Horizons System of NASA.

All the authors expect that this work contributes in paving the way to improve the current PV-technology and modeling for applications into SMGs

with a much higher level of RRROS.

7.2   Future Research Perspectives

Several gaps on the research of III-V/Si based PV cells for application in space environments were identified during the development of this thesis work. However, some of the issues/drawbacks/gaps have been planned to be addressed in the coming future. Each point has been listed and briefly introduced in the following.

1. *A new model for the slowed-down spectrum of energetic charged particles traveling across a shielding.* This model is under progress and some preliminary results are available right away. However, the current model is based on the continuous slowing-down approximation (CSDA) considering only the electronic stopping power (ESP) while the nuclear stopping power (NSP) is assumed to be negligible, which makes to have considerable error at low energies with respect to the results provided by the software packages SPENVIS/MULASSIS and SRIM. The advantage of a physical-based model is the higher speed with results having physical meaning.

2. *A new physical-based model for the degradation mechanism due to radiation of nuclei particles on MJ III-V PV cells.* The model is planned to be based on a mixture between Monte-Carlo simulations and a better physical approximation taking into account the directionality of the electronic clouds in each kind of compound. The experimental data obtained during the research stay will be used to validate the modeling. One of the reasons behind this physical-based model is to give an explanation to the challenges identified. Namely, the larger degradation of the GaAs compound in comparison to others, the degradation in the interfaces between the subcells of the PV cell, the actual origin of the steeper slope of the IV-curves after the radiation, the effects of the electronic cloud directionality on the degradation, and to explain the unexpected results in the experimental data.

3. *Further experimental tests.* The new experimental setups will be defined during and after the modeling of the particle radiation-induced degradation of PV cells based on III-V materials. The new experiments will involved the use of electrons for radiation at different energies and fluences. Besides, it is desirable to experiment with new architectures. The new results will help to clarify all the challenges described in the last point.

4. *Improvement of the physical-based model for the PV cells proposed here.* Even though the proposed model described in this thesis for the PV cell has shown a higher accuracy than other currently used models and in different situations, the need for tuning parameters exist yet. Therefore, a further physical analysis is planned to be carried out to reduce or even avoid the use of tuning parameters while keeping a high accuracy and low processing time.

5. *A new method to identify highly illuminated sites on the Moon.* For the strategy proposed here to find the most optimal arrangement of sites to harvest solar energy on the Lunar south pole, twenty previously identified POIs were used. Therefore, it is planned to improve the strategy proposed here to compute the Lunar relief around any POI in a faster way, since currently this is the most demanding routine in terms of computational resources. Thus, the estimation of highly illuminated places within a short processing time will be possible. Then, the optimizer will be able to analyze a larger number and type of sites. Indeed, it is also planned to change the heuristic solver for a more accurate algorithm, such as the TLBO method, to prevent local minima. Finally, a more sophisticated numerical solver for the three-body problem, such as the Runge Kutta Fourth Order, is planned to be used to reduce the error between the model and the highly accurate Horizons system of NASA.

6. *Use the illumination profiles to compute the temperature in any place over the Lunar surface.* A physical-based model to compute the temperature upon the Lunar surface is of paramount importance for future Lunar missions. Therefore, it is planned to assess the current methodologies to estimate the temperature over the surface of the Moon, and in the case of being necessary, either improve or formulate a new model based on the previous estimation of the time-series illumination profiles.

7. *An integral model for the power generation, shielding, and degradation of the PV cells in outer space conditions.* The ultimate goal is to create a *Simulink* block with an *easy-to-use* interface to allow future researchers to use directly in their models including PV cells in outer space conditions. The planned integral model will have the option to be used either for offline applications with a high accuracy, or for online applications, such as digital twining with a faster processing time but a reduced accuracy.

Bibliography

References

[1] A. Mann. (2021, oct) Starlink: SpaceX's satellite internet project. [Online]. Available: https://www.space.com/spacex-starlink-satellites.html

[2] L. Grush. (2021, oct) Roscosmos says it will send two tourists to the space station in 2023 — and one of them will spacewalk. [Online]. Available: https://www.theverge.com/2020/6/25/21302941/roscosmos-space-adventures-tourists-spacewalk-2023-iss

[3] V. Stein. (2021, oct) Inspiration4: The first all-civilian spaceflight on SpaceX Dragon. [Online]. Available: https://www.space.com/inspiration4-spacex.html

[4] E. Arevalo. (2021, oct) DearMoon Project Announces They Already Selected Finalists That Could Ride SpaceX's First Crewed Starship Flight. [Online]. Available: https://www.tesmanian.com/blogs/tesmanian-blog/dearmoon-1

[5] E. S. . Security. (2021, oct) Risky asteroids. [Online]. Available: https://www.esa.int/Safety_Security/Risky_asteroids

[6] J. P. L. C. I. of Technology. (2021, oct) Psyche. [Online]. Available: https://www.jpl.nasa.gov/missions/psyche

[7] N. Aeronautics and S. Administration. (2021, oct) OSIRIS-REx. [Online]. Available: https://www.nasa.gov/osiris-rex

[8] ——. (2021, oct) NASA's Dragonfly Will Fly Around Titan Looking for Origins, Signs of Life. [Online]. Available: https://www.nasa.gov/press-release/nasas-dragonfly-will-fly-around-titan-looking-for-origins-signs-of-life

[9] E. S. Agency. (2021, oct) Juice. [Online]. Available: https://sci.esa.int/web/juice

[10] ——. (2021, oct) Exomars - Has life ever existed on Mars? [Online]. Available: https://www.esa.int/Science_Exploration/Human_and_Robotic_Exploration/Exploration/ExoMars

[11] N. Aeronautics and S. Administration. (2021, oct) Mars Exploration Program. [Online]. Available: https://mars.nasa.gov/

[12] J. A. E. Agency. (2021, oct) MMX Martian Moons Exploration. [Online]. Available: https://www.mmx.jaxa.jp/en/

[13] N. Aeronautics and S. Administration. (2021, oct) Lunar Reconnaissance Orbiter. [Online]. Available: https://lunar.gsfc.nasa.gov/

[14] A. Jones. (2021, oct) 1,000 days on the moon! China's Chang'e 4 lunar far side mission hits big milestone. [Online]. Available: https://www.space.com/china-chang-e-4-moon-far-side-1000-days

References

[15] N. Aeronautics and S. Administration. (2021, oct) Gateway. [Online]. Available: https://www.nasa.gov/gateway/overview

[16] ——. (2021, oct) Artemis. [Online]. Available: https://www.nasa.gov/specials/artemis/

[17] SpaceX. (2021, oct) Mars & Beyond - The road to making humanity multiplanetary. [Online]. Available: https://www.spacex.com/human-spaceflight/mars/

[18] T. Pultarova. (2021, oct) Russia, China reveal moon base roadmap but no plans for astronaut trips yet. [Online]. Available: https://www.space.com/china-russia-international-lunar-research-station

[19] S. H. Choi, G. C. King, H.-J. Kim, and Y. Park, "Electrostatic Power Generation from Negatively Charged, Simulated Lunar Regolith," *Rn*, vol. 3, no. R2, p. R1, 2010. [Online]. Available: https://ntrs.nasa.gov/api/citations/20100032922/downloads/20100032922.pdf

[20] A. Bermudez-Garcia, P. Voarino, and O. Raccurt, "Environments, needs and opportunities for future space photovoltaic power generation: A review," *Applied Energy*, vol. 290, p. 116757, 2021. [Online]. Available: https://www.sciencedirect.com/science/article/pii/S030626192100266X

[21] E. F. Lisbona, "llf-2 - Calibration, testing and monitoring of space solar cells," in *Solar Cells*, T. Markvart and L. Castañer, Eds. Oxford: Elsevier Science, 2005, pp. 475–503, doi: doi:https://doi.org/10.1016/B978-185617457-2/50019-6. [Online]. Available: https://www.sciencedirect.com/science/article/pii/B9781856174572500196

[22] X. Zhao, A. Aierken, M. Heini, M. Tan, Y. Wu, S. Lu, R. Hao, J. Mo, Y. Zhuang, X. Shen, Y. Xu, Q. Lei, and Q. Guo, "Degradation characteristics of electron and proton irradiated InGaAsP/InGaAs dual junction solar cell," *Solar Energy Materials and Solar Cells*, vol. 206, p. 110339, 2020, doi: doi:https://doi.org/10.1016/j.solmat.2019.110339. [Online]. Available: https://www.sciencedirect.com/science/article/pii/S0927024819306658

[23] S. Z. Karazhanov, "Mechanism for the anomalous degradation of silicon space solar cells," *Applied Physics Letters*, vol. 76, no. 19, pp. 2689–2691, 2000, doi: doi:10.1063/1.126445. [Online]. Available: https://doi.org/10.1063/1.126445

[24] S. Park, J. C. Bourgoin, H. Sim, C. Baur, V. Khorenko, O. Cavani, J. Bourcois, S. Picard, and B. Boizot, "Space degradation of 3J solar cells: I—Proton irradiation," *Progress in Photovoltaics: Research and Applications*, vol. 26, no. 10, pp. 778–788, 2018, doi: doi:https://doi.org/10.1002/pip.3016. [Online]. Available: https://onlinelibrary.wiley.com/doi/abs/10.1002/pip.3016

[25] S. J. Taylor, M. Yamaguchi, T. Yamaguchi, S. Watanabe, K. Ando, S. Matsuda, T. Hisamatsu, and S. I. Kim, "Comparison of the effects of electron and proton irradiation on n+–p–p+ silicon diodes," *Journal of Applied Physics*, vol. 83, no. 9, pp. 4620–4627, 1998, doi: doi:10.1063/1.367246. [Online]. Available: https://doi.org/10.1063/1.367246

[26] M. Yamaguchi, S. J. Taylor, S. Matsuda, and O. Kawasaki, "Mechanism for the anomalous degradation of Si solar cells induced by high fluence 1 MeV electron irradiation," *Applied Physics Letters*, vol. 68, no. 22, pp. 3141–3143, 1996, doi: doi:10.1063/1.115804. [Online]. Available: https://doi.org/10.1063/1.115804

[27] N. Gruginskie, F. Cappelluti, G. J. Bauhuis, P. Mulder, E. J. Haverkamp, E. Vlieg, and J. J. Schermer, "Electron radiation–induced degradation of GaAs solar cells with different architectures," *Progress in Photovoltaics: Research and Applications*, vol. 28, no. 4, pp. 266–278, 2020, doi: doi:https://doi.org/10.1002/pip.3224. [Online]. Available: https://onlinelibrary.wiley.com/doi/abs/10.1002/pip.3224

[28] M. Imaizumi, M. Yamaguchi, S. Taylor, S. Matsuda, O. Kawasaki, and T. Hisamatsu, "Mechanism for the anomalous degradation of Si solar cells induced by high-energy proton irradiation," *Solar Energy Materials and Solar Cells*, vol. 50, no. 1, pp. 339 – 344, 1998, doi: doi:https://doi.org/10.1016/S0927-0248(97)00164-5. [Online]. Available: http://www.sciencedirect.com/science/article/pii/S0927024897001645

References

[29] S.-i. Sato, T. Ohshima, and M. Imaizumi, "Modeling of degradation behavior of InGaP/GaAs/Ge triple-junction space solar cell exposed to charged particles," *Journal of Applied Physics*, vol. 105, no. 4, p. 044504, 2009, doi: doi:10.1063/1.3079522. [Online]. Available: https://doi.org/10.1063/1.3079522

[30] S. ichiro Sato, H. Miyamoto, M. Imaizumi, K. Shimazaki, C. Morioka, K. Kawano, and T. Ohshima, "Degradation modeling of InGaP/GaAs/Ge triple-junction solar cells irradiated with various-energy protons," *Solar Energy Materials and Solar Cells*, vol. 93, no. 6, pp. 768–773, 2009, 17th International Photovoltaic Science and Engineering Conference. doi: doi:https://doi.org/10.1016/j.solmat.2008.09.044. [Online]. Available: https://www.sciencedirect.com/science/article/pii/S0927024808003140

[31] T. Takamoto, M. Yamaguchi, S. J. Taylor, M.-J. Yang, E. Ikeda, and H. Kurita, "Radiation resistance of high-efficiency InGaP/GaAs tandem solar cells," *Solar Energy Materials and Solar Cells*, vol. 58, no. 3, pp. 265–276, 1999, doi: doi:https://doi.org/10.1016/S0927-0248(99)00003-3. [Online]. Available: https://www.sciencedirect.com/science/article/pii/S0927024899000033

[32] M. Yamaguchi, A. Khan, S. J. Taylor, M. Imaizumi, T. Hisamatsu, and S. Matsuda, "A detailed model to improve the radiation-resistance of Si space solar cells," *IEEE Transactions on Electron Devices*, vol. 46, no. 10, pp. 2133–2138, 1999, doi: doi:10.1109/16.792008.

[33] M. Zazoui and J. C. Bourgoin, "Space degradation of multijunction solar cells: An electroluminescence study," *Applied Physics Letters*, vol. 80, no. 23, pp. 4455–4457, 2002, doi: doi:10.1063/1.1485134. [Online]. Available: https://doi.org/10.1063/1.1485134

[34] C. Peng, F. Ding, Z. Lei, Z. Zhang, Y. En, and Y. Huang, "Investigation of radiation-induced degradations in four-junction solar cell by experiment and simulation," *Microelectronics Reliability*, vol. 108, p. 113646, 2020, doi: doi:https://doi.org/10.1016/j.microrel.2020.113646. [Online]. Available: https://www.sciencedirect.com/science/article/pii/S0026271419311229

[35] S. R. Messenger, E. A. Burke, R. J. Walters, J. H. Warner, G. P. Summers, and T. L. Morton, "Effect of Omnidirectional Proton Irradiation On Shielded Solar Cells," *IEEE Transactions on Nuclear Science*, vol. 53, no. 6, pp. 3771–3778, 2006, doi: doi:10.1109/TNS.2006.886220.

[36] G. P. Summers, S. R. Messenger, E. A. Burke, M. A. Xapsos, and R. J. Walters, "Contribution of low-energy protons to the degradation of shielded GaAs solar cells in space," *Progress in Photovoltaics: Research and Applications*, vol. 5, no. 6, pp. 407–413, 1997, doi: doi:https://doi.org/10.1002/(SICI)1099-159X(199711/12)5:6<407::AID-PIP192>3.0.CO;2-P. [Online]. Available: https://onlinelibrary.wiley.com/doi/abs/10.1002/%28SICI%291099-159X%28199711/12%295%3A6%3C407%3A%3AAID-PIP192%3E3.0.CO%3B2-P

[37] A. Aierken, L. Fang, M. Heini, Q. Zhang, Z. Li, X. Zhao, M. Sailai, H. Liu, Q. Guo, W. Gao, H. Gao, and Q. Sun, "Effects of proton irradiation on upright metamorphic GaInP/GaInAs/Ge triple junction solar cells," *Solar Energy Materials and Solar Cells*, vol. 185, pp. 36–44, 2018, doi: doi:https://doi.org/10.1016/j.solmat.2018.04.035. [Online]. Available: https://www.sciencedirect.com/science/article/pii/S0927024818302095

[38] R. Lang, J. Schön, J. Lefèvre, B. Boizot, F. Dimroth, and D. Lackner, "Radiation hardness and post irradiation regeneration behavior of GaInAsP solar cells," *Solar Energy Materials and Solar Cells*, vol. 211, p. 110551, 2020, doi: doi:https://doi.org/10.1016/j.solmat.2020.110551. [Online]. Available: https://www.sciencedirect.com/science/article/pii/S0927024820301549

[39] J. M. Raya-Armenta, N. Bazmohammadi, J. C. Vasquez, and J. M. Guerrero, "A short review of radiation-induced degradation of III–V photovoltaic cells for space applications," *Solar Energy Materials and Solar Cells*, vol. 233, p. 111379, 2021. [Online]. Available: https://www.sciencedirect.com/science/article/pii/S0927024821004219

References

[40] H. W. Jones, "The Recent Large Reduction in Space Launch Cost," in *48th International Conference on Environmental Systems*, jul 2018.

[41] M. Karamirad, M. Omid, R. Alimardani, H. Mousazadeh, and S. N. Heidari, "ANN based simulation and experimental verification of analytical four- and five-parameters models of PV modules," *Simulation Modelling Practice and Theory*, vol. 34, pp. 86 – 98, 2013.

[42] Y. Mahmoud and E. El-Saadany, "Accuracy improvement of the ideal pv model," *IEEE Transactions on Sustainable Energy*, vol. 6, no. 3, pp. 909–911, 2015.

[43] Y. Mahmoud, W. Xiao, and H. H. Zeineldin, "A Simple Approach to Modeling and Simulation of Photovoltaic Modules," *IEEE Transactions on Sustainable Energy*, vol. 3, no. 1, pp. 185–186, Jan 2012.

[44] B. K. Dey, I. Khan, N. Mandal, and A. Bhattacharjee, "Mathematical modelling and characteristic analysis of Solar PV Cell," in *2016 IEEE 7th Annual Information Technology, Electronics and Mobile Communication Conference (IEMCON)*, 2016, pp. 1–5.

[45] A. Coelho and R. Castro, "Experimental validation of PV power output prediction models," in *2012 IEEE International Conference on Industrial Technology*, 2012, pp. 705–710.

[46] M. G. Villalva, J. R. Gazoli, and E. R. Filho, "Comprehensive Approach to Modeling and Simulation of Photovoltaic Arrays," *IEEE Transactions on Power Electronics*, vol. 24, no. 5, pp. 1198–1208, 2009.

[47] K. Ishaque, Z. Salam, H. Taheri, and Syafaruddin, "Modeling and simulation of photovoltaic (PV) system during partial shading based on a two-diode model," *Simulation Modelling Practice and Theory*, vol. 19, no. 7, pp. 1613 – 1626, 2011.

[48] W. D. Soto, S. Klein, and W. Beckman, "Improvement and validation of a model for photovoltaic array performance," *Solar Energy*, vol. 80, no. 1, pp. 78 – 88, 2006.

[49] D. Sera, R. Teodorescu, and P. Rodriguez, "PV panel model based on datasheet values," in *2007 IEEE International Symposium on Industrial Electronics*, June 2007, pp. 2392–2396.

[50] A. A. Elbaset, H. Ali, and M. A.-E. Sattar], "Novel seven-parameter model for photovoltaic modules," *Solar Energy Materials and Solar Cells*, vol. 130, pp. 442 – 455, 2014.

[51] K. Yu, X. Chen, X. Wang, and Z. Wang, "Parameters identification of photovoltaic models using self-adaptive teaching-learning-based optimization," *Energy Conversion and Management*, vol. 145, pp. 233 – 246, 2017.

[52] S. Li, W. Gong, X. Yan, C. Hu, D. Bai, and L. Wang, "Parameter estimation of photovoltaic models with memetic adaptive differential evolution," *Solar Energy*, vol. 190, pp. 465 – 474, 2019.

[53] B. Yang, J. Wang, X. Zhang, T. Yu, W. Yao, H. Shu, F. Zeng, and L. Sun, "Comprehensive overview of meta-heuristic algorithm applications on PV cell parameter identification," *Energy Conversion and Management*, vol. 208, p. 112595, 2020.

[54] A. Mellit, M. Benghanem, and S. Kalogirou, "Modeling and simulation of a stand-alone photovoltaic system using an adaptive artificial neural network: Proposition for a new sizing procedure," *Renewable Energy*, vol. 32, no. 2, pp. 285 – 313, 2007.

[55] A. N. Celik, "Artificial neural network modelling and experimental verification of the operating current of mono-crystalline photovoltaic modules," *Solar Energy*, vol. 85, no. 10, pp. 2507 – 2517, 2011.

[56] J. Ziegler. (2021, jun) SRIM - The Stopping and Range of Ions in Matter. [Online]. Available: http://www.srim.org/

[57] S. R. Messenger, E. A. Burke, T. L. Morton, G. P. Summers, R. J. Walters, and J. H. Warner, "Modelling low energy proton radiation effects on solar cells," in *3rd World Conference on Photovoltaic Energy Conversion, 2003. Proceedings of*, vol. 1, 2003, pp. 716–719 Vol.1. [Online]. Available: https://ieeexplore.ieee.org/abstract/document/1305382

References

[58] C. Weiss, S. Park, J. Lefèvre, B. Boizot, C. Mohr, O. Cavani, S. Picard, R. Kurstjens, T. Niewelt, and S. Janz, "Electron and proton irradiation effect on the minority carrier lifetime in SiC passivated p-doped Ge wafers for space photovoltaics," *Solar Energy Materials and Solar Cells*, vol. 209, p. 110430, 2020, doi: doi:https://doi.org/10.1016/j.solmat.2020.110430. [Online]. Available: https://www.sciencedirect.com/science/article/pii/S0927024820300362

[59] W. Rong, L. Yunhong, and S. Xufang, "Effects of 0.28–2.80MeV proton irradiation on GaInP/GaAs/Ge triple-junction solar cells for space use," *Nuclear Instruments and Methods in Physics Research Section B: Beam Interactions with Materials and Atoms*, vol. 266, no. 5, pp. 745–749, 2008, doi: doi:https://doi.org/10.1016/j.nimb.2007.12.076. [Online]. Available: https://www.sciencedirect.com/science/article/pii/S0168583X07018678

[60] R. B. I. for Space Aeronomy. (2021, jun) SPENVIS - The Space Environment Information System. [Online]. Available: https://www.spenvis.oma.be/intro.php

[61] H. J. Fincannon, *Lunar Environment and Lunar Power Needs*. Springer Handbook Series Contribution, May 2020. [Online]. Available: https://ntrs.nasa.gov/citations/20205002224

[62] J. Gruener, D. Bussey, S. Lawrence, and L. Mason, "Polar Volatiles Exploration in Peary Crater Enabled by NASA's Kilopower Project," in *Lunar Polar Volatiles Meeting*, 2018. [Online]. Available: https://ui.adsabs.harvard.edu/abs/2018LPICo2087.5042G/abstract

[63] X. Li, S. Wang, Y. Zheng, and A. Cheng, "Estimation of solar illumination on the Moon: A theoretical model," *Planetary and Space Science*, vol. 56, no. 7, pp. 947–950, 2008, doi: doi:https://doi.org/10.1016/j.pss.2008.02.008.

[64] J. Fincannon, *Lunar Polar Illumination for Power Analysis*. American Institute of Aeronautics and Astronautics, July 2008. [Online]. Available: https://arc.aiaa.org/doi/abs/10.2514/6.2008-5631

[65] ——, *Characterization of Lunar Polar Illumination from a Power System Perspective*. American Institute of Aeronautics and Astronautics, January 2008. [Online]. Available: https://arc.aiaa.org/doi/abs/10.2514/6.2008-447

[66] ——, *Lunar South Pole Illumination: Review, Reassessment, and Power System Implications*. American Institute of Aeronautics and Astronautics, June 2007. [Online]. Available: https://arc.aiaa.org/doi/abs/10.2514/6.2007-4700

[67] H. Noda, H. Araki, S. Goossens, Y. Ishihara, K. Matsumoto, S. Tazawa, N. Kawano, and S. Sasaki, "Illumination conditions at the lunar polar regions by KAGUYA (SELENE) laser altimeter," *Geophysical research letters*, vol. 35, no. 24, 2008.

[68] E. Mazarico, G. Neumann, D. Smith, M. Zuber, and M. Torrence, "Illumination conditions of the lunar polar regions using LOLA topography," *Icarus*, vol. 211, no. 2, pp. 1066–1081, 2011. [Online]. Available: https://www.sciencedirect.com/science/article/pii/S0019103510004203

[69] E. Sefton-Nash, M. Siegler, and D. Paige, "Thermal extremes in permanently shadowed regions at the lunar south pole," in *Proceedings of the 44th Lunar and Planetary Science Conference*. Lunar and Planetary Institute, 2013, p. 2617.

[70] J. M. Raya-Armenta, P. R. Ortega, N. Bazmohammadi, S. V. Spataru, J. C. Vasquez, and J. M. Guerrero, "An Accurate Physical Model for PV Modules With Improved Approximations of Series-Shunt Resistances," *IEEE Journal of Photovoltaics*, vol. 11, no. 3, pp. 699–707, 2021. [Online]. Available: https://doi.org/10.1109/JPHOTOV.2021.3056668

[71] D. M. Hurley, M. Sarantos, C. Grava, J.-P. Williams, K. D. Retherford, M. Siegler, B. Greenhagen, and D. Paige, "An analytic function of lunar surface temperature for exospheric modeling," *Icarus*, vol. 255, pp. 159–163, 2015, lunar Volatiles. [Online]. Available: https://www.sciencedirect.com/science/article/pii/S0019103514004606

References

[72] G.-P. Hu, Y.-C. Zheng, A.-A. Xu, and Z.-S. Tang, "Lunar Surface Temperature of Global Moon: Preparation of Database With Topographic and Albedo Effects," *IEEE Geoscience and Remote Sensing Letters*, vol. 13, no. 1, pp. 110–114, 2016. [Online]. Available: https://doi.org/10.1109/LGRS.2015.2499305

[73] G. Hu, K. Chen, Q. Huang, W. Guo, Q. Li, L. Gui, and Y. Cheng, "Brightness temperature calculation of lunar crater: Interpretation of topographic effect on microwave data from chang'e," *IEEE Transactions on Geoscience and Remote Sensing*, vol. 52, no. 8, pp. 4499–4510, 2014. [Online]. Available: https://doi.org/10.1109/TGRS.2013.2282342

[74] A. D. Bintoudi, C. Timplalexis, G. Mendes, J. M. Guerrero, and C. Demoulias, "Design of Space Microgrid for Manned Lunar Base: Spinning-in Terrestrial Technologies," in *2019 European Space Power Conference (ESPC)*, 2019, pp. 1–8. [Online]. Available: https://doi.org/10.1109/ESPC.2019.8932024

[75] A. Lashab, M. Yaqoob, Y. Terriche, J. C. Vasquez, and J. M. Guerrero, "Space Microgrids: New Concepts on Electric Power Systems for Satellites," *IEEE Electrification Magazine*, vol. 8, no. 4, pp. 8–19, 2020. [Online]. Available: https://doi.org/10.1109/MELE.2020.3026436

[76] D. Saha, N. Bazmohammadi, J. M. Raya-Armenta, A. D. Bintoudi, A. Lashab, J. C. Vasquez, and J. M. Guerrero, "Space Microgrids for Future Manned Lunar Bases: A Review," *IEEE Open Access Journal of Power and Energy*, pp. 1–1, 2021. [Online]. Available: https://doi.org/10.1109/OAJPE.2021.3116674

[77] C. Ciurans, N. Bazmohammadi, J. C. Vasquez, G. Dussap, J. M. Guerrero, and F. Godia, "Hierarchical Control of Space Closed Ecosystems: Expanding Microgrid Concepts to Bioastronautics," *IEEE Industrial Electronics Magazine*, vol. 15, no. 2, pp. 16–27, 2021. [Online]. Available: https://doi.org/10.1109/MIE.2020.3026828

[78] NASA. (2021, may) Space Technology Mission Directorate. [Online]. Available: https://www.nasa.gov/mission_pages/tdm/fission-surface-power/index.html

[79] A. J. Colozza, "Small Lunar Base Camp and In Situ Resource Utilization Oxygen Production Facility Power System Comparison," National Aeronautics and Space Administration (NASA), contractor report, mar 2020. [Online]. Available: https://ntrs.nasa.gov/citations/20200001622

[80] D. R. Williams. (2020, jan) Moon Fact Sheet. NASA Goddard Space Flight Center. [Online]. Available: https://nssdc.gsfc.nasa.gov/planetary/factsheet/moonfact.html

[81] ——. (2020, feb) Earth Fact Sheet. NASA Goddard Space Flight Center. [Online]. Available: https://nssdc.gsfc.nasa.gov/planetary/factsheet/earthfact.html

[82] J. Freeh, *Analysis of Stationary, Photovoltaic-Based Surface Power System Designs at the Lunar South Pole*. Aerospace Research Central, 2008. [Online]. Available: https://arc.aiaa.org/doi/abs/10.2514/6.2008-7810

[83] D. E. Smith, M. T. Zuber, G. A. Neumann, F. G. Lemoine, E. Mazarico, M. H. Torrence, J. F. McGarry, D. D. Rowlands, J. W. Head III, T. H. Duxbury, O. Aharonson, P. G. Lucey, M. S. Robinson, O. S. Barnouin, J. F. Cavanaugh, X. Sun, P. Liiva, D.-d. Mao, J. C. Smith, and A. E. Bartels, "Initial observations from the Lunar Orbiter Laser Altimeter (LOLA)," *Geophysical Research Letters*, vol. 37, no. 18, 2010. [Online]. Available: https://agupubs.onlinelibrary.wiley.com/doi/abs/10.1029/2010GL043751

[84] M. K. Barker, E. Mazarico, G. A. Neumann, D. E. Smith, M. T. Zuber, and J. W. Head, "Improved LOLA elevation maps for south pole landing sites: Error estimates and their impact on illumination conditions," *Planetary and Space Science*, vol. 203, p. 105119, 2021. [Online]. Available: https://www.sciencedirect.com/science/article/pii/S0032063320303329

[85] NASA. PDS Geosciences Node Data and Services: LRO LOLA. (Accessed on 01/12/2020). [Online]. Available: https://pds-geosciences.wustl.edu/missions/lro/lola.htm

References

[86] J. M. Raya-Armenta, N. Bazmohammadi, J. C. Vasquez, and J. M. Guerrero, "Optimal Allocation of a PV-Based Lunar Multi-Microgrid Based on a Novel Method to Estimate Sun Illumination Profiles," *Submitted to IEEE Transactions on Smart Grid*, 2021.

[87] J. Oberst, A. Christou, R. Suggs, D. Moser, I. Daubar, A. McEwen, M. Burchell, T. Kawamura, H. Hiesinger, K. Wünnemann, R. Wagner, and M. Robinson, "The present-day flux of large meteoroids on the lunar surface—A synthesis of models and observational techniques," *Planetary and Space Science*, vol. 74, no. 1, pp. 179–193, 2012, scientific Preparations For Lunar Exploration. [Online]. Available: https://www.sciencedirect.com/science/article/pii/S0032063312002966

[88] C. S. Ruschel, F. P. Gasparin, E. R. Costa, and A. Krenzinger, "Assessment of pv modules shunt resistance dependence on solar irradiance," *Solar Energy*, vol. 133, pp. 35 – 43, 2016.

[89] J. Arora, A. Verma, and M. Bhatnagar, "Variation of series resistance with temperature and illumination level in diffused junction poly-and single-crystalline silicon solar cells," *Journal of materials science letters*, vol. 5, no. 12, pp. 1210–1212, 1986.

[90] G. Hongliang, S. Linfeng, S. Qiang, Z. Qiming, W. Yiyong, X. Jingdong, G. Bin, and Z. Yanqing, "Degradation of up-grown metamorphic InGaP/InGaAs/Ge solar cells by low-energy proton irradiation," *Solar Energy Materials and Solar Cells*, vol. 191, pp. 399–405, 2019, doi: doi:https://doi.org/10.1016/j.solmat.2018.11.033. [Online]. Available: https://www.sciencedirect.com/science/article/pii/S0927024818305580

[91] M. S. Chowdhury, K. S. Rahman, T. Chowdhury, N. Nuthammachot, K. Techato, M. Akhtaruzzaman, S. K. Tiong, K. Sopian, and N. Amin, "An overview of solar photovoltaic panels' end-of-life material recycling," *Energy Strategy Reviews*, vol. 27, p. 100431, 2020.

[92] S. Philipps and W. Warmuth, "Photovoltaics report 2021." Fraunhofer Institute for Solar Energy Systems, ISE with support of PSE Projects GmbH, Tech. Rep., 2021, accessed 27 July 2021. [Online]. Available: https://www.ise.fraunhofer.de/en/publications/studies/photovoltaics-report.html

[93] X. Li, G. Li, H. Lu, and W. Zhang, "> 35% 5-junction space solar cells based on the direct bonding technique," *Journal of Semiconductors*, pp. 1–7, 2021.

[94] R. R. King, D. C. Law, K. M. Edmondson, C. M. Fetzer, G. S. Kinsey, H. Yoon, R. A. Sherif, and N. H. Karam, "40% efficient metamorphic GaInP/GaInAs/Ge multijunction solar cells," *Applied Physics Letters*, vol. 90, no. 18, p. 183516, 2007.

[95] T. Torchynska and G. Polupan, "III-V material solar cells for space application," *Semiconductor Physics Quantum Electronics & Optoelectronics*, pp. 063–070, 2002.

[96] E. A. Silva, F. Bradaschia, M. C. Cavalcanti, and A. J. Nascimento, "Parameter Estimation Method to Improve the Accuracy of Photovoltaic Electrical Model," *IEEE Journal of Photovoltaics*, vol. 6, no. 1, pp. 278–285, 2016.

[97] E. Moshksar and T. Ghanbari, "Adaptive Estimation Approach for Parameter Identification of Photovoltaic Modules," *IEEE Journal of Photovoltaics*, vol. 7, no. 2, pp. 614–623, 2017.

[98] G. Li, C. Wang, J. Lu, and H. Zhang, "Temperature impact on parameters of In0.3Ga0.7As PV cell under laser irradiation condition," *AIP Advances*, vol. 9, no. 9, p. 095053, 2019.

[99] D. Fébba, R. Rubinger, A. Oliveira, and E. Bortoni, "Impacts of temperature and irradiance on polycrystalline silicon solar cells parameters," *Solar Energy*, vol. 174, pp. 628 – 639, 2018.

[100] E. A. Silva, F. Bradaschia, M. C. Cavalcanti, A. J. Nascimento, L. Michels, and L. P. Pietta, "An Eight-Parameter Adaptive Model for the Single Diode Equivalent Circuit Based on the Photovoltaic Module's Physics," *IEEE Journal of Photovoltaics*, vol. 7, no. 4, pp. 1115–1123, 2017.

References

[101] A. J. Nascimento, M. C. Cavalcanti, F. Bradaschia, E. A. Silva, L. Michels, and L. P. Pietta, "Parameter estimation technique for double-diode model of photovoltaic modules," in *2017 Brazilian Power Electronics Conference (COBEP)*, 2017, pp. 1–6.

[102] B. J. Hallam, P. G. Hamer, R. S. Bonilla, S. R. Wenham, and P. R. Wilshaw, "Method of Extracting Solar Cell Parameters From Derivatives of Dark I–V Curves," *IEEE Journal of Photovoltaics*, vol. 7, no. 5, pp. 1304–1312, 2017.

[103] Z. Salam, K. Ishaque, and H. Taheri, "An improved two-diode photovoltaic (PV) model for PV system," in *2010 Joint International Conference on Power Electronics, Drives and Energy Systems 2010 Power India*, 2010, pp. 1–5.

[104] P. K. Pandey and K. S. Sandhu, "Multi diode modelling of PV cell," in *2014 IEEE 6th India International Conference on Power Electronics (IICPE)*, 2014, pp. 1–4.

[105] S. P. Aly, S. Ahzi, and N. Barth, "An adaptive modelling technique for parameters extraction of photovoltaic devices under varying sunlight and temperature conditions," *Applied Energy*, vol. 236, pp. 728 – 742, 2019.

[106] M. E. Elnagi Mahmoud, A. A. Zaki Diab, and D. A. Kotin, "Simulation and Experimental Validation of Two-Diode Model of Photovoltaic (PV) Modules," in *2018 XIV International Scientific-Technical Conference on Actual Problems of Electronics Instrument Engineering (APEIE)*, 2018, pp. 244–251.

[107] S. Sze and K. Ng, *Physics of Semiconductor Devices*. Wiley, 2006. [Online]. Available: https://books.google.dk/books?id=o4unkmHBHb8C

[108] S. Jain and D. Roulston, "A simple expression for band gap narrowing (BGN) in heavily doped Si, Ge, GaAs and GexSi1- x strained layers," *Solid-State Electronics*, vol. 34, no. 5, pp. 453–465, 1991.

[109] H. P. D. Lanyon and R. A. Tuft, "Bandgap narrowing in moderately to heavily doped silicon," *IEEE Transactions on Electron Devices*, vol. 26, no. 7, pp. 1014–1018, 1979.

[110] J. Wagner, "Band-gap narrowing in heavily doped silicon at 20 and 300 K studied by photoluminescence," *Phys. Rev. B*, vol. 32, pp. 1323–1325, Jul 1985.

[111] K. Safa, K. Cyril, and R. H. E., *Electrical Conduction in Metals and Semiconductors*. Cham: Springer International Publishing, 2017, pp. 1–1. [Online]. Available: https://doi.org/10.1007/978-3-319-48933-9_2

[112] S. O. Kasap, *Principles of electronic materials and devices*. Tata McGraw-Hill, 2006.

[113] W. Ananda, "External quantum efficiency measurement of solar cell," in *2017 15th International Conference on Quality in Research (QiR) : International Symposium on Electrical and Computer Engineering*, 2017, pp. 450–456.

[114] S. Chander, A. Purohit, A. Nehra, S. Nehra, and M. Dhaka, "A study on spectral response and external quantum efficiency of mono-crystalline silicon solar cell," *International Journal of Renewable Energy Research (IJRER)*, vol. 5, no. 1, pp. 41–44, 2015.

[115] M. Zouine, M. Akhsassi, N. Erraissi, N. Aarich, A. Bennouna, M. Raoufi, and A. Outzourhit, "Mathematical Models Calculating PV Module Temperature Using Weather Data: Experimental Study," in *International Conference on Electronic Engineering and Renewable Energy*. Springer, 2018, pp. 630–639.

[116] M. Akhsassi, A. E. Fathi], N. Erraissi, N. Aarich, A. Bennouna, M. Raoufi, and A. Outzourhit, "Experimental investigation and modeling of the thermal behavior of a solar PV module," *Solar Energy Materials and Solar Cells*, vol. 180, pp. 271 – 279, 2018.

[117] J. A. Kratochvil, W. E. Boyson, and D. L. King, *Photovoltaic array performance model*. United States. Department of Energy, 8 2004.

References

[118] M. Salzberger, M. Rutzinger, C. Nömayr, P. Lugli, and C. G. Zimmermann, "Voltage-dependent photocurrent in irradiated GaAs solar cells," *Progress in Photovoltaics: Research and Applications*, vol. 26, no. 5, pp. 317–323, 2018, doi: doi:https://doi.org/10.1002/pip.2983. [Online]. Available: https://onlinelibrary.wiley.com/doi/abs/10.1002/pip.2983

[119] S. I. Maximenko, M. P. Lumb, J. Moore, L. C. Hirst, M. K. Yakes, and P. P. Jenkins, "Thin GaAs Solar Cells For High Irradiation Levels," in *2019 IEEE 46th Photovoltaic Specialists Conference (PVSC)*, 2019, pp. 2814–2817, doi: doi:10.1109/PVSC40753.2019.8980879.

[120] N. Gruginskie, F. Cappelluti, M. van Eerden, G. Bauhuis, P. Mulder, E. Vlieg, and J. Schermer, "Proton irradiation induced GaAs solar cell performance degradation simulations using a physics-based model," *Solar Energy Materials and Solar Cells*, vol. 223, p. 110971, 2021, doi: doi:https://doi.org/10.1016/j.solmat.2021.110971. [Online]. Available: https://www.sciencedirect.com/science/article/pii/S0927024821000155

[121] S. R. Messenger, G. P. Summers, E. A. Burke, R. J. Walters, and M. A. Xapsos, "Modeling solar cell degradation in space: A comparison of the NRL displacement damage dose and the JPL equivalent fluence approaches†," *Progress in Photovoltaics: Research and Applications*, vol. 9, no. 2, pp. 103–121, 2001, doi: doi:https://doi.org/10.1002/pip.357. [Online]. Available: https://onlinelibrary.wiley.com/doi/abs/10.1002/pip.357

[122] G. Yan, J. ling Wang, J. Liu, Y. yu Liu, R. Wu, and R. Wang, "Electroluminescence analysis of VOC degradation of individual subcell in GaInP/GaAs/Ge space solar cells irradiated by 1.0 MeV electrons," *Journal of Luminescence*, vol. 219, p. 116905, 2020, doi: doi:https://doi.org/10.1016/j.jlumin.2019.116905. [Online]. Available: https://www.sciencedirect.com/science/article/pii/S0022231319313444

[123] N. Z. Vagidov, K. H. Montgomery, G. K. Bradshaw, and D. A. Wilt, "Light trapping structures for radiation hardness enhancement of space solar cells," *Solar Energy Materials and Solar Cells*, vol. 182, pp. 136–141, 2018, doi: doi:https://doi.org/10.1016/j.solmat.2018.03.036. [Online]. Available: https://www.sciencedirect.com/science/article/pii/S0927024818301478

[124] S. Tobin, S. Vernon, M. Sanfacon, and A. Mastrovito, "Enhanced light absorption in gaas solar cells with internal bragg reflectors," in *The Conference Record of the Twenty-Second IEEE Photovoltaic Specialists Conference - 1991*, 1991, pp. 147–152 vol.1.

[125] V. M. Lantratov, V. M. Emelyanov, N. A. Kalyuzhnyy, S. A. Mintairov, and M. Z. Shvarts, "Improvement of radiation resistance of multijunction gainp/ga(in)as/ge solar cells with application of bragg reflectors," in *5th FORUM ON NEW MATERIALS PART C*, ser. Advances in Science and Technology, vol. 74. Trans Tech Publications Ltd, 1 2011, pp. 225–230.

[126] S. J. Polly, G. T. Nelson, J. R. D'Rozario, R. Tatavarti, and S. M. Hubbard, "Radiation effects in thinned gaas photovoltaics incorporating dbrs for improved radiation tolerance of multijunctions," in *2019 IEEE 46th Photovoltaic Specialists Conference (PVSC)*, 2019, pp. 2818–2821.

[127] R. Tatavarti, K. Forghani, R. Reddy, J. R. D'Rozario, G. T. Nelson, and S. Hubbard, "Radiation hardening of dual junction solar cells," in *2020 47th IEEE Photovoltaic Specialists Conference (PVSC)*, 2020, pp. 2258–2261.

[128] T. Takamoto, H. Washio, and H. Juso, "Application of InGaP/GaAs/InGaAs triple junction solar cells to space use and concentrator photovoltaic," in *2014 IEEE 40th Photovoltaic Specialist Conference (PVSC)*, 2014, pp. 0001–0005, doi: doi:10.1109/PVSC.2014.6924936.

[129] H. Gao, R. Yang, and Y. Zhang, "Improving Radiation Resistance of GaInP/GaInAs/Ge Triple-Junction Solar Cells Using GaInP Back-Surface Field in the Middle Subcell," *Materials*, vol. 13, no. 8, 2020, doi: doi:10.3390/ma13081958. [Online]. Available: https://www.mdpi.com/1996-1944/13/8/1958

References

[130] W. Laiadi, A. Meftah, and C. Laiadi, "Effect of proton irradiation fluence on the performance of the AlxGa1-xAs/GaAs p+ nn+ solar cell," *Algerian Journal of Environmental Science and Technology*, vol. 7, no. 3, 2021, https://www.aljest.org/index.php/aljest/article/view/580.

[131] D. J. Curtin and R. L. Statler, "Review of Radiation Damage to Silicon Solar Cells," *IEEE Transactions on Aerospace and Electronic Systems*, vol. AES-11, no. 4, pp. 499–513, 1975, doi: doi:10.1109/TAES.1975.308112.

[132] R. Hill and N. M. Pearsall, "Indium phosphide solar cells," in *IEE Colloquium on Solar Cells for Space Applications*, 1988, pp. 2/1–2/5. [Online]. Available: https://ieeexplore.ieee.org/document/209641

[133] J. R. Woodyard and G. A. Landis, "Radiation resistance of thin-film solar cells for space photovoltaic power," *Solar Cells*, vol. 31, no. 4, pp. 297–329, 1991, special Issue: Radiation Effects on Solar Cells. doi: doi:https://doi.org/10.1016/0379-6787(91)90103-V. [Online]. Available: https://www.sciencedirect.com/science/article/pii/037967879190103V

[134] R. J. Walters, "A review of radiation effects in InP solar cells," in *Proceedings of 1994 IEEE 6th International Conference on Indium Phosphide and Related Materials (IPRM)*, 1994, pp. 275–279, doi: doi:10.1109/ICIPRM.1994.328220.

[135] B. Anspaugh, "Proton and electron damage coefficients for gaas/ge solar cells," in *The Conference Record of the Twenty-Second IEEE Photovoltaic Specialists Conference - 1991*, 1991, pp. 1593–1598 vol.2.

[136] P. Iles, "Evolution of space solar cells," *Solar Energy Materials and Solar Cells*, vol. 68, no. 1, pp. 1–13, 2001, solar cells in space. doi: doi:https://doi.org/10.1016/S0927-0248(00)00341-X. [Online]. Available: https://www.sciencedirect.com/science/article/pii/S092702480000341X

[137] H. Tada and J. Carter Jr, "Solar cell radiation handbook," Jet Propulsion Laboratory, Tech. Rep., November 1977. [Online]. Available: https://ntrs.nasa.gov/citations/19780007623

[138] B. Anspaugh *et al.*, "GaAs solar cell radiation handbook," National Aeronautics and Space Administration, Jet Propulsion Laboratory., Tech. Rep., July 1996, uRL: https://ntrs.nasa.gov/citations/19970010878.

[139] S. Karazhanov, "Mechanism for the anomalous degradation of proton- or electron-irradiated silicon solar cells," *Solar Energy Materials and Solar Cells*, vol. 69, no. 1, pp. 53 – 60, 2001, doi: doi:https://doi.org/10.1016/S0927-0248(00)00358-5. [Online]. Available: http://www.sciencedirect.com/science/article/pii/S0927024800003585

[140] N. de Angelis, J. Bourgoin, T. Takamoto, A. Khan, and M. Yamaguchi, "Solar cell degradation by electron irradiation. Comparison between Si, GaAs and GaInP cells," *Solar Energy Materials and Solar Cells*, vol. 66, no. 1, pp. 495 – 500, 2001, pVSEC 11 - Part II. doi: doi:https://doi.org/10.1016/S0927-0248(00)00211-7. [Online]. Available: http://www.sciencedirect.com/science/article/pii/S0927024800002117

[141] T. Sumita, M. Imaizumi, S. Matsuda, T. Ohshima, A. Ohi, and H. Itoh, "Proton radiation analysis of multi-junction space solar cells," *Nuclear Instruments and Methods in Physics Research Section B: Beam Interactions with Materials and Atoms*, vol. 206, pp. 448 – 451, 2003, 13th International Conference on Ion Beam Modification of Materials. doi: doi:https://doi.org/10.1016/S0168-583X(03)00791-2. [Online]. Available: http://www.sciencedirect.com/science/article/pii/S0168583X03007912

[142] S. Makham, M. Zazoui, G. Sun, and J. Bourgoin, "Prediction of proton-induced degradation of GaAs space solar cells," *Solar Energy Materials and Solar Cells*, vol. 90, no. 10, pp. 1513 – 1518, 2006, selected Papers from the 8th International Conference on Condensed Matter and Statistical Physics. doi: doi:https://doi.org/10.1016/j.solmat.2005.10.015. [Online]. Available: http://www.sciencedirect.com/science/article/pii/S0927024805003223

References

[143] S. R. Messenger, E. M. Jackson, J. H. Warner, and R. J. Walters, "Scream: A new code for solar cell degradation prediction using the displacement damage dose approach," in *2010 35th IEEE Photovoltaic Specialists Conference*, 2010, pp. 001 106–001 111, doi: doi:10.1109/PVSC.2010.5614713.

[144] V. Emelyanov, N. Kalyuzhniy, S. Mintairov, M. Shvarts, and V. Lantratov, "Multijunction gainp/gainas/ge solar cells with bragg reflectors," *Semiconductors*, vol. 44, no. 12, pp. 1600–1605, 2010, doi: doi:https://doi.org/10.1134/S1063782610120122.

[145] M. Z. Shvarts, E. A. Aronova, V. M. Emelyanov, N. A. Kalyuzhnyy, V. M. Lantratov, S. A. Mintairov, A. A. Soluyanov, and N. K. Timoshina, "Multijunction solar cell with intermediate ir reflector," *AIP Conference Proceedings*, vol. 1477, no. 1, pp. 28–31, 2012, doi: doi:https://doi.org/10.1063/1.4753826. [Online]. Available: https://aip.scitation.org/doi/abs/10.1063/1.4753826

[146] A. Skachkov, "Optimization of the structure of a gainp/gaas/ge triple-junction solar cell with an al 0.1 ga 0.9 as/al 0.8 ga 0.2 as integrated bragg reflector," *Optoelectronics, Instrumentation and Data Processing*, vol. 50, no. 4, pp. 423–427, 2014, doi: doi:https://doi.org/10.3103/S8756699014040165.

[147] Y. Jiang, M. J. Keevers, P. Pearce, N. Ekins-Daukes, and M. A. Green, "Design of an intermediate bragg reflector within triple-junction solar cells for spectrum splitting applications," *Solar Energy Materials and Solar Cells*, vol. 193, pp. 259–269, 2019, doi: doi:https://doi.org/10.1016/j.solmat.2019.01.011. [Online]. Available: https://www.sciencedirect.com/science/article/pii/S092702481930011X

[148] H. Karadeniz, "A study on triple-junction GaInP2/InGaAs/Ge space grade solar cells irradiated by 24.5 MeV high-energy protons," *Nuclear Instruments and Methods in Physics Research Section B: Beam Interactions with Materials and Atoms*, vol. 471, pp. 1–6, 2020, doi: doi:https://doi.org/10.1016/j.nimb.2020.03.015. [Online]. Available: https://www.sciencedirect.com/science/article/pii/S0168583X20301300

[149] E. Yaccuzzi, S. D. Napoli, E. J. D. Liscia, S. Suárez, M. Alurralde, A. Strittmatter, J. Pla, and P. Giudici, "Experimental re-evaluation of proton penetration ranges in GaAs and InGaP," *Journal of Physics D: Applied Physics*, vol. 54, no. 11, p. 115302, jan 2021, doi: doi:10.1088/1361-6463/abce7d. [Online]. Available: https://doi.org/10.1088/1361-6463/abce7d

[150] W. Guter, J. Schöne, S. P. Philipps, M. Steiner, G. Siefer, A. Wekkeli, E. Welser, E. Oliva, A. W. Bett, and F. Dimroth, "Current-matched triple-junction solar cell reaching 41.1% conversion efficiency under concentrated sunlight," *Applied Physics Letters*, vol. 94, no. 22, p. 223504, 2009, doi: doi:10.1063/1.3148341. [Online]. Available: https://doi.org/10.1063/1.3148341

[151] *2000 ASTM Standard Extraterrestrial Spectrum Reference E-490-00*, National Renewable Energy Laboratory Std., 2000, (Accessed on 12/12/2021). [Online]. Available: https://www.nrel.gov/grid/solar-resource/spectra-astm-e490.html

[152] G. Siefer, C. Baur, and A. W. Bett, "External quantum efficiency measurements of Germanium bottom subcells: Measurement artifacts and correction procedures," in *2010 35th IEEE Photovoltaic Specialists Conference*, 2010, pp. 000 704–000 707.

[153] JAXA. The jaxa space exploration innovation hub center co-produces results on remote and automatic control to build lunar base. (Accessed on 10/14/2021). [Online]. Available: https://global.jaxa.jp/press/2019/03/20190328a.html

[154] M. Gibson and P. Schmitz, "Higher Power Design Concepts for NASA's Kilopower Reactor," in *2020 IEEE Aerospace Conference*. IEEE, 2020, pp. 1–9.

[155] E. J. Speyerer and M. S. Robinson, "Persistently illuminated regions at the lunar poles: Ideal sites for future exploration," *Icarus*, vol. 222, no. 1, pp. 122–136, 2013. [Online]. Available: https://www.sciencedirect.com/science/article/pii/S0019103512004174

References

[156] T. W. Kerslake, "Lunar Surface-to-Surface Power Transfer," in *AIP Conference Proceedings*, vol. 969, no. 1. American Institute of Physics, 2008, pp. 466–473.

[157] L. Summerer and O. Purcell, "Concepts for wireless energy transmission via laser," *Europeans Space Agency (ESA)-Advanced Concepts Team*, 2009.

[158] K. Jin and W. Zhou, "Wireless laser power transmission: A review of recent progress," *IEEE Transactions on Power Electronics*, vol. 34, no. 4, pp. 3842–3859, 2019. [Online]. Available: https://doi.org/10.1109/TPEL.2018.2853156

[159] D. E. Smith, M. T. Zuber, G. B. Jackson, J. F. Cavanaugh, G. A. Neumann, H. Riris, X. Sun, R. S. Zellar, C. Coltharp, J. Connelly *et al.*, "The lunar orbiter laser altimeter investigation on the lunar reconnaissance orbiter mission," *Space science reviews*, vol. 150, no. 1, pp. 209–241, 2010.

[160] G. Neumann, D. Smith, S. Scott, S. Slavney, and E. Grayzek, "Lunar Reconnaissance Orbiter Lunar Orbiter Laser Altimeter reduced data record and derived products software interface specification, version 2.6," *National Aeronautics and Space Administration Planetary Data System (Accessed 01 December 2020)*, 2016. [Online]. Available: http://pds-geosciences.wustl.edu/missions/lro/lola.htm

[161] NASA-JPL. Solar System Dynamics: HORIZONS Web-Interface. (Accessed on 01/09/2021). [Online]. Available: https://ssd.jpl.nasa.gov/horizons.cgi#results

[162] D. R. Williams. (2018, feb) Sun Fact Sheet. NASA Goddard Space Flight Center. [Online]. Available: https://nssdc.gsfc.nasa.gov/planetary/factsheet/sunfact.html

Summary of Papers

Paper A

Space Microgrids for Future Manned Lunar Bases: A Review

Diptish Saha, *Student Member, IEEE,* Najmeh Bazmohammadi, *Member, IEEE,*
José Maurilio Raya-Armenta, Angelina D. Bintoudi, *Student Member, IEEE,*
Abderezak Lashab, *Member, IEEE,* Juan C. Vasquez, *Senior Member, IEEE,* and
Josep M. Guerrero, *Fellow, IEEE*

Paper B

An Accurate Physical Model for PV Modules With Improved Approximations of Series-Shunt Resistances

José Maurilio Raya-Armenta, Pablo R. Ortega,
Najmeh Bazmohammadi, *Member, IEEE*, Sergiu V. Spataru, *Member, IEEE*,
Juan C. Vasquez, *Senior Member, IEEE*, and Josep M. Guerrero, *Fellow, IEEE*

113

Paper C

A Short Review of Radiation-Induced Degradation of III-V Photovoltaic Cells for Space Applications

José Maurilio Raya-Armenta, Najmeh Bazmohammadi, Juan C. Vasquez, Josep M. Guerrero

Paper D

Optimal Allocation of a PV-Based Lunar Multi-Microgrid Based on a Novel Method to Estimate Sun Illumination Profiles

José Maurilio Raya-Armenta, Najmeh Bazmohammadi, *Member, IEEE*, Juan C. Vasquez, *Senior Member, IEEE*, and Josep M. Guerrero, *Fellow, IEEE*